ILLINOIS CENTER FOR TRANSPORTATION

Report No. FHWA-ICT-26-005

Spatial and Temporal Load Distribution in Steel Bridge Superstructures (Vol. II): Evaluation of Skewed Steel I-Girder Bridge Behavior under Deck Placement and Live Load through Field Monitoring and Numerical Simulation

Siang Zhou
Ricardo Dorado
Larry A. Fahnestock
James M. LaFave

ICT Project R27-194

May 2026

ISSN: 0197-9191
ICT Series Report No. 26-005
https://doi.org/10.36501/0197-9191/26-005

TECHNICAL REPORT DOCUMENTATION PAGE

1. Report No.	2. Government Accession No.	3. Recipient's Catalog No.
FHWA-ICT-26-005	N/A	N/A

4. Title and Subtitle	5. Report Date
Spatial and Temporal Load Distribution in Steel Bridge Superstructures (Vol. II): Evaluation of Skewed Steel I-Girder Bridge Behavior under Deck Placement and Live Load through Field Monitoring and Numerical Simulation	May 2026
	6. Performing Organization Code N/A

7. Authors	8. Performing Organization Report No.
Siang Zhou (https://orcid.org/0000-0002-1540-5698), Ricardo Dorado (https://orcid.org/0000-0002-5906-4792), Larry A. Fahnestock (https://orcid.org/0000-0003-3172-2260), James M. LaFave (https://orcid.org/0000-0001-6514-2163)	ICT-26-005 UILU-2026-2005

9. Performing Organization Name and Address	10. Work Unit No.
Illinois Center for Transportation Department of Civil and Environmental Engineering University of Illinois Urbana-Champaign 205 North Mathews Avenue, MC-250 Urbana, IL 61801	N/A
	11. Contract or Grant No. R27-194

12. Sponsoring Agency Name and Address	13. Type of Report and Period Covered
Illinois Department of Transportation (SPR) Bureau of Research 126 East Ash Street Springfield, IL 62704	Interim Report 7/1/18–5/31/26
	14. Sponsoring Agency Code

15. Supplementary Notes

Conducted in cooperation with the U.S. Department of Transportation, Federal Highway Administration.

https://doi.org/10.36501/0197-9191/26-005

16. Abstract

Two skewed (around 45°) two-span continuous bridges with stub abutments or integral abutments were monitored in the field during construction and after the bridges were in service. The goal was to establish a comprehensive understanding of load distribution in skewed steel I-girder bridges and to potentially refine their analysis and design procedures. Key girder cross-sections and cross-frames were instrumented with strain gauges, and global bridge movements were captured with displacement transducers and tiltmeters. Temperature was recorded simultaneously with structural response measurements. Numerical studies using 3D finite element analysis (FEA) were based on a field-validated simulation framework. The 3D FEA was conducted on the instrumented bridges to evaluate effects of bridge geometry, especially skew and abutment type, on skewed steel I-girder bridge superstructure response. Load distribution during deck placement and under live load was investigated, and standard design guidelines regarding girder strong-axis bending and flange lateral bending were evaluated. For a skewed bridge with a staggered cross-frame layout along its length under concrete dead load, standard design recommendations from the AASHTO "LRFD Bridge Design Specifications" regarding skew-related lateral bending stress might not be appropriate for both interior and exterior girders. Under isolated truck live loads, exterior girders are prone to larger strong-axis bending stress than interior girders when directly loaded, while interior girders are more critical regarding flange lateral bending stress than exterior girders. Distribution of lateral bending stress on a skewed bridge is dependent on the live load position, and limiting the distance between the first intermediate cross-frame and bridge ends is important to avoid lateral bending stress concentration near bridge obtuse corners. The dynamic load allowance of 33% used in design was found to be mostly conservative, except at a few monitored locations near obtuse corners of the integral abutment bridge.

17. Key Words	18. Distribution Statement
Skewed Bridge, Steel I-Girder Bridge, Flange Lateral Bending, Field Monitoring, Numerical Simulation, Deck Placement, Live Load	No restrictions. This document is available through the National Technical Information Service, Springfield, VA 22161.

19. Security Classif. (of this report)	20. Security Classif. (of this page)	21. No. of Pages	22. Price
Unclassified	Unclassified	79	N/A

ACKNOWLEDGMENT, DISCLAIMER, MANUFACTURERS' NAMES

This publication is based on the results of **ICT-R27-194: Spatial and Temporal Load Distribution in Steel Bridge Superstructures**. ICT-R27-194 was conducted in cooperation with the Illinois Center for Transportation; the Illinois Department of Transportation; and the U.S. Department of Transportation, Federal Highway Administration.

Members of the Technical Review Panel (TRP) were the following:

- Mark Shaffer, TRP Chair, Illinois Department of Transportation
- Andrew Bauer, Illinois Department of Transportation
- Ruben Boehler, Illinois Department of Transportation
- Nick Lombardi, Federal Highway Administration
- Peter Pascua, Illinois Department of Transportation
- Kevin Riechers, Illinois Department of Transportation

EXECUTIVE SUMMARY

Highly skewed steel I-girder bridges are commonly used, especially in congested areas, despite complications in their analysis, design, and construction. Additional research is needed to establish a comprehensive understanding of load distribution in skewed steel I-girder bridges and to potentially refine their analysis and design procedures. This report documents field monitoring of two skewed two-span continuous bridges in Champaign, Illinois: Mattis Avenue over I-74 (Mattis-74) and Mattis Avenue over I-57 (Mattis-57). Mattis-74 is a stub abutment bridge with 41° skew, and Mattis-57 is an integral abutment bridge with 45° skew. Key girder cross-sections and cross-frames were instrumented with strain gauges, the end rotations of critical girders were measured with tiltmeters, global bridge movements were captured with displacement transducers, and temperature was recorded simultaneously with structural response measurements. Sensing equipment capable of high sampling frequency (up to 20 Hz) was used. Data collection was initiated during construction, and the instrumented bridges were evaluated in the field during concrete deck placement and after each bridge was in service through isolated truck tests at various speeds: 3.2 kph (2 mph), 32 kph (20 mph), and 56 kph (35 mph). A 3D finite element analysis (FEA) was conducted to provide enhanced understanding of bridge behavior. Good agreement was observed between the numerical simulation results and field monitoring data for both deck placement and live load testing. Numerical parametric studies were conducted on the instrumented bridges to evaluate effects of bridge geometry, especially skew and abutment type, on skewed steel I-girder bridge superstructure response. Load distribution during deck placement and under live load was investigated, and standard design guidelines regarding girder strong-axis bending and flange lateral bending were evaluated.

Under concrete dead load, a staggered cross-frame layout provided additional load paths that transferred lateral load from the deck overhang to the interior girders, which was observed to be more significant near midspan of a skewed bridge. Development of flange lateral bending near supports of a skewed bridge was primarily caused by superstructure stiffness along the skewed bearing lines. Large flange lateral bending stress occurred when the lateral movement induced from girder rotation along the skew was restrained at the support. For a skewed bridge with a staggered cross-frame layout along its length, standard design recommendations from the AASHTO *LRFD Bridge Design Specifications* (2024) regarding skew-related lateral bending stress might not be appropriate for both interior and exterior girders. Under isolated truck live loads, exterior girders are prone to larger strong-axis bending stress than interior girders when directly loaded. Estimating girder strong-axis bending stress using line girder analysis with the live load distribution factor (LLDF) calculated according to AASHTO requirements is overall conservative for isolated truck loads, but the common practice to use a controlling LLDF for all girders can be overly conservative for interior girders. On the other hand, interior girders are more critical regarding flange lateral bending stress than exterior girders. The distribution of lateral bending stress on a skewed bridge is dependent on live load positioning, and limiting the minimum distance from the first intermediate cross-frames to bridge ends is important to avoid lateral stress concentration near bridge obtuse corners. The dynamic load allowance of 33% used in design was found to be mostly conservative, except for at a few monitored locations near obtuse corners of the integral abutment bridge.

TABLE OF CONTENTS

LIST OF FIGURES

LIST OF TABLES

CHAPTER 1: INTRODUCTION

Highly skewed steel I-girder bridges are commonly used across the United States, especially in congested areas, despite complications in their analysis and design during construction and after bridges are in-service (Greimann et al., 2014; LaFave et al., 2021; Luo et al., 2021; McConnell et al., 2016; Okumus et al., 2018). Illinois Center for Transportation project R27-194 aims to provide a comprehensive understanding of load distribution in skewed steel I-girder bridges and to potentially refine their analysis and design procedures through field monitoring and numerical simulations. This report, Volume II for the R27-194 project, documents the evaluation of bridge response based on field monitoring and numerical simulation results. The following sections provide information on the monitoring campaign and numerical simulation approaches. The background of this research project and details regarding field monitoring and numerical simulation approaches are elaborated on in Volume I (Zhou et al., 2026).

SUMMARY OF FIELD MONITORING

Two skewed two-span continuous bridges were monitored, as shown in Figures 1 and 2, to facilitate a greater understanding of skewed steel I-girder bridge behavior under construction dead load, in-service live load, and thermal loads. The I-74 and I-57 bridges over Mattis Avenue (referred to as Mattis-74 and Mattis-57 in this report, respectively) are close to each other in Champaign, Illinois. They are, therefore, expected to be under almost identical environmental conditions and experience similar traffic. Mattis-74 is a stub abutment bridge with a 41° skew angle and 12 steel I-girders of 1.8 m (70 in.) web height. Mattis-57 is an integral abutment bridge (IAB) with a 45° skew angle and eight steel I-girders of 1.9 m (74 in.) web height. Both bridges are two-span continuous and have internal X-shaped cross-frames arranged perpendicular to the girder lines in a staggered configuration. In the field-monitoring campaign, strain variation at select steel I-girders, critical cross-frames, and key concrete locations was measured with strain gauges. Rotations of select steel I-girders were measured with tiltmeters, while relative movement between the bridge superstructure and substructure was measured with displacement transducers called crackmeters, as shown in Figures 1 and 2. Temperature was collected concurrently at all gage locations through built-in thermistors.

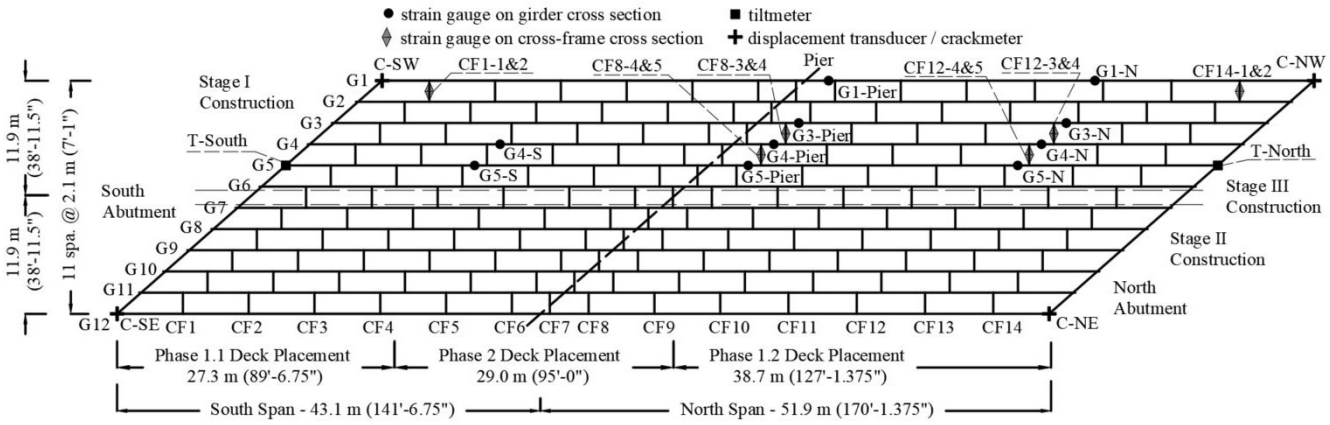

Figure 1. Plan view. Mattis-74 with instrument locations.

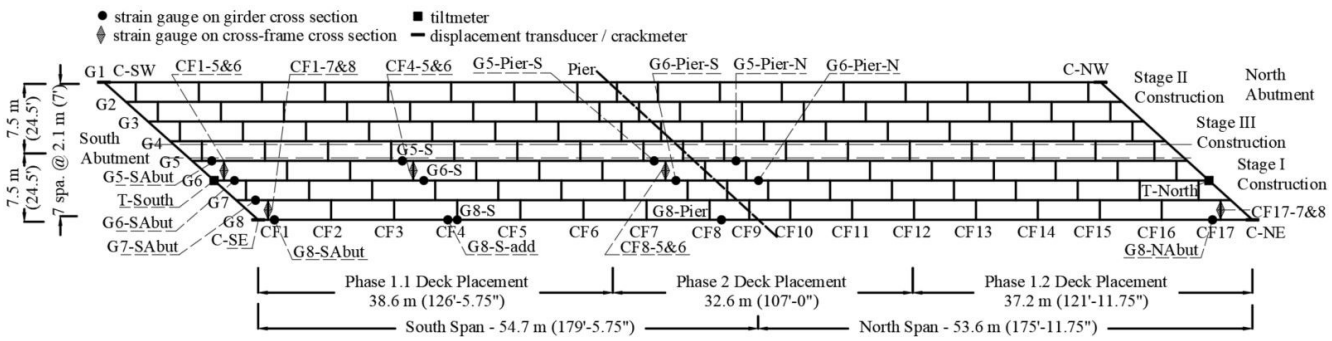

Figure 2. Plan view. Mattis-57 with instrument locations.

Girder and cross-frame sections were instrumented where the largest compressive or tensile stresses were expected for both bridges. For Mattis-57, there was additional focus on bridge acute and obtuse corners to observe behavior introduced by restraint at the integral abutments. Both bridges were constructed in three stages, where Stage I (approximately half of the bridge) was built and in service while Stage II was under construction. Stage III was then a closure pour between Stages I and II toward the end of the construction period. To allow the full instrumentation systems to be brought online all at once and to capture behavior starting with the construction phase, the monitoring program focuses on the region of the bridges within Stage I. The concrete deck slab was placed in two phases (Phase 1 in the positive moment regions and Phase 2 in the negative moment region), as shown in Figures 1 and 2. Phases 1 and 2 were separated by six days, and Phase 1 deck placement was conducted in two parts during the same day: Phase 1.1 in the south span and Phase 1.2 in the north span for both bridges.

Girder cross-sections were either heavily instrumented—with eight strain gauges on the girder and one embedded gauge in the concrete deck, as shown in Figure 3-A—or lightly instrumented with fewer gauges. At a heavily instrumented section, eight strain gauges were spot-welded to the steel girder and an embedded concrete strain gauge was tied to the reinforcing steel near mid-height of the deck before concrete placement. Interior girders under traffic lanes were heavily instrumented. Exterior girders, as well as some other interior girders, were lightly instrumented. For Mattis-74, girder cross-sections G4-Pier, G5-Pier, G4-N, and G5-N were heavily instrumented; for Mattis-57, girder cross-sections G6-SAbut, G6-Pier-S, and G6-Pier were heavily instrumented. Girder gauge locations were chosen between cross-frames to limit any disturbed region effects from connections, except at G8-S-add on Mattis-57. For fully instrumented girder cross-sections, measured strains were decomposed into components caused by strong-axis bending, flange lateral bending (comprising weak-axis bending and warping torsion), axial force, and local bending at the bottom flange and web (Deng et al., 2015; Greimann et al., 2014; Zhou et al., 2024). Then, strains were used to calculate stresses assuming elastic response under service live load. Less information was measured for lightly instrumented girder cross-sections. Plate local bending effects were not considered for four-gauge cross-sections. Volume I (Zhou et al., 2026) provides a detailed description of the data-processing scheme.

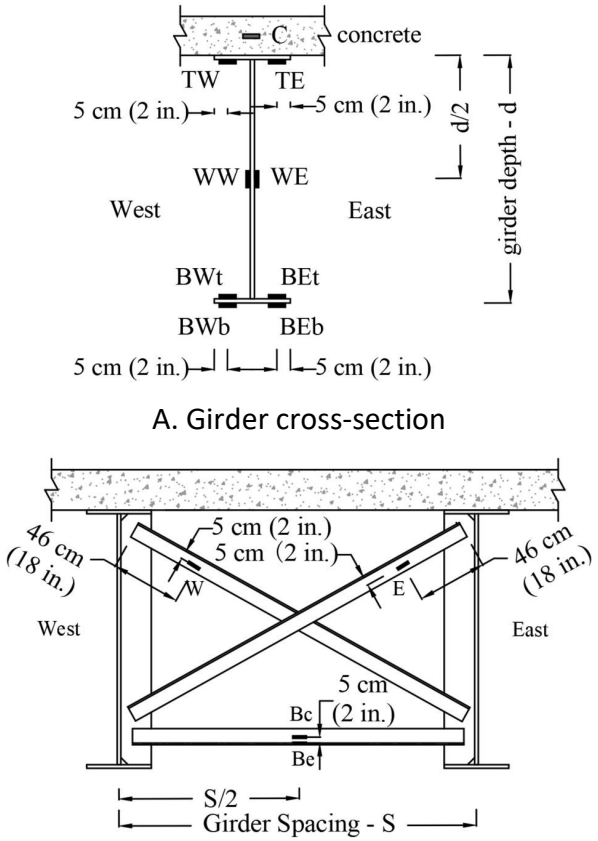

Figure 3. Schematic. Cross-section view of Mattis-57 and Mattis-74 strain gauge locations.

Cross-frames near the heavily instrumented girder cross-sections and close to bridge corners were monitored to understand the load path at those locations. Diagonal and bottom members of the cross-frames are all L100 × 100 × 10 mm (L4 × 4 × 3/8 in.). Three strain gauges were typically installed at an instrumented cross-frame location—at the west top portion of one diagonal angle (W), at the east top portion of the other diagonal angle (E), and at mid-length of the bottom chord angle on the connection (concentric) leg (Bc) (Figure 3-B). For location CF1-1&2 on Mattis-74, an additional strain gauge was placed at mid-length of the bottom chord angle on the outstanding (eccentric) leg—named CF1-1&2-Be—to study localized behavior of cross-frame members. Cross-frames were relatively lightly instrumented in this research, because the focus is on studying the response of I-girders.

Tiltmeters ("T") were installed at the two ends of a critical girder—G5 for Mattis-74 and G6 of Mattis-57—to measure girder end rotations. Linear displacement transducers (crackmeters, "C") were placed at the four corners (C-SW, C-NW, C-SE, and C-NE) of each bridge to measure relative movement between the bridge superstructure and substructure. Crackmeters were installed along and perpendicular to the girder line for the stub abutment bridge (Mattis-74, Figure 1) between the abutment and girder bottom flange (at the bearing level) and only along the girder line for the IAB (Mattis-57, Figure 2) between the approach slab and transition slab (approach-transition at the deck level).

SUMMARY OF NUMERICAL SIMULATION APPROACH

A 3D finite element analysis was conducted, using ABAQUS (2023), to enhance understanding of field response and strengthen evaluation of bridge behavior through parametric studies. Steel I-girders, a concrete deck for bridge in-service conditions (or wooden formwork for bridge construction conditions), steel cross-frames, and steel stiffeners were all modeled explicitly with 3D 4-node reduced integration shell elements (S4R), and steel end diaphragms in skewed stub abutment bridges were modeled with 3D 2-node linear beam elements (B31). Cross-frames were considered critical members for transferring lateral response between girders, especially to study the effect of skew, and were therefore modeled using the same level of detail as the I-girders. All instances were meshed with a typical element size of 13 cm (5 in.). The bridges were considered to behave elastically under dead load and traffic load, so linear elastic material properties were modeled.

Girders were defined as continuous over their full length, with tie-constraints for all degrees of freedom (dofs) at girder splices. Bent plates, transverse stiffeners, and bearing stiffeners were all modeled as simple rectangular plates. They were connected to girder webs and flanges with tie-constraints in all dofs along all contacting edges. Connections between cross-frame members and between cross-frames and transverse stiffeners (over the bolted area of the fully tensioned bolts) were simplified as tie-constraints in all dofs. Cross-frame angle end connections were defined to the connected leg of the angle, accounting for realistic eccentric loading with respect to the outstanding angle leg. Haunches were modeled to realistically represent the concrete slab for in-service bridges, and composite behavior was defined with tie-constraints connecting nodes of the haunches and steel girder top flanges in all six dofs.

During the deck placement process, girder top flanges were connected by wooden formwork as a platform to support and distribute the wet concrete dead load during deck placement, so the formwork was modeled as 20 cm (8 in.) thick shell elements with a material having low elastic modulus of 138 MPa (20 ksi). The overhang portion of the formwork was supported by steel brackets, which were modeled by truss elements connecting the edge of the formwork to the girder bottom flange-web junction. Edges of formwork and adjacent girder top flanges were tied with all displacement dofs, and steel brackets were also connected to the outer edge of the formwork (on the top) and along the girder bottom flange-web junction with all displacement dofs.

Boundary conditions at the end of Mattis-74 are Type I elastomeric bearings designed according to the Illinois Department of Transportation (IDOT, 2023) *Bridge Manual*, which were represented by simplified bearing springs connected to a rigid substructure. For the Mattis-57 IAB, end boundary conditions before integral abutment placement are the same as the bridge middle pier support—a fixed bearing, which is connected to the substructure with a bearing plate and pair of anchor bolts at the bottom flange. The steel bearing plate was represented as a set of compression-only truss elements along the girder bottom flange at the bearing stiffeners. The trusses were pinned (restrained in all displacement dofs) to the ground reference. Two beam elements were modeled to simulate the contribution from the pair of bolts in preventing girder uplift and in-plane movement, which were fixed at their base (restrained in all dofs) and pinned to the girder bottom flange at mid-width of the flange plate on both sides. The abutments for IABs are typically cast together with the concrete bridge deck. Therefore, the integral abutments and pile cap (for Mattis-57) were modeled as

concrete shell elements (S4R), meshed with the same element size of 13 cm (5 in.) as mentioned for other instances. Rigid connections between the abutment and superstructure (deck and girders) were represented with tie constraints in all dofs. Backfill soil friction and passive pressure (not considering at-rest or active pressure) were represented as springs at displacement dofs along and perpendicular to the abutments. Contributions from the piles supporting the integral abutments were modeled as lumped springs at and between girders under the abutment. Details regarding the definition of bearing springs for the stub abutments, soil springs, and pile stiffnesses for the integral abutments are documented in Volume I (Zhou et al., 2026).

Live load truck testing and the deck placement process were simulated by applying spatially progressing pressure on the deck (or on the wooden formwork and girder top flanges for deck placement) with a DLOAD user-subroutine. Truck wheels were defined as 50 × 25 cm (20 × 10 in.) regions of pressure (AASHTO, 2024) applied to the concrete deck. Wet concrete was placed along the skew and applied on the wooden formwork and girder top flanges (as was done in the field). Local coordinates were adjusted to properly extract normal stress from elements of interest. A five-point through-thickness Simpson's Rule integration was used for all S4R elements. Section points SP1 and SP5 were extracted for normal stresses representing the bottom and top surfaces of the shell elements, respectively. Temperature varied only slightly, both throughout the continuous deck placement over a few hours and during live load testing with an isolated vehicle, so thermal effects were not considered in these short-term analyses.

PARAMETRIC VARIATIONS OF INSTRUMENTED BRIDGES

To better understand the response of skewed steel I-girder bridges during deck placement and after being in service, sets of numerical parametric studies were conducted based on geometric variations of the two instrumented bridges. Modeling and geometric variations of the Mattis Avenue bridges are described in this section to facilitate discussion of numerical parametric study results. Mattis-74 and Mattis-57 were modeled with skew variations of 0°, 20°, 30°, 45°, 50°, 60°, 65°, and 70° and with bridge width variations having 4, 6, 8, and 12 girders. Skew variations of pre-composite Stage I Mattis Avenue bridges—stub abutment bridges with six girders (based on half bridge Mattis-74) and IABs with four girders (based on half bridge Mattis-57)—were studied under concrete dead load. The full set of skew and width variations for the composite stub abutment bridges and IABs were used to study bridge response under live load. With the intention of keeping bridges of geometric variations as similar as possible to the original design, cross-frame arrangement was the only slight adjustment made. All other bridge details were kept the same as the actual design of Mattis-74 (for stub abutment bridges) and Mattis-57 (for IABs).

The stub abutment bridges were modeled using intermediate cross-frame layouts consistent with the original design, which caused the allocation of edge cross-frames to be different as bridge skew varied. The location of the girder splices and arrangement of cross-frames near the bridge middle pier was kept the same as the original design. Figure 4 presents stub abutment bridges modeled with 12 girders and variation of bridge skew (0°, 45°, and 70° shown). As noted previously, the layout of inner cross-frames was kept identical from bridge to bridge, with edge cross-frame allocation being the only adjustment made for the bridges with skew variation.

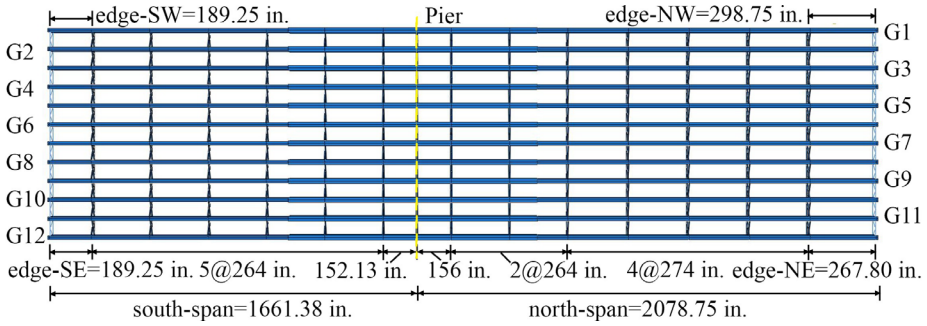

A. Skew angle: 0°

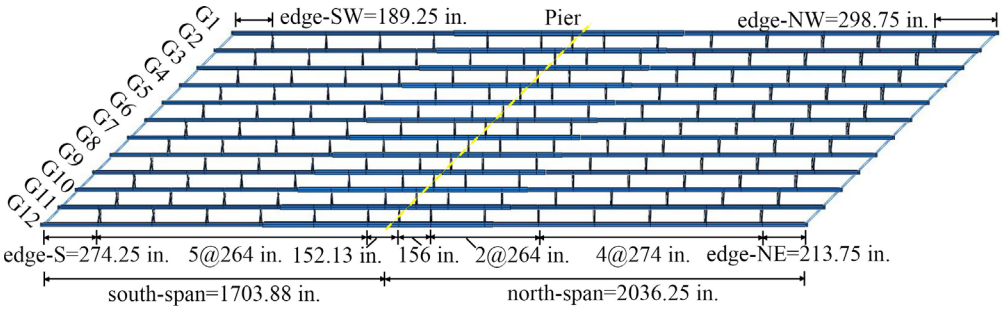

B. Skew angle: 45°

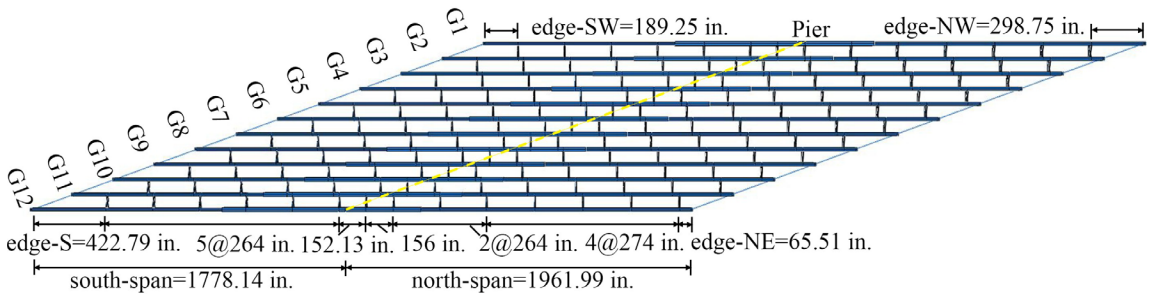

C. Skew angle: 70°

Figure 4. Plan view. Geometry of stub abutment bridges with skew variation.

AASHTO (2024, p. 6-86) C6.7.4.2 states: "Where support lines are skewed more than 20 degrees from normal and cross-frames or diaphragms are provided along the skewed support line, the first intermediate cross-frames or diaphragms placed normal to the girders adjacent to the skewed support ideally should be offset, where practicable, by a minimum of the larger of $4b_f$ or $0.4L_b$ from the support." This recommendation aims to avoid an increased transverse stiffness at skewed supports (AASHTO, 2024). Here, b_f is the largest girder flange width, and L_b is the unbraced length between the first and second intermediate cross-frames from the support. The minimum distance for the stub abutment bridges based on the design of Mattis-74 is 2.7 m (105.6 in.), which was not satisfied for bridges skewed at 70° used for parametric study. However, this variation was kept, as shown in Figure 4-C, in a consistent manner with the other models of skew variation, to facilitate comparisons. Observations regarding lateral bending response for models of stub abutment bridges

at 70° skew will be discussed considering that the recommendation on minimum end cross-frame distance was exceeded for these very highly skewed bridges included in the parametric studies.

Mattis-57 (with a 45° skew, Figure 5-B) was designed with an end cross-frame distance of 1.3 m (52.25 in.), so this distance was maintained as a minimum for the studied IAB variations. Figure 5 presents the IABs modeled with 12 girders and three variations of bridge skew. It includes abutments at the end as an illustration to distinguish IABs from stub abutment bridges. The abutments were not modeled for pre-composite stages during deck placement.

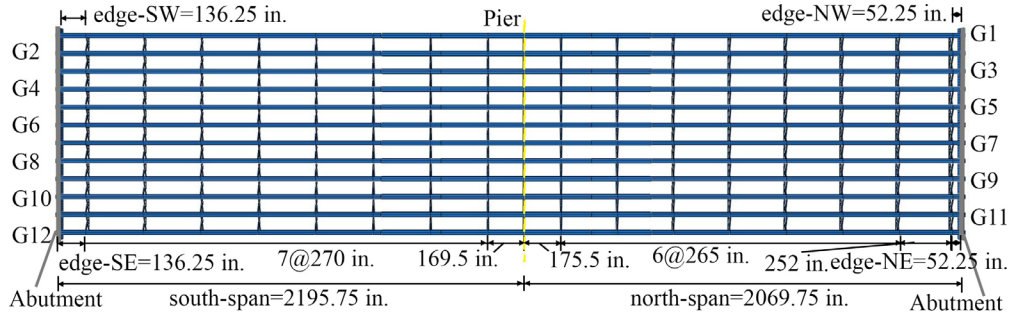

A. Skew angle: 0°

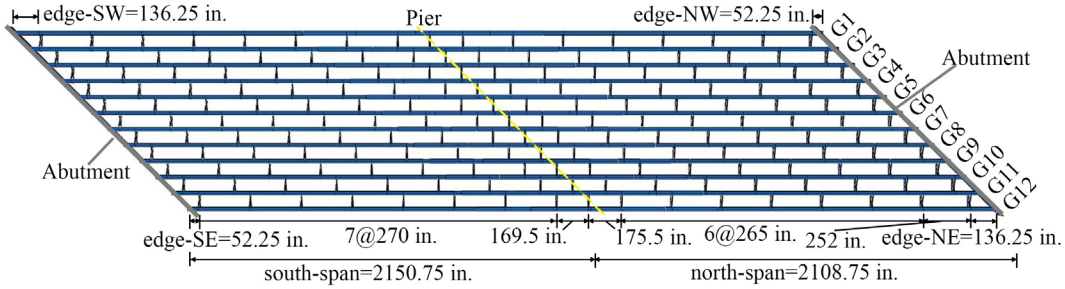

B. Skew angle: 45°

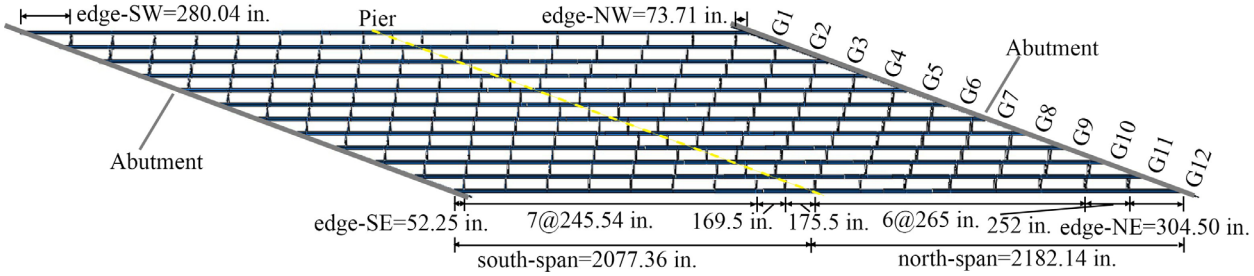

C. Skew angle: 70°

Figure 5. Plan view. Geometry of integral abutment bridges with skew variation.

CURRENT RESEARCH AND REPORT OUTLINE

This report (Volume II) presents the evaluation of girder strong-axis bending, lateral bending, cross-frame stress, and dynamic response of skewed steel I-girder bridges during construction and while in service through field monitoring and numerical simulation. The monitoring and analysis results are

presented in the following order: field monitoring of bridge response under deck placement (Chapter 2), numerical simulation results of bridge response under deck placement (Chapter 3), field monitoring of bridge response under live load (Chapter 4), and numerical simulation results of bridge response under live load (Chapter 5). Summary, conclusions, and recommendations for potential applications are presented in Chapter 6. The research project was carried out in the following four tasks, and this report supports the results presentation for Tasks 2 through 4, as summarized below.

- **Task 1: Literature review and agency survey**. A review of the existing research literature and typical design practices for steel I-girder bridges was conducted at the beginning of and throughout the project to inform, guide, and provide context to the current research. A summary of the literature review and findings from the responses to the agency survey are presented in Volume I (Zhou et al., 2026).

- **Task 2: Field monitoring**. Informed by findings from the agency survey, two new IDOT steel I-girder bridges were selected for a long-term field-monitoring campaign to collect comprehensive data that documents behavior from construction to after bridges are in service. Two bridges skewed around 45° (one with stub abutments and the other with integral abutments) were monitored in the field. Strain and temperature variation at critical girder cross-sections and cross-frames are monitored, and bridge global movement (girder end rotations and bridge movement) is captured. Information for the selected bridges, detailed instrumentation plan, and processing scheme of field measurements are presented in Volume I (Zhou et al., 2026). Observations based on the field measurements are presented in Chapters 2 and 4 of this report.

- **Task 3: Numerical simulation**. Numerical simulations are carried out in the current research to enhance understanding of field measurements by modeling the bridges under field monitoring and to provide insights about geometric effects on skewed steel I-girder bridge behavior through parametric studies. 3D finite element analysis methods have been developed since the beginning of the project. Before bridges were in place, numerical simulations were validated with prior research, and instrumentation placement was determined according to a set of preliminary numerical simulations. Iterations to improve the accuracy of computational modeling have been conducted with field measurements after data collection started. Numerical modeling methods and preliminary numerical simulations are presented in Volume I (Zhou et al., 2026). Observations based on the numerical simulation analysis results are presented in Chapters 3 and 5 of this report.

- **Task 4: Design recommendations**. After synthesizing the first three tasks, observations and insights on the behavior of skewed steel I-girder bridges are summarized, and analysis, design, and construction guidelines are proposed to implement the research results in practice. Field monitoring, companion numerical simulations, parametric study results, and observations on bridge behavior are presented in Chapters 2 through 5 and summarized in Chapter 6 of this report.

CHAPTER 2: BRIDGE RESPONSE UNDER DECK PLACEMENT—FIELD MONITORING

Steel I-girder bridges are subjected to unique loading conditions when they are under construction. Lateral bending of skewed bridges during deck placement is of particular interest. Proper evaluation of skew effects on girder lateral bending stress in pre-composite steel superstructures under concrete dead load is necessary for ensuring safety and economy in design for construction-stage loading. To provide new data on bridge response during deck placement, two instrumented skewed steel I-girder bridges (Mattis-74 in Figure 1 and Mattis-57 in Figure 2) were monitored during deck placement of Stage I construction. Girder stress components associated with strong-axis bending and lateral bending were calculated from field strain measurements, and complementary 3D finite element numerical simulations were conducted. Modeling strategies that properly incorporate field girder boundary conditions and deck overhang loading for pre-composite bridges were validated using field data from the two instrumented bridges. The deck placement process, observations from field monitoring, and validation between numerical simulation results and field measurements are presented in this chapter, with a focus on I-girder response.

FIELD OPERATIONS

The instrumented Mattis Avenue bridges were constructed in three stages, as illustrated in Figure 1 for Mattis-74 and in Figure 2 for Mattis-57, where Stage I occurred approximately six months before being connected to Stage II with a closure pour (Stage III). Stage I was the focus of field instrumentation for each bridge, so the analysis of deck placement based on field measurement is presented for Stage I. The concrete deck was placed in two phases during Stage I construction—with the positive moment regions poured about a week before the negative moment region. Phase 1.1 of deck placement for Mattis-74 started at the south abutment of the bridge and proceeded north, and Phase 1.2 started in the north span and proceeded north to the abutment. Deck placement in the negative moment region (Phase 2) then started in the south span. For Mattis-57, Phase 1.1 started in the south span and proceeded south to the abutment, and Phase 1.2 started at the north abutment and proceeded south; Phase 2 then started in the north span. For Mattis-57, the abutments were poured integral with the deck. These typical deck placement sequences were also considered in the numerical simulations.

Figures 6 and 7 present typical strain measurements for girder cross-sections on Mattis-74 and Mattis-57 during Stage I deck placement, respectively, including Phase 1 (Phase 1.1, closely followed by Phase 1.2) and Phase 2. Field measurements from slightly before and after deck placement are included, and the measured strains shown in Figures 6 and 7 were initialized about an hour before Phase 1 of deck placement. In later parts of this chapter, where field data are used to analyze bridge response, initialization is taken when concrete placement begins for each phase. Larger strain variations were measured during Phase 1 than during Phase 2, which will be further illustrated below. Heaters were placed between girders near their top flanges at least a day prior to each pour to overcome the cold weather during winter construction. A relatively stable temperature and thermal gradient were maintained during the heating process, including the few hours of deck placement,

with limited effects from solar radiation. Temperature variation and thermal gradient during deck placement were therefore not considered when analyzing the field response and conducting associated numerical simulations.

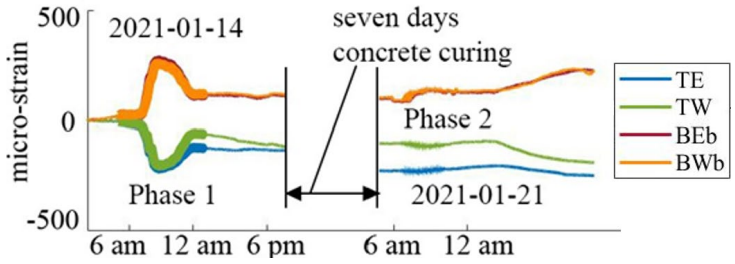

A. Cross-section G4-S

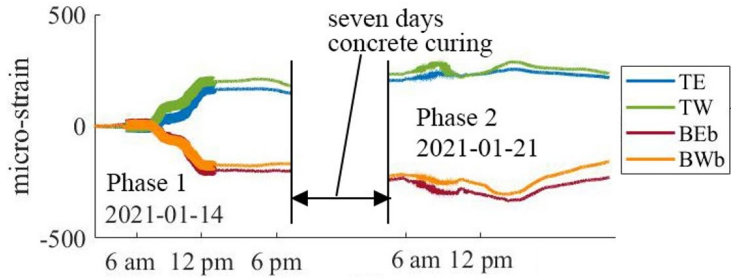

B. Cross-section G1-Pier

Figure 6. Graph. Typical strain measurements during Stage I deck placement at girder cross-sections on Mattis-74.

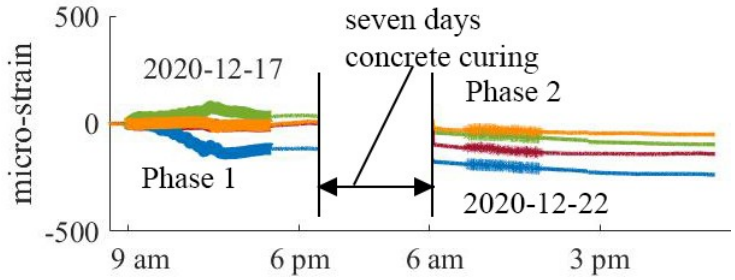

A. Cross-section G6-SAbut (top flange and web)

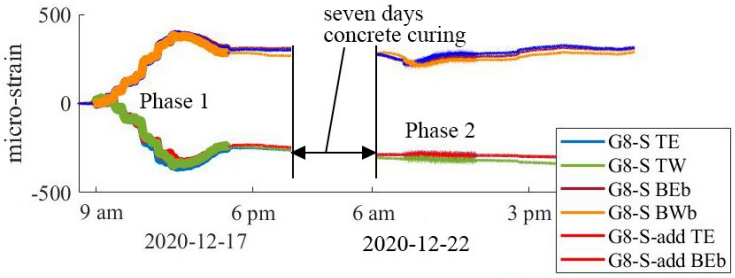

B. Cross-section G8-S and G8-S-add

Figure 7. Graph. Typical field strain measurements during Stage I deck placement at girder cross-sections on Mattis-57.

To study I-girder behavior, strain readings at gauge locations (field measurements) and stress outputs at element integration points (from numerical simulation results) were decomposed into components related to axial force, strong-axis bending, and lateral bending (including contributions from weak-axis bending and warping torsion effects). A pre-composite (steel-only) girder cross-section was considered for calculation of the theoretical elastic centroid. Bridge superstructure response is within the elastic range under concrete dead load, so decomposed girder strain from field monitoring was related directly to stress through the steel elastic modulus of 200 MPa (29,000 ksi). Axial force effects are small, so the primary stress components of interest are strong-axis and lateral bending, and axial effects are not reported in this and the following chapter.

When analyzing field results and validating models, strain measurements and stresses from numerical simulation results were taken at the field gauge locations and averages were calculated at the flange surfaces. Then, strong-axis bending stress was calculated at the bottom surface of the flanges, and lateral bending stress was evaluated at the gauge locations (5 cm [2 in.] from flange tips) for both field measurements and numerical simulation results of Mattis-57 and Mattis-74. On the other hand, when numerical simulation results were used for parametric study, stresses were extracted from flange edge elements. Decomposed stress was calculated to evaluate maximum strong-axis stress (at mid-thickness of flanges) and lateral bending stress (at flange tips) of a girder cross-section.

I-GIRDER STRONG-AXIS BENDING

Figures 8 and 9 present typical decomposed strong-axis bending stress comparisons between field measurements and numerical simulation results for Phase 1 deck placement on Mattis-74 and Mattis-57, respectively, initialized at the beginning of the phase. Figures 8-A and 9-A show symmetrical strong-axis bending response in the south span of Mattis-74 and Mattis-57, with the top flange in compression and the bottom flange in tension. The simulated strong-axis bending stress histories follow the trends observed in the field data, with similar peak values (compared in more detail below). Strong-axis moment in the span increases during Phase 1.1 of the deck pour as concrete was placed in the south span and then decreases during Phase 1.2 as concrete is placed in the north span (see Figures 1 and 2). Girder cross-sections near the pier had symmetrical strong-axis bending response with tension in the top flange and compression in the bottom flange, as shown in Figures 8-B and 9-B. The instrumented girder cross-sections near abutments on Mattis-57 have relatively small strong-axis bending stress compared to other cross-sections.

The peak strong-axis bending stress magnitudes for Mattis-74 and Mattis-57 are presented in Figures 10 and 11, respectively. These Phase 1 deck placement stresses show reasonable field-model agreement for strong-axis bending. Figures 10 and 11 also show Phase 2 (pier region, see Figures 1 and 2) field deck placement stresses, which are small compared to Phase 1 and, thus, are not important for further study. All models in the parametric studies described in Chapter 3 apply the load with a simplification of the full deck placed in a single phase.

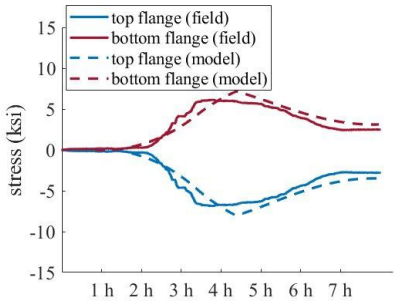

A. Cross-section G4-S

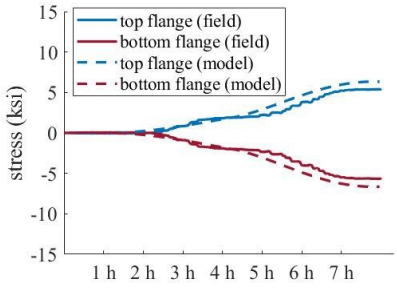

B. Cross-section G1-Pier

Figure 8. Graph. Typical decomposed strong-axis bending stress comparison between field measurements and numerical simulation results on Mattis-74.

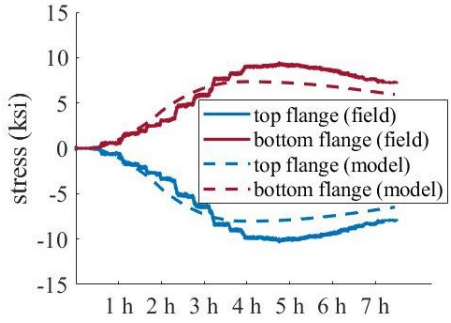

A. Cross-section G5-S

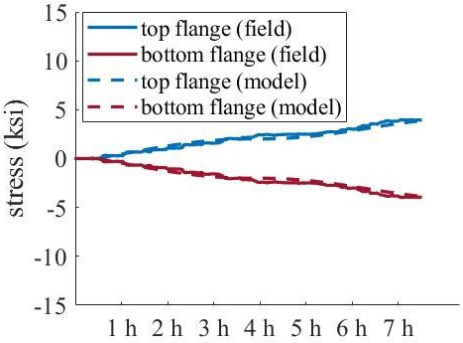

B. Cross-section G5-Pier-N

Figure 9. Graph. Typical decomposed strong-axis bending stress comparison between field measurements and numerical simulation results on Mattis-57.

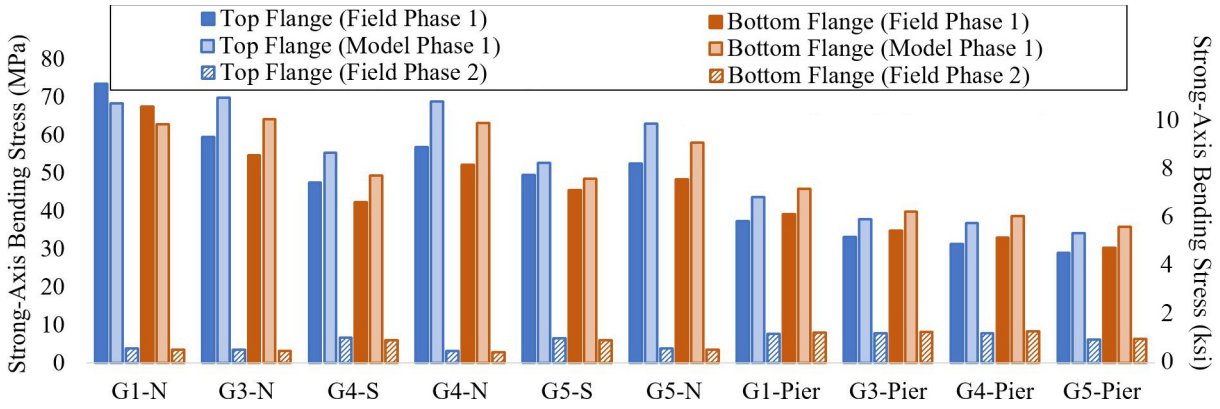

Figure 10. Graph. Field measurements and numerical simulation results—Mattis-74 strong-axis bending.

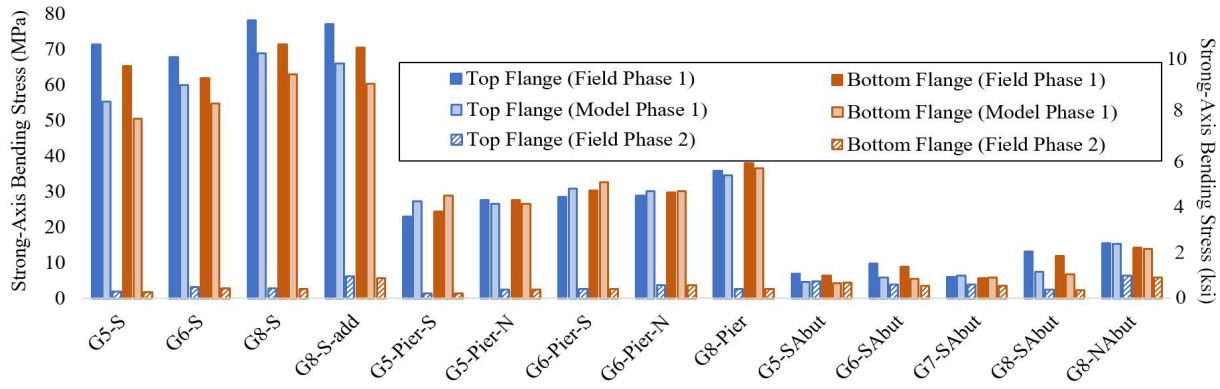

Figure 11. Graph. Field measurements and numerical simulation results—Mattis-57 strong-axis bending.

Phase 1 field measurements indicate that exterior girders experienced larger strong-axis bending stress than interior girders for both bridges: G1 for Mattis-74 and G8 for Mattis-57. This observation was most obvious for locations near midspan, with the most significant strong-axis bending behavior, but was also noted near bridge supports. The monitored distribution of strong-axis bending stress among girders during deck placement (larger for exterior girders than interior girders) was slightly different from what is typically presumed in design—the same requirements for exterior and interior girders. This could be caused by construction live load, especially that of the screed machine, which was supported near the exterior girders.

I-GIRDER LATERAL BENDING

Figures 12 and 13 present typical decomposed lateral bending stress comparisons between field measurements and numerical simulation results for Phase 1 deck placement on Mattis-74 and Mattis-57, respectively. The figures were initialized at the beginning of the phase, and the stresses were calculated at instrumented gauge locations—5 cm (2 in.) from the flange edge—of girder top and bottom flanges. (Positive values indicate tension on the flange west side.) Phase 2 was again not included in the figures due to the much smaller magnitude of strain measurements during that process.

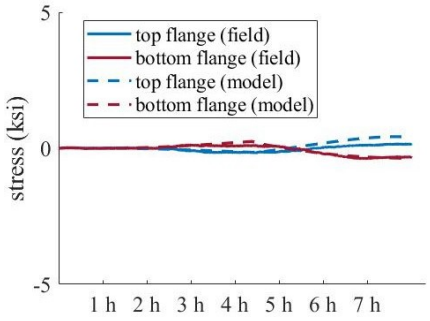

A. Cross-section G3-Pier

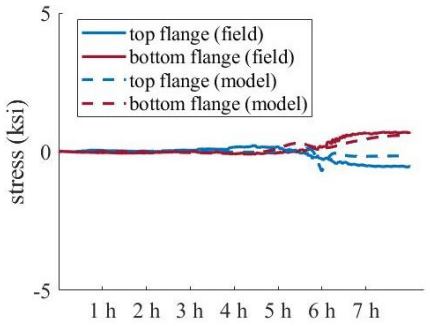

B. Cross-section G4-N

Figure 12. Graph. Typical decomposed lateral bending stress comparison between field measurements and numerical simulation results on Mattis-74.

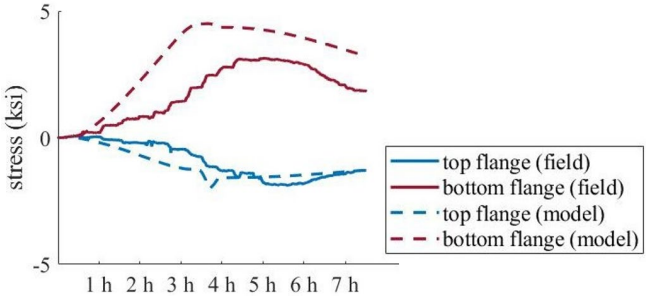

A. Cross-section G8-SAbut

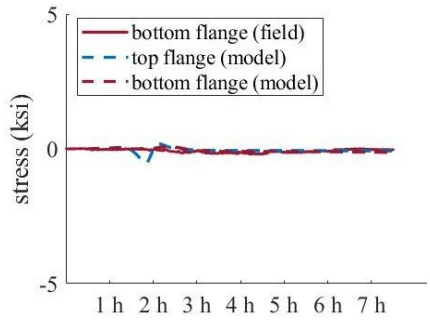

B. Cross-section G5-S

Figure 13. Graph. Typical decomposed lateral bending stress comparison between field measurements and numerical simulation results on Mattis-57.

The lateral bending stresses on the top and bottom flanges are usually distinct, and the most significant lateral bending response is observed at girder cross-sections near abutments for Mattis-57, as shown in Figure 13-A. The maximum magnitude of lateral bending stress (roughly 21 MPa [3 ksi]) is unexpected, considering the girder end is nominally pinned. However, the two-bolt bottom flange connection provides some resistance to lateral bending, and the influence is seen in both field and model stresses. The model stresses are generally higher than the field, indicating that the field condition is more flexible than the model idealization.

The peak flange lateral bending stress magnitudes for Mattis-74 and Mattis-57 are presented in Figures 14 and 15, respectively. Similar to the strong-axis bending behavior, Phase 2 deck placement generally contributed less to girder lateral bending behavior than Phase 1 (which was used as a basis for validating the numerical simulation approaches). As noted above, significant lateral bending response was observed for Mattis-57 near the ends of the girders. Since the in-span monitored girder cross-sections are offset from cross-frames, they do not record peak lateral bending behavior (AASHTO, 2024; Sanchez, 2011). Thus, as will be shown in Chapter 3 with numerical parametric studies, peak lateral bending stresses at cross-frame locations are expected to be approximately double to triple the field stresses reported in Figures 14 and 15.

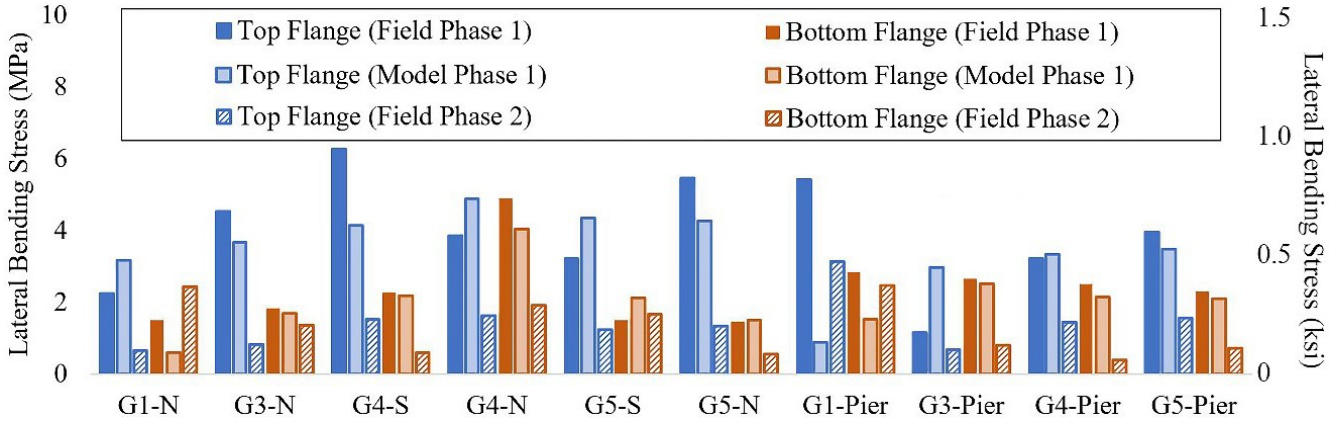

Figure 14. Graph. Field measurements and numerical simulation results—Mattis-74 lateral bending.

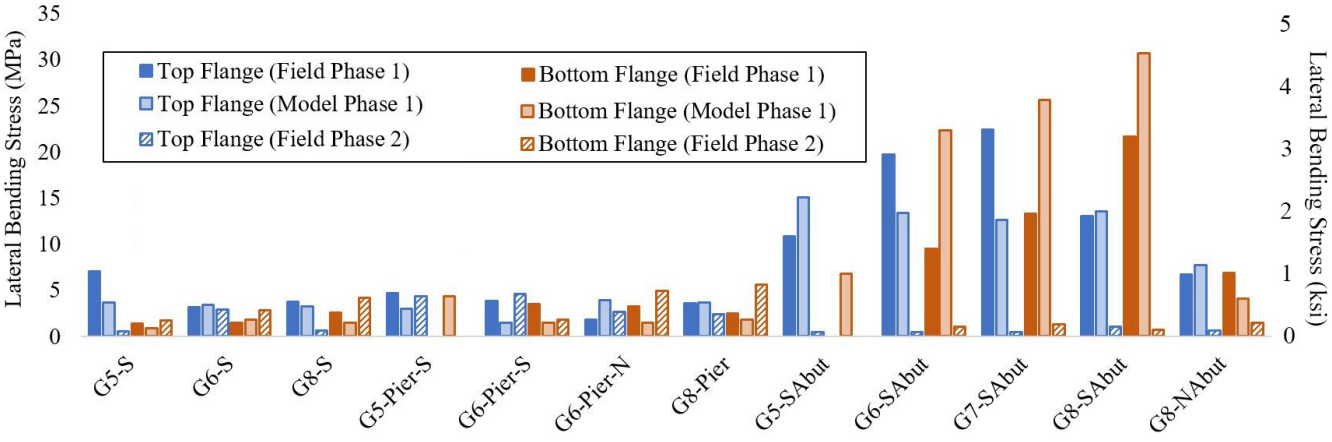

Figure 15. Graph. Field measurements and numerical simulation results—Mattis-57 lateral bending.

As illustrated in Figures 12 and 13, field flange lateral bending response history trends are reasonably captured by the model, although the field-model stress magnitude agreement is not as close as the field-model agreement for strong-axis bending. These comparisons indicate that construction-stage flange lateral bending stress magnitudes are more sensitive to modeling assumptions and idealizations than strong-axis bending stress magnitudes. The influence of girder end boundary conditions on flange lateral bending stress was discussed above (and in Volume I [Zhou et al., 2026]); even realistic models do not necessarily represent the true field support stiffness. Variations in construction live load, which are challenging to replicate, also influence field-model flange lateral bending agreement. Despite these limitations, the modeling framework developed here provides a sound basis for relative comparisons between bridge scenarios across a range of parametric variations.

CHAPTER 3: BRIDGE RESPONSE UNDER DECK PLACEMENT—NUMERICAL PARAMETRIC STUDY

This chapter describes a further evaluation of skewed steel I-girder bridge superstructure response during deck placement through parametric studies, focusing on the analysis of skew effects on flange lateral bending stress. The two instrumented bridges were studied with hypothetical skew variations from 0° to 70°, and nine other in-service bridges from the IDOT inventory were modeled with pre-composite conditions under concrete dead load as well. The background of the numerical parametric study and synthesis of the simulation results are presented, starting with observations based on the Mattis Avenue bridges with skew variation followed by expanding the findings to real IDOT bridges.

NUMERICAL PARAMETRIC STUDY BACKGROUND

Parametric studies were conducted to investigate the effects of bridge skew on strong-axis and lateral bending behavior of steel I-girders under deck placement. Two sets of analyses were conducted: (1) the instrumented Stage I Mattis Avenue bridges were studied with hypothetically varied skew at 0°, 20°, 30°, 45°, 50°, 60°, 65°, and 70°, with other parameters mostly unchanged, for a total of 16 unique bridge scenarios; and (2) nine real bridges (including the two instrumented Mattis Avenue bridges) were selected from a database provided by IDOT and analyzed as full and half bridges for a total of 17 additional unique bridge scenarios.

Sources of Flange Lateral Bending

The two major sources of flange lateral bending for I-girders in a skewed bridge during deck placement (Figure 16)—namely deck overhang and skew—were explained in Volume I (Zhou et al., 2026). Brackets at the outside face of the exterior girder transfer overhang loading, and in a skewed bridge, cross-frames then transfer lateral bending effects from exterior to interior girders through their staggered layout. This effect is referred to in this research as the overhang (local) skew effect. Cross-frames contribute to girder kinematics along skewed support lines, where there is a tendency for girders to rotate about the skewed support line instead of about their individual strong axes of bending (perpendicular to the girder line), as shown in Figure 16. This is referred to as the global skew effect.

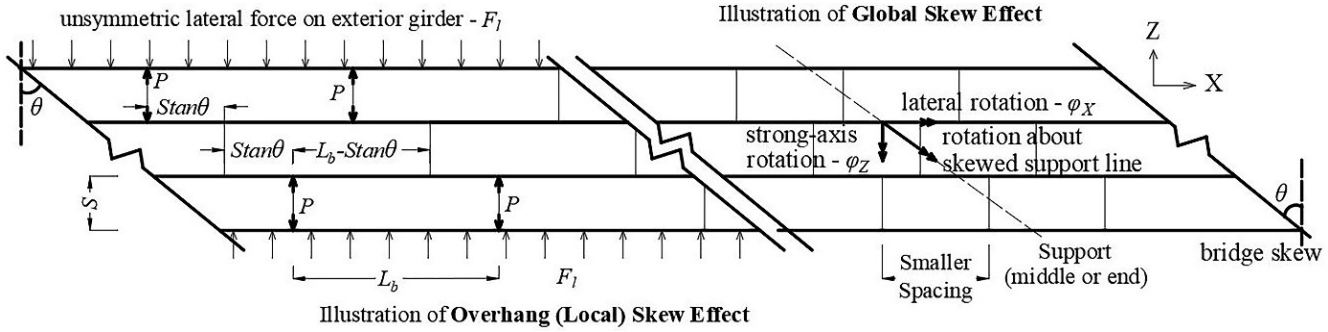

Figure 16. Plan view. Lateral load transfer of a typical skewed bridge at the bottom flange.

AASHTO (2024) considers flange lateral bending for a skewed steel I-girder bridge during deck placement by estimating the effects of skew (Commentary C6.10.1) and overhang (Commentary C6.10.3.4) separately. In the absence of a refined analysis, flange lateral bending stress under skew effect is recommended as 69 MPa (10 ksi) for interior girders and 14 MPa (2 ksi) for exterior girders away from the end supports for a bridge with skew > 20° that uses discontinuous cross-frames or diaphragms along the bridge. Although AASHTO (2024) C6.10.1 is somewhat ambiguous, the correct interpretation seems to be that the recommended flange lateral bending stress estimate in exterior girders near skewed bridge supports is 7.5 ksi when there are discontinuous cross-frames near the supports.

Overhang brackets transfer eccentric loads, resulting in lateral flange loading that can be approximated as a uniformly distributed lateral load F_l over the unbraced length L_b between cross-frames. The lateral force is of the opposite direction for top and bottom flanges. Figure 16 illustrates a case of the distributed load acting inward on the exterior girder bottom flange. AASHTO assumes cross-frames as effectively torsionally fixed locations of the girder for continuous and equal adjacent unbraced lengths. Considering a fixed-end beam model, flange lateral bending stress is calculated by the equation in Figure 17 (AASHTO 2024, Commentary C6.10.3.4), where S_l is flange lateral section modulus.

$$f_{l-AASHTO} = \frac{F_l L_b^2}{12 S_l}$$

Figure 17. Equation. Lateral bending stress calculation per AASHTO.

Lateral bending behavior induced by overhang load is evaluated on exterior girders in standard practice, without considering additional flange lateral bending that may result from skew effect. With a staggered cross-frame layout in skewed bridges, lateral load transfers through cross-frames to interior girders, as presented in Figure 16. The controlling girder flange lateral bending moment is then the greater one from exterior and interior girders, loaded gravitationally by concrete dead load and laterally by overhang brackets, both of which are amplified by the skew effect.

Loading Scenarios

Deck placement was simulated in one continuous phase across the bridge, which is an unrealistic simplification for longer bridges that require phased deck pours, but it is slightly conservative (i.e., yields larger stresses, particularly near middle piers) and streamlines comparisons. To evaluate both local (deck overhang) and global skew effects on bridge lateral behavior at various girder cross-sections, results from two loading scenarios are presented below with concrete dead load (i) only on the overhang and (ii) on the full deck area (Figure 18). Overhang loading–induced flange lateral bending is primarily due to local skew effect. Full loading provides a realistic complete view of flange lateral bending response, with a primary contribution from the global skew effect.

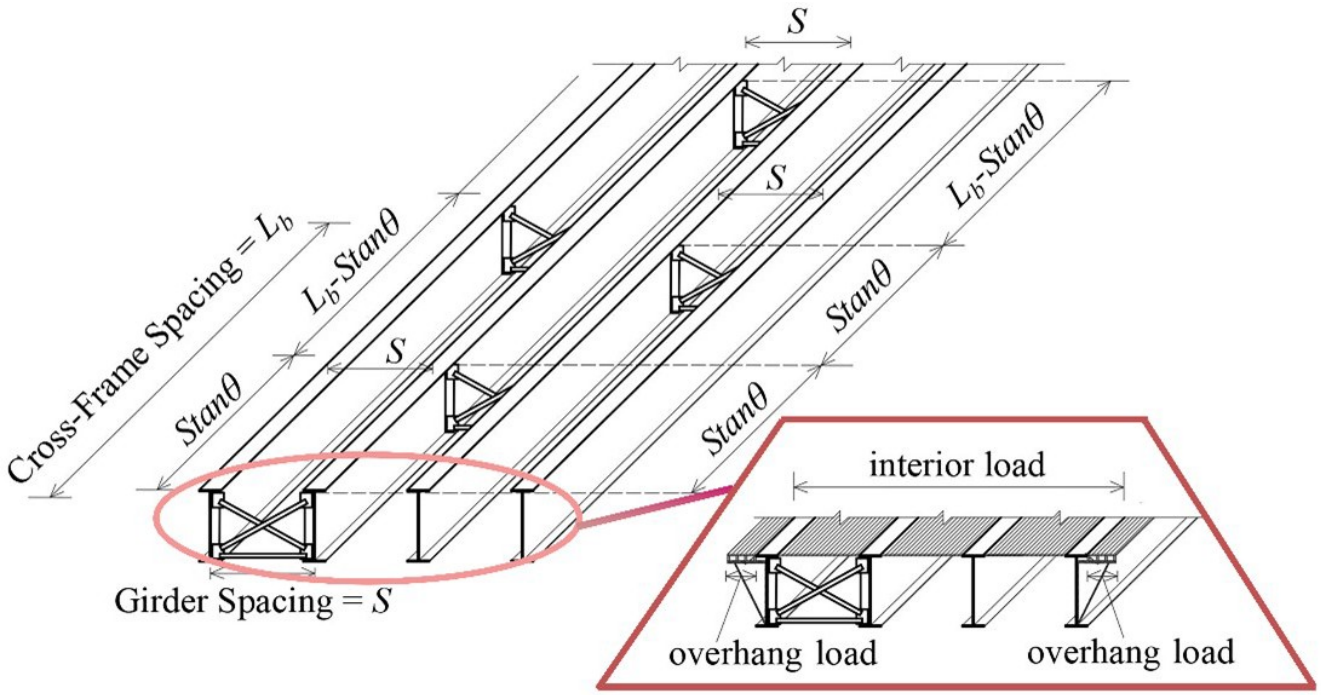

Figure 18. Illustration. Geometry and load of a typical skewed bridge.

Parametric Study Bridges

For the Mattis Avenue Stage I bridges, eight skew variations were considered—0°, 20°, 30°, 45°, 50°, 60°, 65°, and 70°—for a total of 16 unique cases. Other bridge parameters were unchanged to provide a clear illustration of the skew effect on bridge response. The designs could be slightly different in engineering practice if bridges with skew variation were fully designed and constructed. In addition to this extended assessment of the instrumented bridges, seven more single- or two-span continuous bridges with moderate to high skew, as shown in Table 1 (total of nine bridges), were selected from a database provided by IDOT of 184 total steel bridges designed or constructed between 2005 and 2020. Bridge parameters of particular interest to the current research are included in the table, including abutment type (stub or integral), skew angle (θ), number of spans, bridge overhang width, span length (L_s) and width (w_g), and skew index (defined as $I_s = tan\theta \times w_g/L_s$). Inner cross-frames for all skewed bridges considered in the parametric study are placed in a staggered configuration perpendicular to the girder line, which is a standard preference for a cross-frame layout in modern Illinois bridge design and construction. The types of cross-frames used are listed in Table 1. The two stub abutment bridges are designed with end diaphragms placed along the skewed bearing line. Full structural plans for each bridge are publicly available through an IDOT ePlan internet search by contract number (IDOT, 2024).

Table 1. Information of Selected Bridges for Parametric Study

Name	Skew Angle	Span	Skew Index	Span Length	Bridge Width	Overhang Width
Int-0	0°	1	0.00	13 m (43 ft)	10 m (33 ft)	0.9 m (35 in.)
Int-22	22°	2	0.14, 0.14	37 m (123 ft), 37 m (123 ft)	12 m (41 ft)	1 m (41 in.)
Int-30	30°	1	0.13	40 m (130 ft)	9 m (30 ft)	0.9 m (34 in.)
Int-35	35°	1	0.29	22 m (72 ft)	9 m (30 ft)	0.8 m (31 in.)
Stub-41 (Mattis-74)	41°	2	0.48, 0.40	43 m (142 ft), 52 m (170 ft)	24 m (78 ft)	0.9 m (37 in.)
Int-45 (Mattis-57)	45°	2	0.27, 0.27	55 m (179 ft), 54 m (176 ft)	15 m (49 ft)	0.9 m (35 in.)
Int-45-single	45°	1	0.34	27 m (88 ft)	9 m (30 ft)	0.8 m (31 in.)
Int-45-multi	45°	2	0.51, 0.41	20 m (66 ft), 25 m (81 ft)	10 m (33 ft)	0.9 m (35 in.)
Stub-50	50°	2	0.77, 0.77	17 m (55 ft), 17 m (55 ft)	11 m (37 ft)	1 m (39 in.)
Name	**Girder Section**	**Girder Depth**		**Girder Spacing**	**Cross-Frame**	**Contract Number**
Int-0	W24x68	0.6 m (23 in.)		2.0 m (80 in.)	Channel	74106
Int-22	PG44	1.1 m (44 in.)		2.5 m (99 in.)	Channel	70A61
Int-30	PG60	1.5 m (60 in.)		1.8 m (71 in.)	X-shape	70534
Int-35	W33x130	0.8 m (31 in.)		1.8 m (72 in.)	Channel	74223
Stub-41 (Mattis-74)	PG70	1.8 m (70 in.)		2.2 m (85 in.)	X-shape	70B38
Int-45 (Mattis-57)	PG74	1.9 m (74 in.)		2.1 m (84 in.)	X-shape	70B38
Int-45-single	PG36	0.9 m (36 in.)		1.8 m (72 in.)	Channel	66994
Int-45-multi	PG36	0.8 m (31 in.)		2.0 m (80 in.)	Channel	74323
Stub-50	W30x148	0.8 m (30 in.)		2.2 m (88 in.)	Channel	66F57

Four of the selected bridges (Mattis-74, Mattis-57, Int-35, and Stub-50) were constructed in multiple stages, for which Stage I bridges need to be checked as separate (more slender) bridge units during construction. To allow for more variation in bridge geometry, the selected bridges were all analyzed as full bridges and half bridges. For example, bridge “Int-0” was analyzed as a full bridge (Int-0-full) and a Stage I (half) bridge (Int-0-half). The deck overhang on the interior side is usually smaller than on the exterior side in practice when a bridge is constructed in multiple stages. When a “half” bridge was analyzed in the parametric study, though, both edges of the bridge were modeled with identical overhang widths to evaluate them as individual structures comparable to real bridges, which results in somewhat smaller interior girder lateral response versus an actual half bridge. For the bridges selected from the IDOT database, 18 unique scenarios were evaluated (including the real Mattis Avenue bridges). Altogether, considering the extended Mattis Avenue bridge cases (16 bridge geometries) and the IDOT database bridge cases (17 additional bridge geometries, with half bridge Mattis-57 of 45° in both cases), 33 bridge geometries were studied in the parametric study.

NUMERICAL PARAMETRIC STUDY ANALYSIS RESULTS

Mattis Avenue Bridges with Skew Variation

Girder strong-axis bending and lateral bending behavior of skewed steel I-girder bridges was analyzed through the parametric study of the instrumented Mattis Avenue bridges with skew variations. Stresses were extracted from flange edge elements, and decomposed stress was calculated to evaluate maximum strong-axis stress (at outer flange surfaces) and lateral bending stress (at flange tips) of a girder cross-section.

I-Girder Strong-Axis Bending

Figure 19 presents the magnitude of maximum strong-axis bending stress at the bottom surface of the girder bottom flange for Mattis Avenue bridges with skew variation, including near midspan (away from supports), near the middle pier support, and near the bridge end supports (for pre-composite IABs without abutments)—all for the full-load scenarios. Larger skew leads to a slightly smaller magnitude of strong-axis bending stress, which is clearest at girder midspan locations. The general trend of the skew reduction effect is similar to that defined by the skew reduction factor for live load distribution, which is further discussed in the following chapters. This small beneficial skew effect is conservatively ignored in current design practice, so strong-axis bending stress using a standard line girder analysis (LGA) approach was identical for the bridges regardless of skew (presented in Figure 19). The ratio between strong-axis bending stress calculated using LGA and 3D FEA, for bridges with no skew, was around 1.3 (stub abutment bridge) and 1.4 (IAB) near bridge midspan, and 1.5 (stub abutment bridge) and 1.8 (IAB) near the bridge middle support. Although I-girder bottom flanges of IABs are supported by bearings at their ends that introduce transverse and longitudinal restraint, the bearings allow rotation, so strong-axis bending near an IAB's pre-composite bridge ends is of less significance compared to midspan. Stub abutment bridges have elastomeric bearings at their end supports, which were modeled with representative springs, and as a result, almost no strong-axis bending develops near the ends of those bridges.

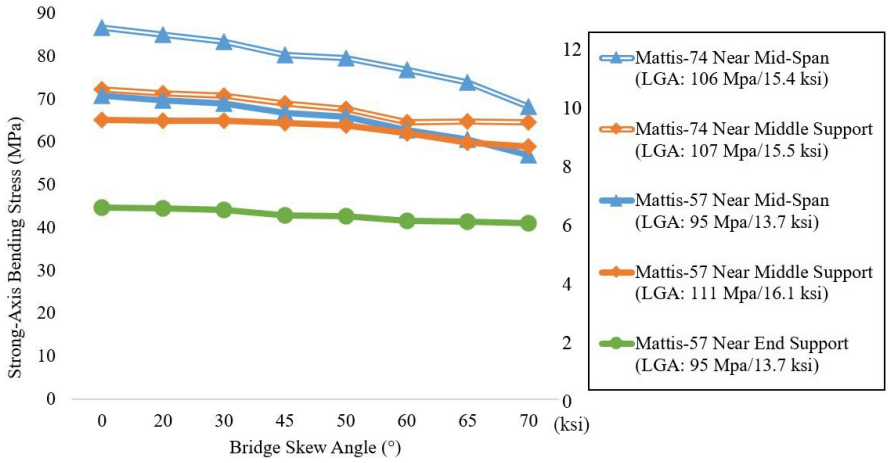

Figure 19. Graph. Magnitude of maximum strong-axis bending stress—Mattis Avenue bridges with skew variation.

I-Girder Lateral Bending Near Midspan

Figure 20 presents the magnitude of maximum flange lateral bending stress near bridge midspan (away from the supports) for the Mattis Avenue bridges studied numerically with skew variation, including the response of all girders under full concrete dead load and exterior girder response under only overhang load, which is related to the AASHTO (2024) approach for determining the overhang effect, as shown in Figure 17. Figure 20 shows that, except for some cases in the range of 0–20° skew, the maximum lateral bending stress under full concrete dead load exceeds that induced by overhang load on exterior girders. Girder flange lateral bending near midspan of pre-composite bridges with different end boundary conditions has similar trends under the effect of skew. For both top and

bottom flanges, lateral bending stress of interior girders was larger than that of exterior girders when a bridge is skewed more than 20°, which is explained by local amplification from the skew effect at cross-frames, as presented in Figure 16.

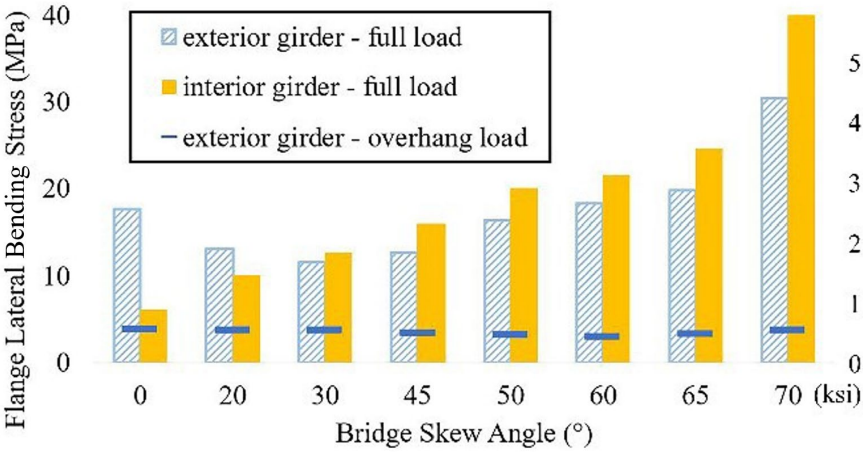

A. Mattis-74 top flange

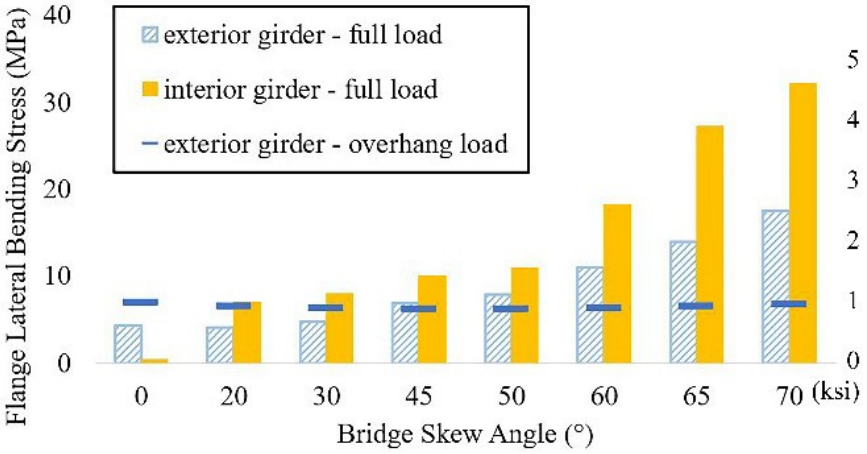

B. Mattis-74 bottom flange

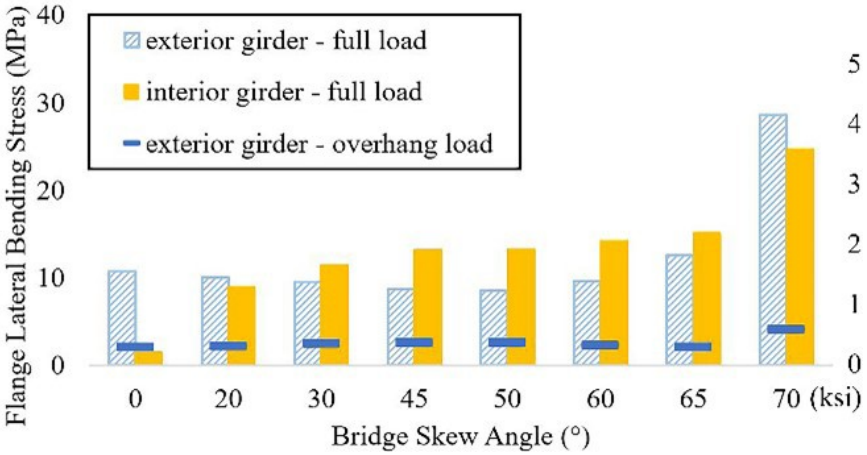

C. Mattis-57 top flange

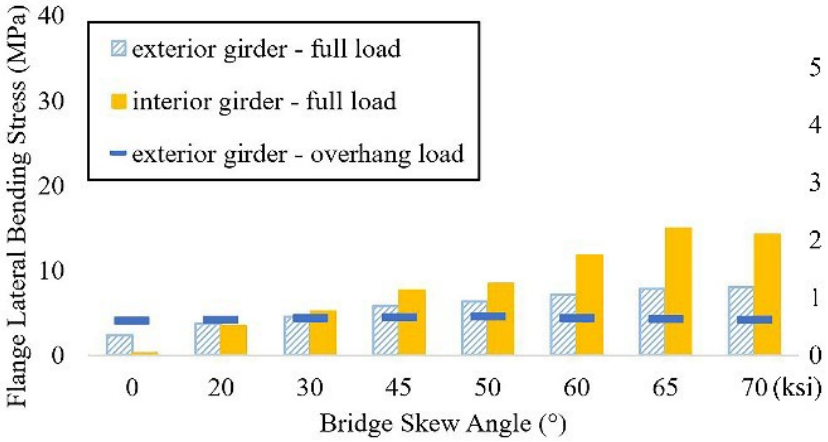

D. Mattis-57 bottom flange

Figure 20. Graph. Magnitude of maximum lateral bending stress near bridge midspan—Mattis Avenue bridges with skew variation.

Variations in lateral bending stress considering larger bridge skew, when the bridges were under full concrete dead load, were more significant on interior girders than exterior girders. The global skew effect similarly impacts exterior and interior girders, and the small lateral bending stress variation on exterior girders skewed between 20° and 60° indicates limited global skew effect. The larger lateral behavior of interior girders was therefore affected by skew transferring the local overhang load inward. Introducing skew (i.e., by comparing the 0° and 20° skew cases) leads to a large increase in lateral bending stress for interior girders, since the direct lateral load path across the bridge provided by aligned cross-frames is not present in the skewed condition. When a bridge is skewed more than 60°, a relatively large increase in the magnitude of flange lateral bending stress with increase of skew angle was observed. Evaluating the AASHTO skew-related suggestions of total unfactored flange lateral bending stress, the 69 MPa (10 ksi) for interior girders and 14 MPa (2 ksi) for exterior girders appear to be sufficient near midspan, except when a bridge is skewed at 70°. The suggested AASHTO lateral bending, however, is intended to capture lateral bending from all sources. In that context, lateral bending of exterior girders on bridges with skew greater than 45° is at least half of the total AASHTO lateral bending stress suggestion of 2 ksi.

I-Girder Lateral Bending Near Supports

Figures 21 and 22 present magnitudes of maximum flange tip lateral bending stress near bridge middle (pier) and end supports, respectively. Top and bottom flanges of exterior and interior girders were analyzed for the Mattis Avenue bridges with skew variation under full concrete dead load. Lateral responses of exterior girders under overhang load only are also presented. Lateral bending response observed near supports was generally larger than that near bridge midspan (shown in Figure 20), which is not clearly considered in current design guidelines. AASHTO (2024) C6.10.1 is somewhat ambiguous, but the correct interpretation seems to be that the recommended flange lateral bending stress estimate in exterior girders near skewed bridge supports is 7.5 ksi. Girder bottom flanges were observed with almost double the lateral bending stress compared to their corresponding top flanges, caused by more bottom flange restraint for a pre-composite superstructure during deck placement near supports, especially for the Mattis Avenue bridge with X-

shaped cross-frames that only had a horizontal bottom chord (but no horizontal top chord). The lateral bending stress of exterior and interior girders under full load mostly trended together. It was thus concluded that flange lateral bending stress near bridge supports was driven by the global skew effect, which induces a similar effect on exterior and interior girders, as explained in Figure 16.

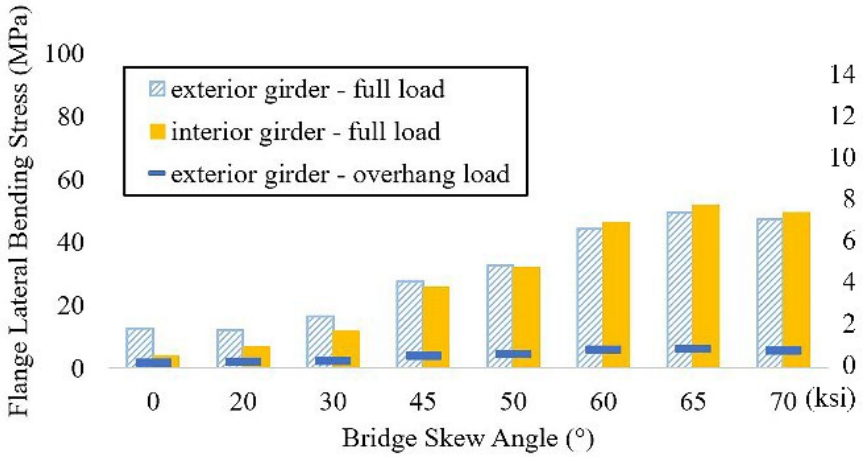

A. Mattis-74 top flange

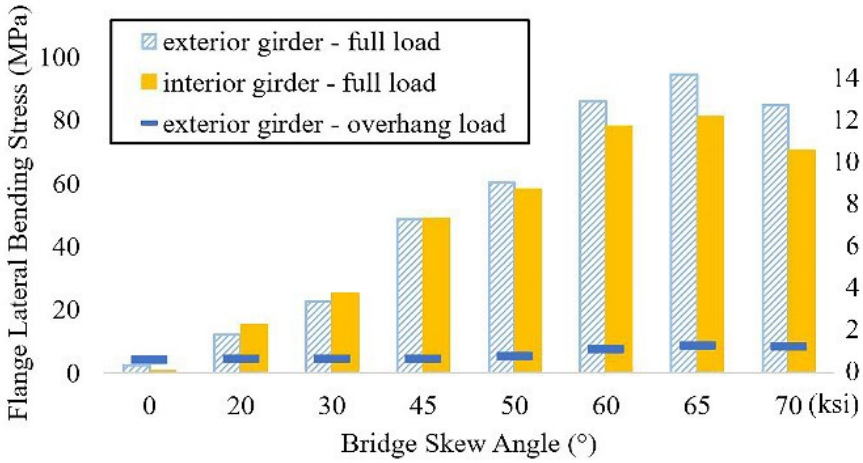

B. Mattis-74 bottom flange

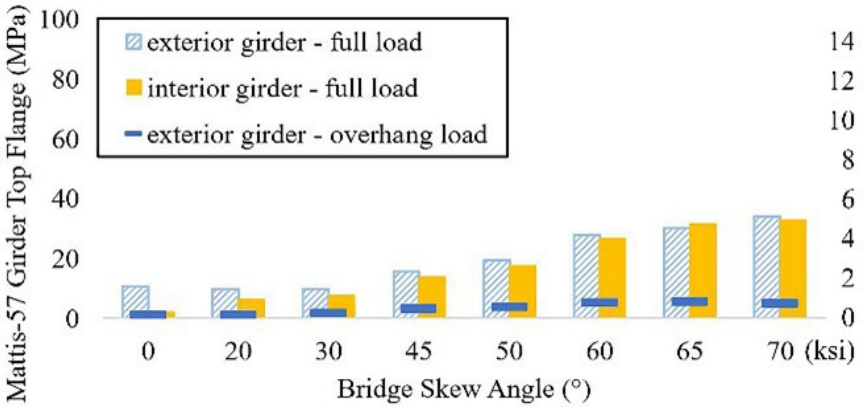

C. Mattis-57 top flange

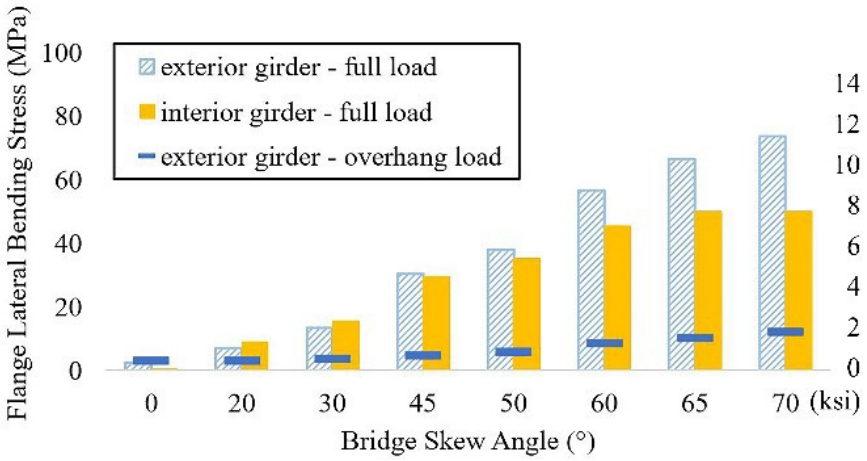

D. Mattis-57 bottom flange

Figure 21. Graph. Magnitude of maximum lateral bending stress near bridge middle support—Mattis Avenue bridges with skew variation.

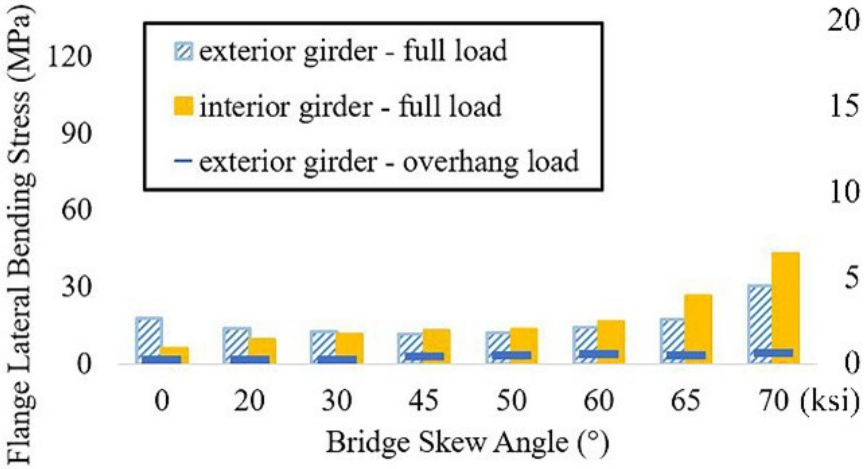

A. Mattis-74 top flange

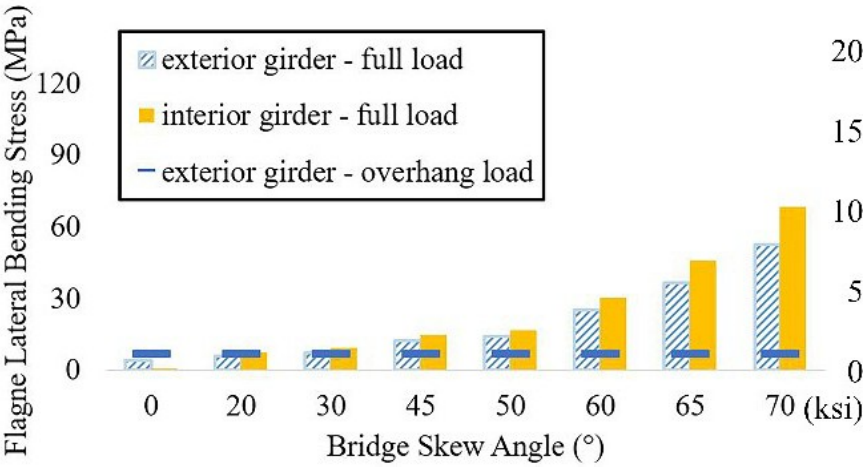

B. Mattis-74 bottom flange

C. Mattis-57 top flange

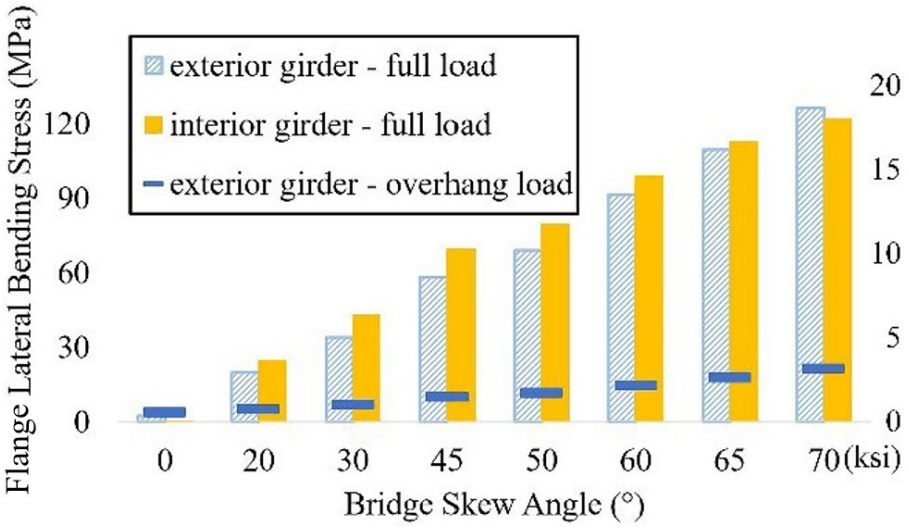

D. Mattis-57 bottom flange

Figure 22. Graph. Magnitude of maximum lateral bending stress near bridge end support—Mattis Avenue bridges with skew variation.

The AASHTO recommendation of a total unfactored flange lateral bending stress of 69 MPa (10 ksi) for interior girders might not be adequate. The suggested 52 MPa (7.5 ksi) for exterior girders with discontinuous cross-frames near supports does not appear sufficient for representing lateral bending stress caused by the global skew effect.

Figure 21 shows similar correlation between lateral bending behavior and bridge skew near the bridge middle support, regardless of bridge end support type. For a pre-composite stub abutment bridge, girder response near end supports during construction may not be specifically considered in design, while girder strength is checked according to demands near bridge midspan. However, in the parametric study, considerable flange lateral bending stress developed during deck placement at the

bridge end, even for the pre-composite stub abutment bridge when the skew is large, as shown in Figure 22. Significant lateral bending stress near the stub abutment bridge end support (more than double that near midspan, as shown in Figure 20) was observed on bottom flanges when a bridge is skewed more than 60°, as shown in Figure 22. Heavily skewed bridges should therefore be analyzed for deck placement to check girder flange lateral bending stress, including pre-composite stub abutment bridges.

Bridges from IDOT Database

A parametric study of other selected IDOT bridges was carried out to extend the findings discussed above, with a focus on flange lateral bending. Table 2 summarizes the design requirements for girder lateral bending of the selected bridges, considering overhang effect and skew effect when no refined analysis is conducted, following AASHTO (2024), which serves as a comparison with numerical simulation results of the bridges under full concrete dead load.

Table 2. Flange Lateral Bending Stress Requirements for Parametric Study Bridges

Name	Overhang Effect (C6.10.3.4)		Skew Effect (C6.10.1)
	Top Flange	Bottom Flange	Not considered (Int-0, straight bridge)
Int-0	59 MPa (8.6 ksi)	52 MPa (7.6 ksi)	All bridges with skew > 20°; interior girders, 69 MPa (10 ksi); exterior girders away from end supports, 14 MPa (2 ksi); exterior girders near end supports, 52 MPa (7.5 ksi).
Int-22	21 MPa (3.1 ksi)	14 MPa (2.1 ksi)	
Int-30	4.8 MPa (0.7 ksi)	4.1 MPa (0.6 ksi)	
Int-35	38 MPa (5.5 ksi)	29 MPa (4.2 ksi)	
Stub-41 (Mattis-74)	9.7 MPa (1.4 ksi)	6.2 MPa (0.9 ksi)	
Int-45 (Mattis-57)	6.2 MPa (0.9 ksi)	4.1 MPa (0.6 ksi)	
Int-45-single	9.0 MPa (1.3 ksi)	3.4 MPa (0.5 ksi)	
Int-45-multi	9.7 MPa (1.4 ksi)	9.7 MPa (1.4 ksi)	
Stub-50	26 MPa (3.7 ksi)	26 MPa (3.7 ksi)	

I-Girder Lateral Bending Near Midspan

Lateral bending stress on the top and bottom flanges for models of the selected IDOT bridges (properties presented in Table 1) is shown in Figure 23, including the maximum stress on both exterior and interior girders. In-span lateral bending response of interior girders typically controls over that of exterior girders for bridges skewed greater than 30°. Lateral bending stress from 3D FEA was larger than the AASHTO overhang demands (shown in Table 2) for both flanges of most selected bridges with skew more than 30°.

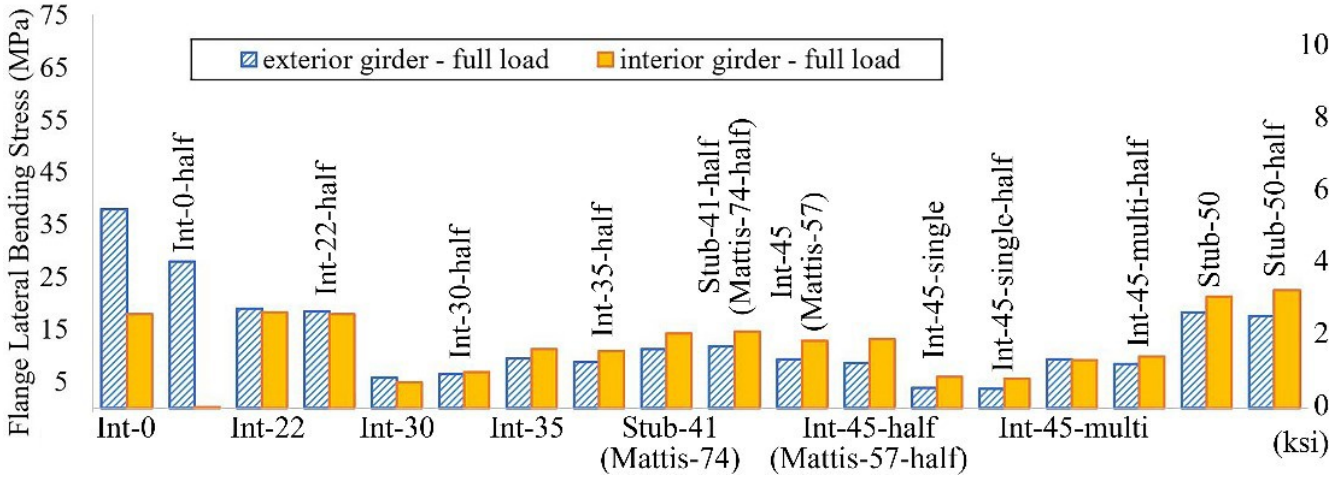

A. Top flange

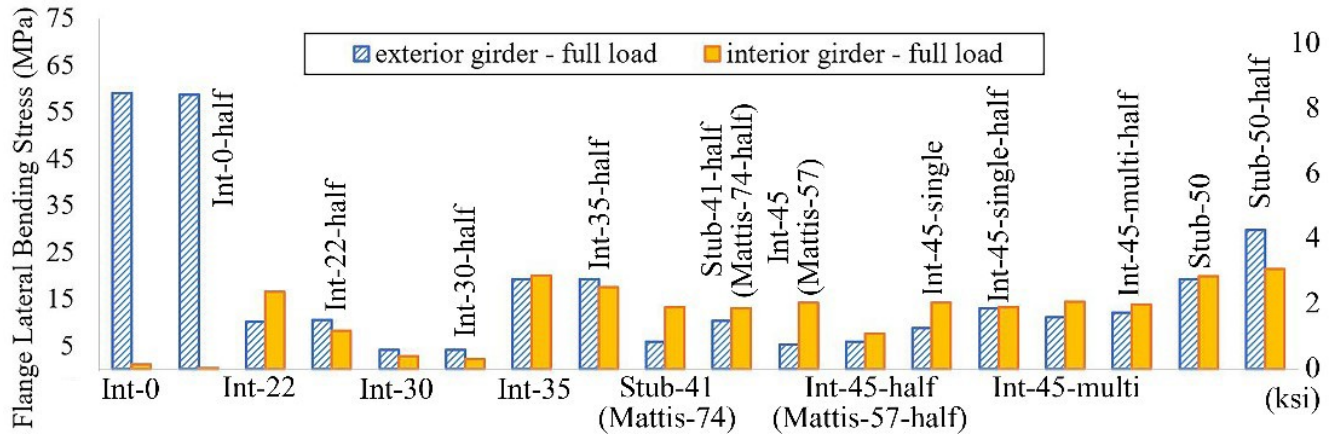

B. Bottom flange

Figure 23. Graph. Magnitude of maximum lateral bending stress near bridge midspan—selected IDOT bridges.

The AASHTO design demands considering deck overhang were mostly sufficient to estimate the total lateral bending stress from 3D FEA for a few skewed bridges (Int-45-multi, Stub-50, and Int-35) that have smaller span lengths and girder sizes compared to other bridges, as presented in Table 1. The distribution of lateral behavior between exterior and interior girders is less significant for bridges with shallower girders, and they are thus more adequate for lateral bending response near the bridge midspan when considering only overhang load on exterior girders, without taking into account any skew-induced lateral bending response. The AASHTO design demands considering skew effects are more appropriate for midspan of the IDOT bridges, which is consistent with observations based on most of the variations in the Mattis Avenue bridge parametric studies.

I-Girder Lateral Bending Near Supports

The maximum lateral bending stress from 3D FEA for the selected bridges under full concrete dead load are shown in Figure 24 (near the bridge middle support) and Figure 25 (near the ends of pre-composite IABs, without abutments). As in the Mattis Avenue bridges with skew variation, design demands considering the deck overhang were only a small portion of the total lateral bending stress near supports of the skewed bridges. The AASHTO suggested lateral bending stress with skew was more appropriate for interior girders, except for Mattis-57 near the abutments, but less so for exterior girders. Skew bridges with smaller span length (Int-45-multi, Stub-50, and Int-35) are prone to less global movement compared to other selected bridges, and, hence, skew-induced lateral bending response is less near supports for these bridges.

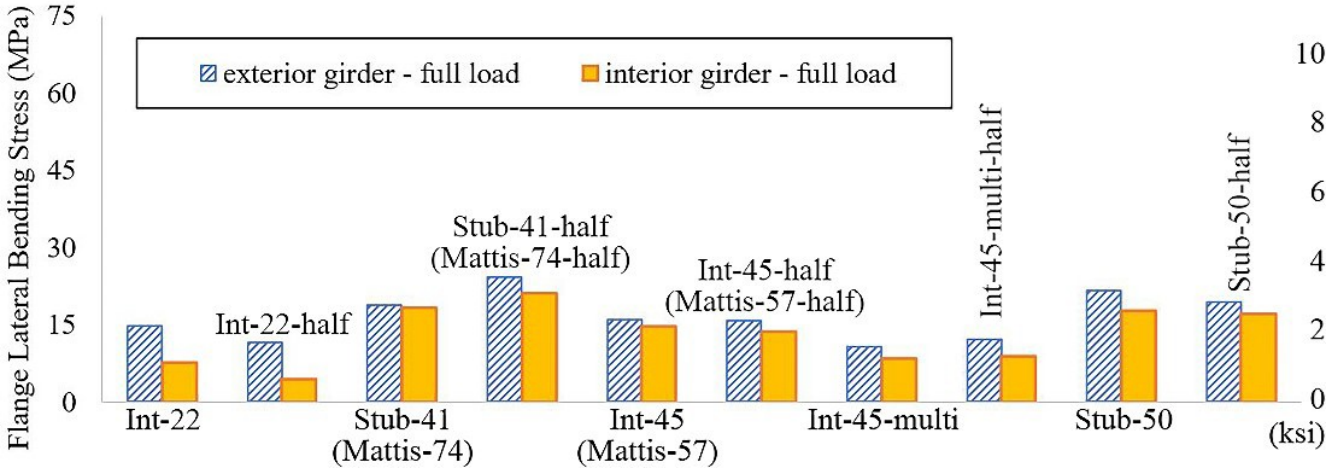

A. Top flange

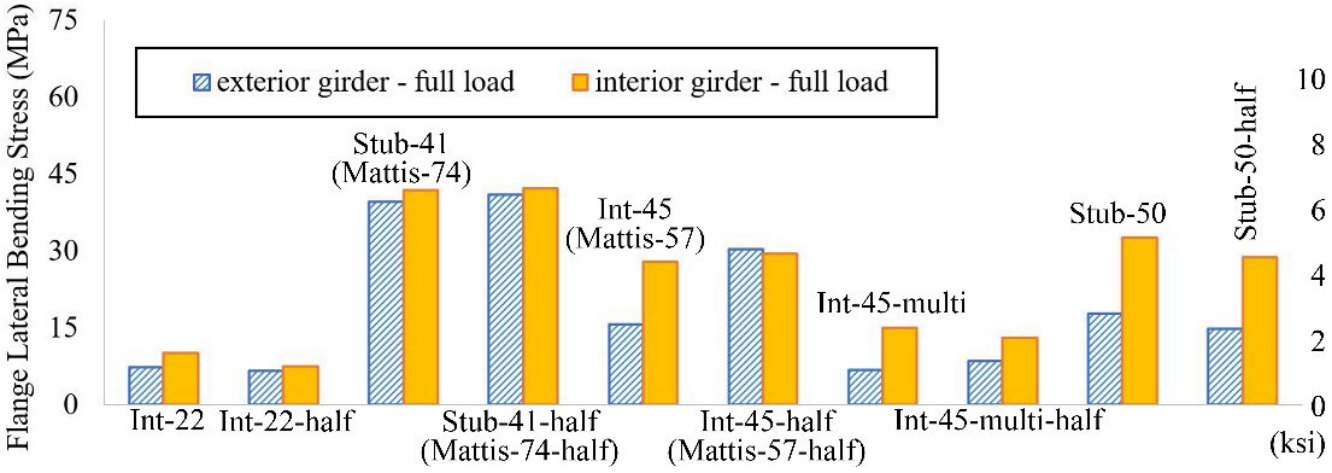

B. Bottom flange

Figure 24. Graph. Magnitude of maximum lateral bending stress near bridge middle support—selected IDOT bridges.

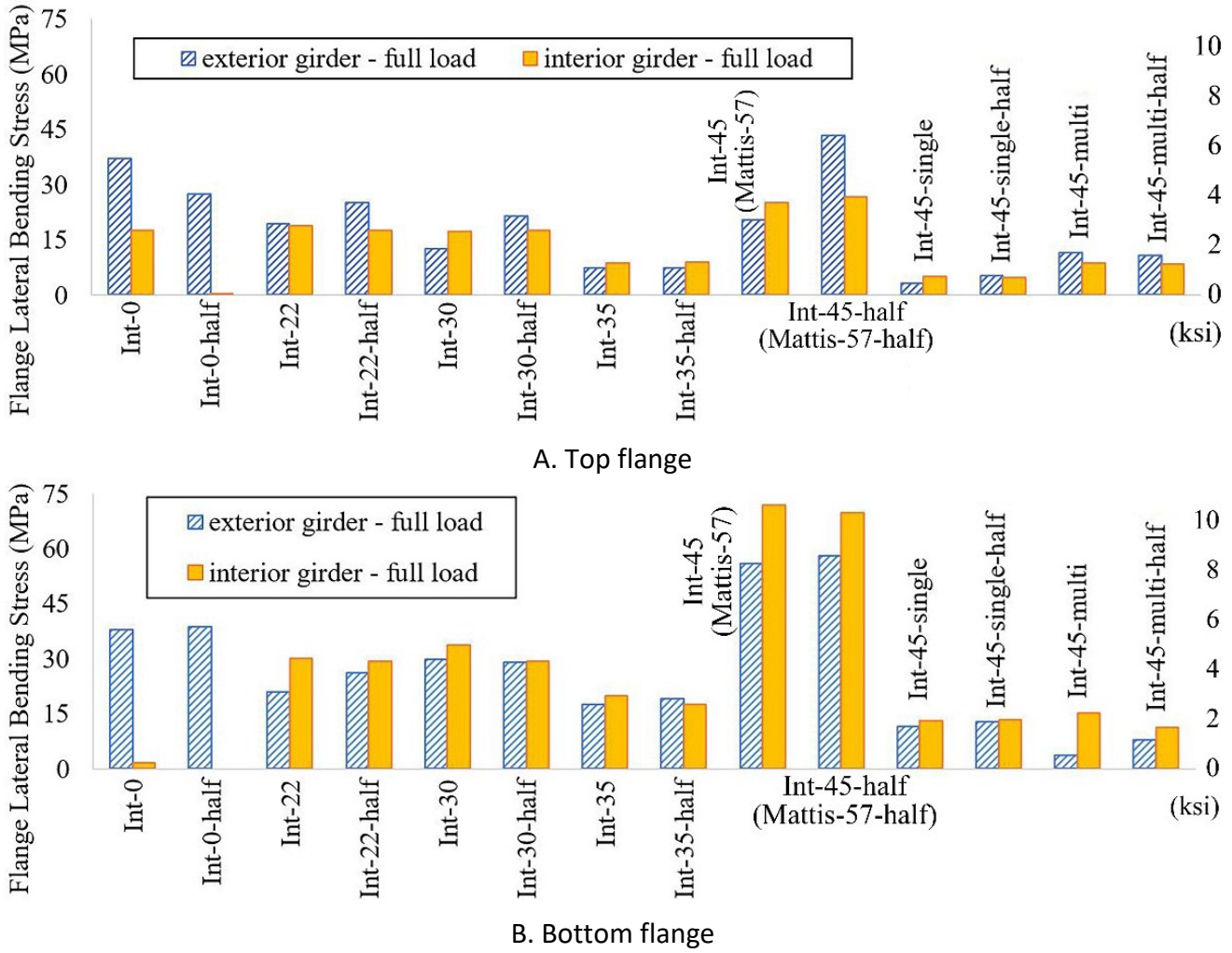

A. Top flange

B. Bottom flange

Figure 25. Graph. Magnitude of maximum lateral bending stress near bridge end support—selected IDOT bridges.

SUMMARY OF NUMERICAL PARAMETRIC STUDY RESULTS

Behavior of skewed steel I-girder bridges during deck placement was evaluated through measurements from field monitoring, numerical simulations of the monitored bridges, and parametric study analyses in this and previous chapters, with a focus on investigating girder flange lateral bending. The two instrumented Mattis Avenue bridges were analyzed with skew variation from 0° to 70° (keeping other parameters from the overall design unchanged), and seven additional real bridges from a database provided by IDOT were selected to enhance the understanding of flange lateral bending findings.

Girder flange lateral bending stress at various locations along the span was evaluated with respect to change in skew, and the skew effect was assessed through comparison with current AASHTO (2024) LRFD recommendations regarding flange lateral bending stress. Findings from the parametric study are summarized in Table 3, where the skew effect on girder flange lateral bending stress is characterized as a deck overhang (local) effect or a global effect.

Table 3. Summary of Skew Effect on Steel I-Girder Stress During Deck Placement

Location	Abutment Type	Skew Effect	Observations
Midspan	Stub, Integral	Overhang (Local)	20° < Skew < 60° results in lateral bending stress of interior girder larger than that of exterior girder.
Middle Support	Stub, Integral	Global	AASHTO C6.10.1 additional skew-related flange lateral bending stress is often not sufficient for interior girders (particularly when skew > 60°) and exterior girders.
End Support	Stub	Global	Skew > 60° develops large lateral bending stress.
	Integral	Global	AASHTO C6.10.1 additional skew-related flange lateral bending stress is often not sufficient for interior girders (particularly when skew > 45°) and exterior girders.

Near bridge midspan, flange lateral bending stress was significantly affected locally by skew, caused by the transfer of lateral load from exterior girders to interior girders through staggered cross-frames (especially for girder bottom flanges when the skew is less than 60°). Near bridge supports, girder lateral bending was primarily affected globally by bridge skew caused by rotation of the steel system about the skewed support line. AASHTO (2024) C6.10.1 provides approximate design recommendations of additional lateral bending stress for girders without refined analysis. However, the suggestions are often not adequate. Consistent with AASHTO, it is suggested that a refined method of analysis capable of considering superstructure lateral load transfer should be carried out in estimating flange lateral bending stress during deck placement, particularly when a bridge is heavily skewed. Although the findings of this study (on deck placement) are to some degree conditioned on bridge design and detailing decisions that are made in Illinois, they are expected to provide valuable insight for other states with similar practices, and they may provide focal points for future study.

CHAPTER 4: BRIDGE RESPONSE UNDER LIVE LOAD—FIELD TESTS

The need for investigating demands, load distribution, and dynamic response of skewed steel I-girder bridge superstructures is summarized in Volume I (Zhou et al., 2026). In-service skewed steel I-girder bridges studied with field monitoring have demonstrated behavior not predicted by typical methods of analysis used in design (LaFave et al., 2021; McConnell et al., 2016). AASHTO (2024) employs evaluation of girder strong-axis bending under live load by standard line girder analysis (LGA) through the live load distribution factor (LLDF) in Article 4.6.2.2 and suggests additional flange lateral bending stress for steel I-girder bridges skewed over 20° (Commentary C6.10.1), which is not strictly followed by many transportation agencies (Zhou et al., 2026). In addition to bridge static behavior, AASHTO requires a dynamic load allowance (DLA) of 33% when fatigue is not considered (AASHTO 2024, Table 3.6.2.1-1). Field data to quantify bridge dynamic response under live load are sparse (Deng et al., 2014), and very limited evaluation of DLA has been performed regarding skewed steel I-girder bridges (Almoosi et al., 2021).

To address the need to provide enhanced estimation of static and dynamic bridge response under live load and to separately investigate superstructure load distribution regarding girder major-axis and lateral bending, the two instrumented bridges were tested in the field with an isolated truck in October 2021, a few months after they were in service. The truck live load tests were conducted at 3.2, 32, and 56 kph (2, 20, and 35 mph) over multiple planned load paths. In addition to full bridge tests, the stub abutment bridge (Mattis-74) was also previously tested with an isolated truck load as a half-in-service bridge during staged construction. The data acquisition system measured the field response at 20 Hz during live load testing. A 3D finite element analysis (FEA) was conducted to computationally simulate the live load tests so that holistic information about the superstructure response could be analyzed in addition to the field measurements. Stress magnitude and distribution of girder strong-axis bending and lateral bending under various load paths were investigated, estimation using LGA was compared with the field measurements and calibrated numerical simulations, and cross-frame response was evaluated. In addition, this chapter presents an assessment of the dynamic response of the two skewed steel I-girder continuous span bridges that were evaluated based on field measurements under single vehicle loading.

FIELD OPERATIONS

The live load tests were conducted at various speeds for the full in-service bridges (Mattis-57 and Mattis-74) using the same truck: crawl (3.2 kph [2 mph]), slightly slower than normal traffic (32 kph [20 mph]), and normal traffic speed (56 kph [35 mph]). The tests on half-Mattis-74 were carried out at an earlier time (shortly after Stage I construction was complete) with a slightly different vehicle at only crawl speed (3.2 kph [2 mph]), or nearly statically. Both test vehicles were typical trucks owned by IDOT (2020). The trucks had three axles, a front axle 1 and rear axles 2 and 3 in a group, as shown in Figure 26. Detailed information about axle width, spacing, and weight is shown in Table 4. Truck 1 was used in the half-bridge tests of Mattis-74, and Truck 2 was used in the full-bridge tests. Information about the AASHTO design truck is also included in Table 4 as a comparison to the test trucks. The design truck was used for numerical parametric studies, as discussed in Chapter 5.

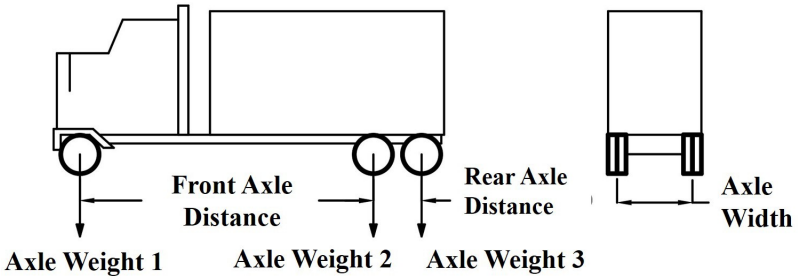

Figure 26. Illustration. Test truck configuration and loading.

Table 4. Information on Test Trucks

Truck Name	Axle Width		Axle Spacing		Axle Weight		
	Axle 1	Axles 2&3	Axle 1-2	Axle 2-3	Axle 1	Axle 2	Axle 3
Truck 1 (half-bridge testing)	1.8 m (6.0 ft)	1.8 m (6.0 ft)	6.1 m (20.0 ft)	1.2 m (4.0 ft)	54 kN (12,120 lb)	69 kN (15,460 lb)	69 kN (15,460 lb)
Truck 2 (full-bridge testing)	2.1 m (6.8 ft)	1.9 m (6.2 ft)	4.8 m (15.9 ft)	1.4 m (4.5 ft)	77 kN (17,200 lb)	91 kN (20,450 lb)	88 kN (19,750 lb)
AASHTO design truck	1.8 m (6 ft)	1.8 m (6 ft)	4.3 m (14 ft)	4.3–9.1 m (14–30 ft)	36 kN (8,000 lb)	142 kN (32,000 lb)	142 kN (32,000 lb)

The half-Mattis-74 bridge was tested along five paths, 1.5 m (5 ft) apart from each other, above the southbound traffic direction (west half of the bridge). The full bridge tests were conducted with the truck aligned along the centerline of each lane, as well as driven as close to the sidewalk or parapet as possible above the bridge shoulder. There were two above-lane tests and one above-shoulder test for both the west (southbound traffic, "-S") and east (northbound traffic, "-N") sides of Mattis-74. There was a test above the only lane and the shoulder for both sides of Mattis-57. The paths are described more specifically using the distance from the centerline of the truck to the centerline of G1 for both bridges in Table 5.

Table 5. Distance from Girder G1 to Centerline of Load Paths

Path Name	Path 1-S	Path 2-S	Path 3-S	Path 4-S	Path 5-S	Path 1-N	Path 2-N	Path 3-N
Half-Mattis-74	3.3 m (10.8 ft)	4.8 m (15.8 ft)	6.3 m (20.8 ft)	7.8 m (25.8 ft)	9.3 m (30.8 ft)	NA	NA	NA
Mattis-74	2.1 m (7.0 ft)	4.6 m (15.0 ft)	8.2 m (27.0 ft)	NA	NA	15.5 m (51.0 ft)	19.2 m (63.0 ft)	21.6 m (71.0 ft)
Mattis-57	2.9 m (9.5 ft)	5.6 m (18.5 ft)	NA	NA	NA	9.3 m (30.5 ft)	12.0 m (39.5 ft)	NA

The five load paths used for half-Mattis-74 testing are presented on a bridge cross-sectional and plan views in Figure 27, which illustrates the information presented in Table 5 (especially regarding the relative location between load paths and girders). The paths shown represent centerlines of the truck during the tests. The half bridge testing started with the truck along Path 1-S, driven from the south to north end of the bridge, and then the truck was backed up from north to south along the same path. This process was repeated for each designated path: Tests 1, 3, 5, 7, and 9 were the truck driving from south to north, and Tests 2, 4, 6, 8, and 10 were the truck backing from north to south. The tests are numbered chronologically, and the average time for each test was around 200 seconds.

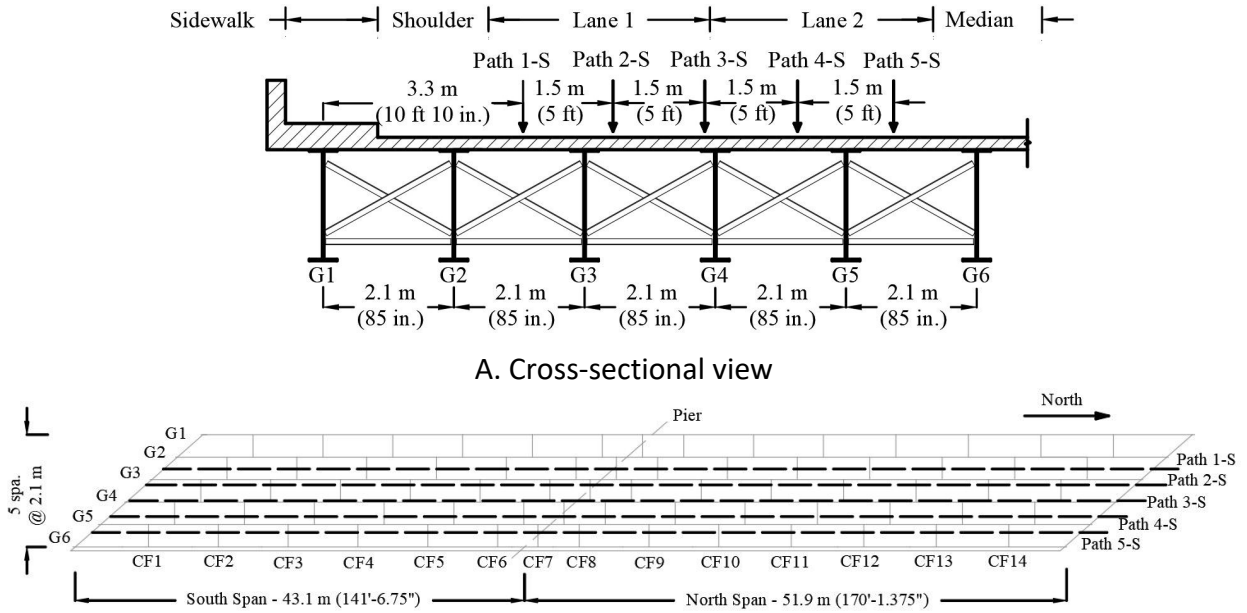

Figure 27. Illustration. Truck paths on half-Mattis-74.

Only unidirectional tests following the normal traffic direction—vehicles driving from south to north (northbound) and from north to south (southbound)—were conducted for the full bridges. Figures 28 and 29 illustrate the truck paths on the full in-service Mattis-74 and Mattis-57 bridges, respectively. Testing on half-Mattis-74 took place right before the Stage I bridge was open to traffic, and the full bridge tests were conducted at night (around 3 a.m. to 4 a.m.) with lane closures, so any adjacent traffic loading or thermal effects were considered negligible.

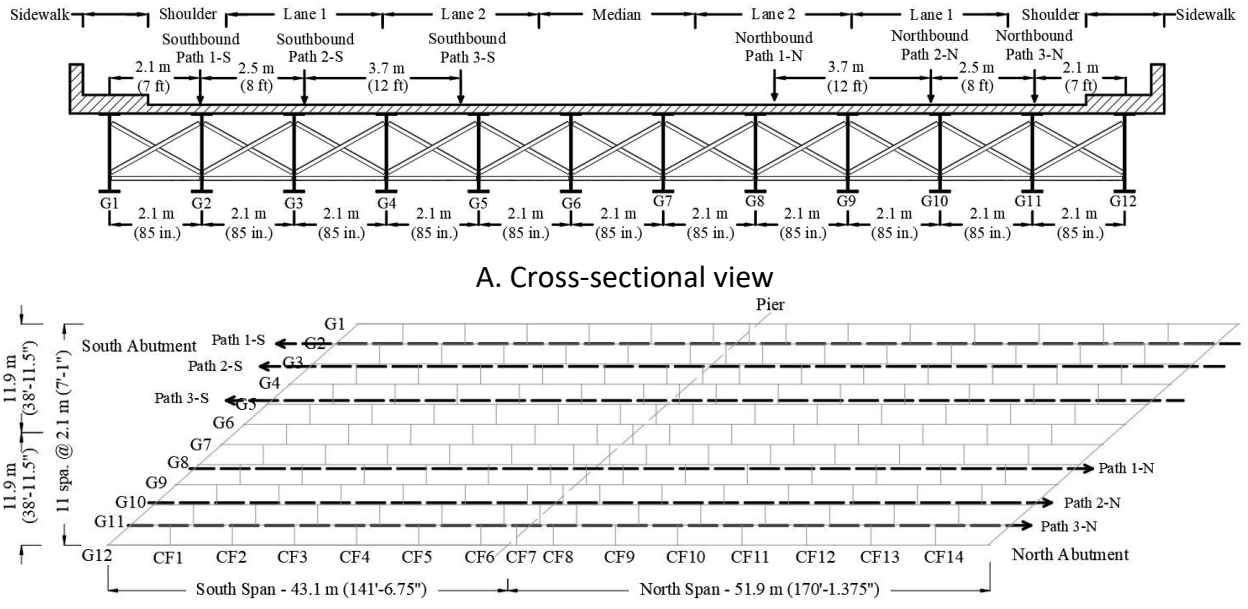

Figure 28. Illustration. Truck paths on Mattis-74.

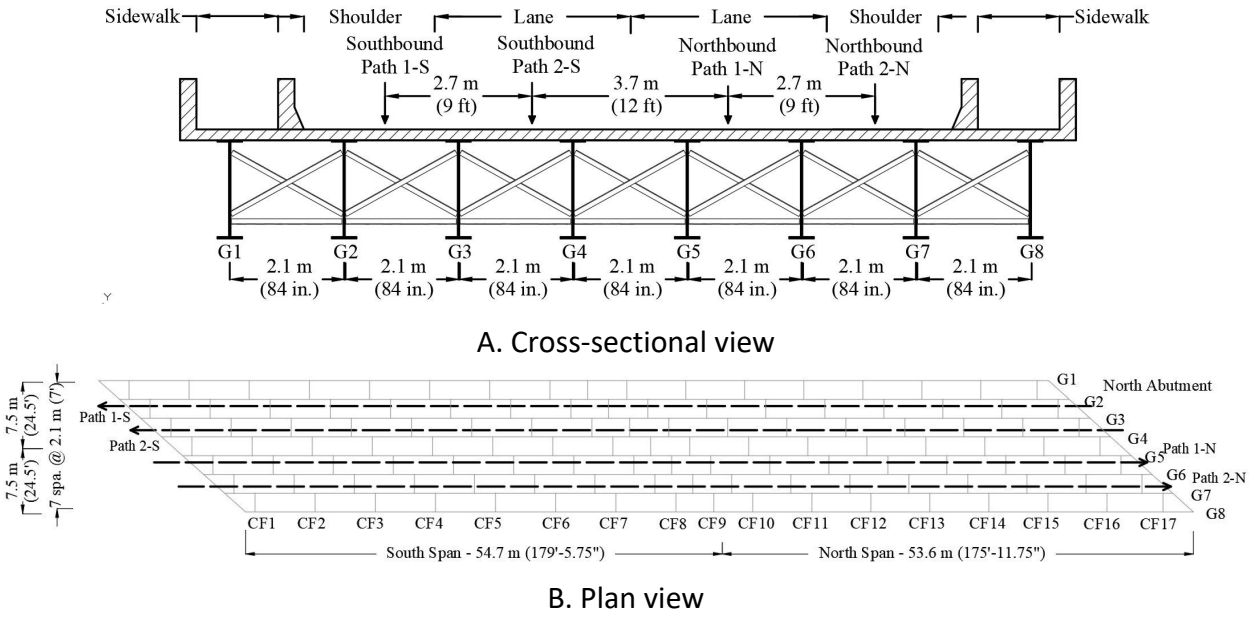

Figure 29. Illustration. Truck paths on Mattis-57.

FIELD MEASUREMENTS AND MODEL VALIDATION: HALF-MATTIS-74

This section presents an illustration of the series of live load tests with an isolated test truck for the (Stage I) half-Mattis-74 bridge and validation of numerical models with field measurements. Field data collected during truck testing were initialized at the beginning of each test, meaning the 10 truck tests (with Truck 1 driven from the south to north bridge ends and backed from the north to south bridge ends) over the five test paths (shown in Figure 27-A, Figure 27-B, and Table 5) were initialized at 10 different time stamps. The numerical model generally agreed with field measurements regarding bridge superstructure behavior. In addition, the field measurements from truck tests on half-Mattis-74 were used to validate the data post-processing scheme at an early stage of this ICT project.

Illustration of Field Measurements

Figure 30 shows typical strain measurements from the field tests and strain results extracted from numerical models for each instrumented girder cross-section, under the load path closest to the girder. Strains extracted from numerical models were generally in good agreement with measurements in the field. Comparisons at each girder cross-section regarding maximum decomposed strong-axis bending and lateral bending response are presented in the following sections. Some of the instrumented girder cross-sections were observed with non-zero final strain based on field measurements, such as the bottom flange locations of G5-S, G1-N, and G3-N, as well as BWb of G1-Pier. These non-zero net strain measurements were induced because the test truck was the first considerable load on the bridge after construction. This effect was not considered as part of the numerical modeling.

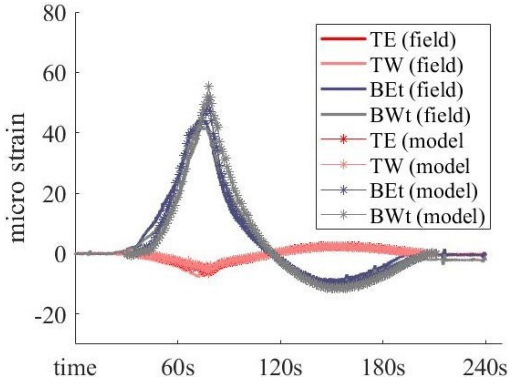

A. Cross-section G4-S, Test 7

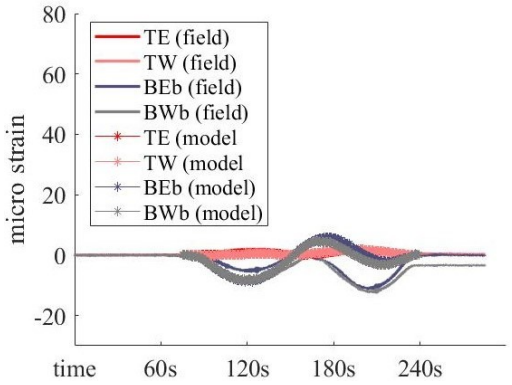

B. Cross-section G1-Pier, Test 1

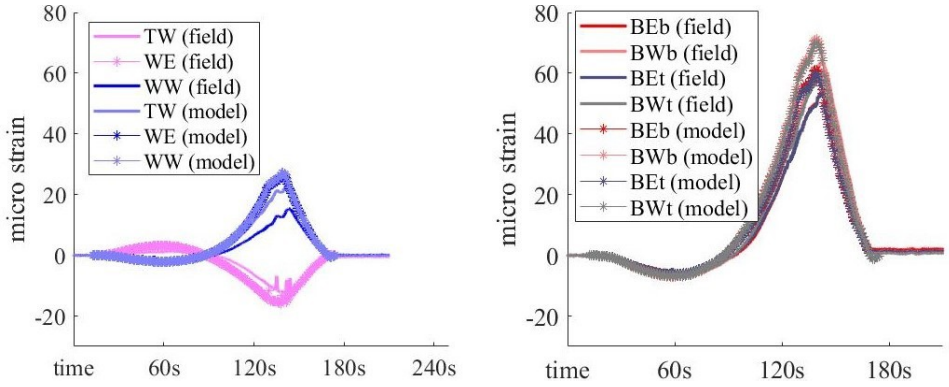

C. Cross-section G5-N, Test 9

Figure 30. Graphs. Typical comparison of field measurement and numerical modeling results of strain at instrumented girder cross-sections for critical load paths during truck tests on half-Mattis-74.

Illustration of I-Girder Cross-Sectional Behavior

Live load field test results on half-Mattis-74 were utilized to illustrate the stress decomposition method (presented in Volume I [Zhou et al., 2026]) used in this research, as illustrated in Figure 31. In the stress decomposition method for in-service bridges, the cross-sectional neutral axis (NA) location was estimated using an uncracked transformed concrete section with a tributary deck width of the girder spacing for interior girders and the sum of overhang width and half the girder spacing for

exterior girders. The assumption was assessed using bridge field data under traffic live loads during the first two years of service. The NA locations for most instrumented girder cross-sections of Mattis-74 and Mattis-57 are close to that used in design, with insignificant variations over time.

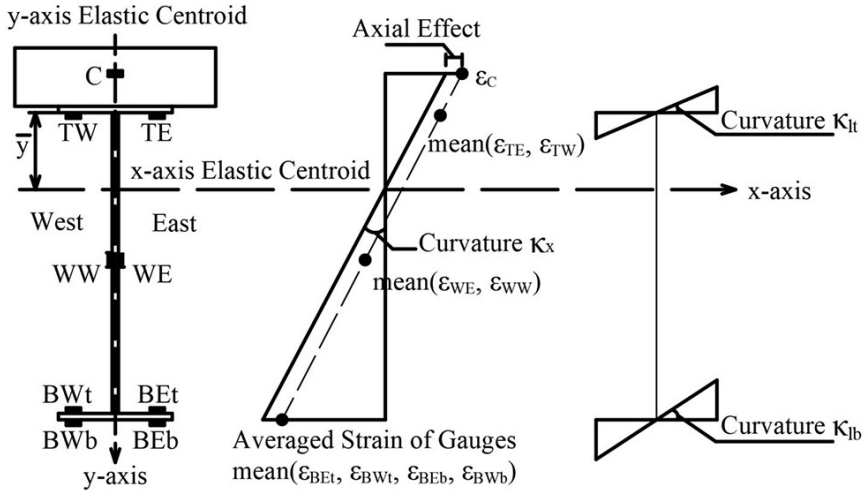

Figure 31. Decomposition illustration. Strong-axis and lateral flexure of an I-girder.

The average of the normal strain readings from two gauges symmetrically placed about the *y*-axis provides normal strain at the *y*-axis without effects from lateral bending, as shown in Figure 31. In addition to the decomposition calculation, curvature of a girder cross-section under strong-axis bending (κ_x) can also be estimated by linear regression using the averaged strain values on the *y*-axis (including concrete strain measured in the deck slab). For a heavily instrumented girder cross-section, as presented in Figure 31, the bottom flange, web, top flange, and concrete slab strains comprise a four-point regression calculation for κ_x. A simpler two-point calculation using only top and bottom flange strains can also be made when the cross-section is lightly instrumented.

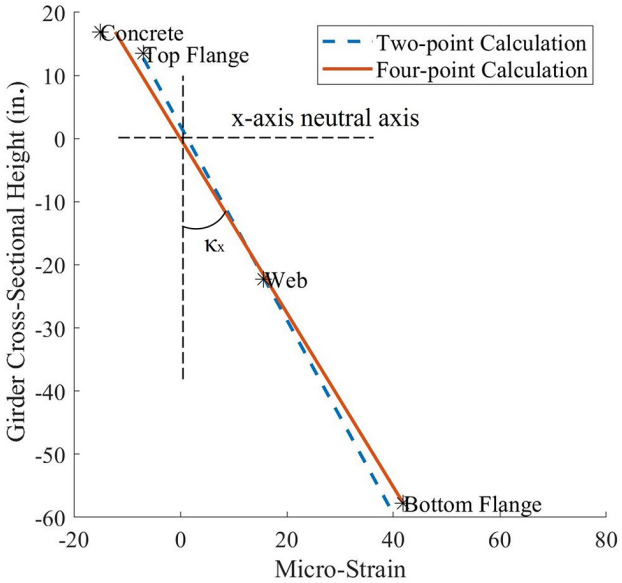

A. Strong-axis bending curvature evaluation (1 in. = 25.4 mm)

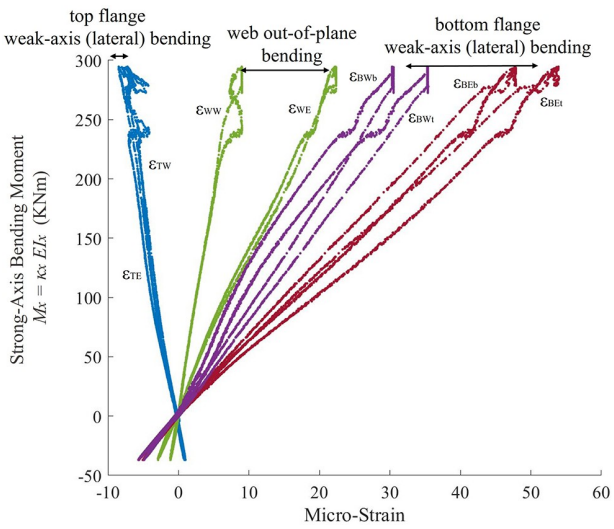

B. Strain variation vs. strong-axis bending moment

Figure 32. Graph. Cross-sectional behavior of G4-N on Stage I half-Mattis-74 during Test 6 (Path 3-S).

Figure 32-A presents the girder cross-sectional strain distribution at G4-N when the largest κ_x was measured during truck load Test 6 (over Path 3-S). The strain reading from the concrete gauge and averaged strain readings from the pairs of girder gauges along the *y*-axis are plotted at four heights for this heavily instrumented cross-section. The cross-sectional behavior evaluated using two averaged strains versus by linear regression with four strain readings are almost identical, indicating strong-axis bending curvature can be evaluated accurately even for lightly instrumented cross-sections. With strong-axis bending behavior quantified by averaged strains on the *y*-axis, the strong-axis moment can be calculated and plotted against individual gauge strains.

Figure 32-B shows moment versus strain at all gauge locations for G4-N during truck Test 6 (over Path 3-S) of half-Mattis-74. These moment versus strain relationships are predominantly linear, and separations between selected gauges indicate different types of localized behavior. Lateral bending of the girder top and bottom flanges can be observed by the difference between strain gauges on opposite (east and west) sides of the flanges, as indicated in Figure 32-B. Similarly, web out-of-plane bending behavior can be observed by the difference between strain gauges on opposite (east and west) sides of the web. In the bottom flange, the primary strong-axis bending behavior causes a strain difference between gauges on the top and bottom, where the bottom gauges are more tensile than the top (Figure 32-B). Strain differences between the top and bottom faces on the same side of the bottom flange are due to a combination of strong-axis bending and slight flange plate local bending.

Analysis and Model Validation of Girder Response

For a composite girder bridge under live load, response variation is more critical for the bottom flange than the continuously braced top flange, particularly when considering flange lateral bending and local plate behavior. The maximum field-monitored bottom flange responses due to girder strong-axis bending and flange lateral bending for each girder cross-section were calculated from truck test data, with the maximum associated stresses among the 10 truck tests shown in Figure 33.

The particular truck test during which each maximum stress component was observed is also shown in Figure 33.

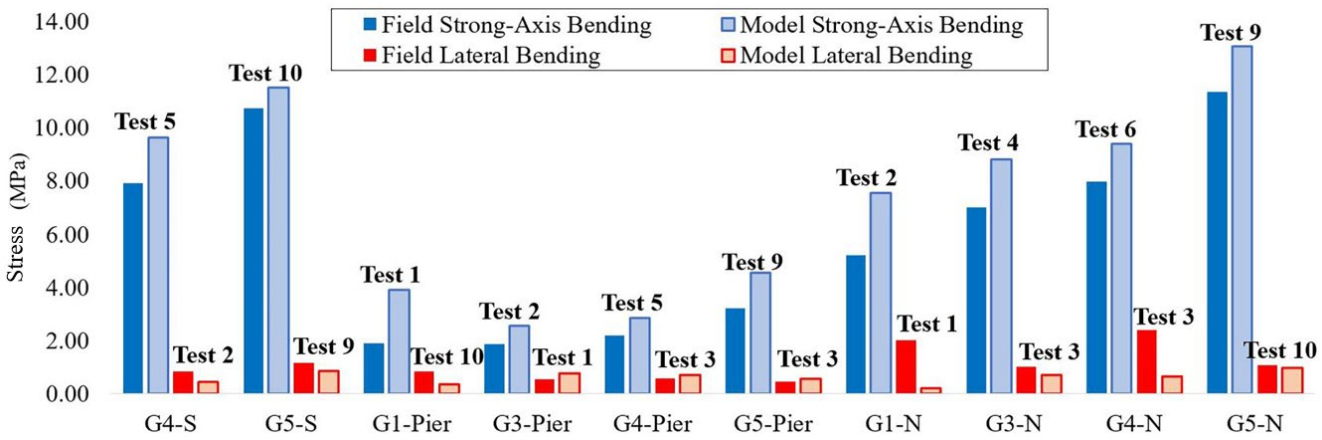

Figure 33. Graph. Maximum stress components at girder bottom flange due to strong-axis bending and lateral bending during truck testing, from field measurement and numerical simulation.

Numerical simulations were conducted for the 10 truck tests across the 5 test paths, and maximum stress components from strong-axis bending and lateral bending were compared against those from field measurements during the same truck test. In general, the numerical simulations reasonably captured the response of the bridge under live load for both girder strong-axis bending and flange lateral bending. Modest overestimation of bottom flange stress due to girder strong-axis bending could be due to modeling assumptions related to the concrete deck properties (i.e., no concrete cracking and no explicit representation of reinforcement in the models). Girder bottom flange lateral bending stresses from field measurement were close to those predicted by numerical simulations, except for G1-N and G4-N, which exhibited the largest differences between the field and models. The significant difference at G1-N is attributed to fascia girder effects, where temporary barriers and diagonal braces influenced field response and were not included in the models. The large difference at G4-N is unexpected since it is an interior girder, and other interior girder locations show closer agreement between the field and models. However, unusual behavior in the vicinity of G4 near midspan was caused by an untightened cross-frame (CF12-3&4) during the time of the live load test, which was found through a field inspection. Simply removing the ineffective cross-frame from the numerical models provided a better comparison between simulation results and field measurements at G4-N.

Analysis and Model Validation of Cross-Frame Response

Figure 34 shows typical strain measurements from field tests and strain results extracted from numerical simulations of each instrumented cross-frame for the load path closest to the bay. (Non-zero final strain was noted at the west diagonal member of CF12-4&5.) Results from numerical models were generally in good agreement with field measurements. Comparisons of normal stress within each cross-frame member among all truck tests are presented in Figure 35 (with the truck test number labeled for when the maximum value was recorded).

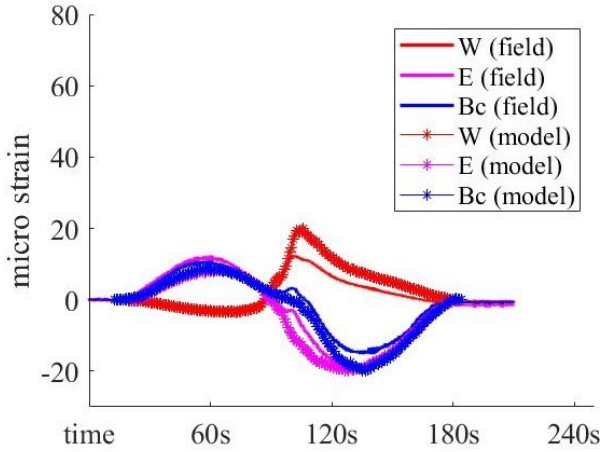

A. CF8-4&5 under Test 7

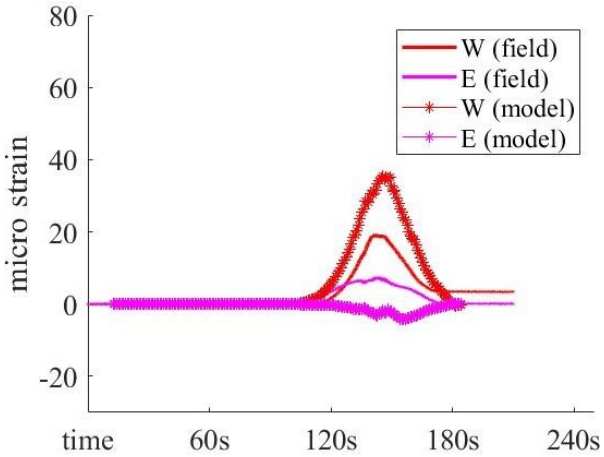

B. CF12-4&5 under Test 7

Figure 34. Graph. Typical comparison of field measurement and numerical simulation results of strain at instrumented cross-frames for critical load paths during truck tests on Stage I half-Mattis-74.

Figure 35 further illustrates a reasonably good comparison between numerical simulation results and field measurements in most cases. Maximum stresses observed in the field during truck tests at the bottom chord and in diagonal members of cross-frames were both around 8.5 MPa (1.2 ksi). However, diagonal members of cross-frame CF12-3&4 did not transfer significant stress, and the corresponding bottom chord gauge (CF12-3&4-B) location was also observed to have much smaller stress than predicted by numerical models. CF12-3&4 is the cross-frame immediately adjacent to the G4-N girder cross-section, so the unexpected responses motivated a targeted field inspection for further investigation. CF12-3&4 was observed with loose bolts (in oversized holes) between cross-frame angles and stiffener plates at several bolt locations. Thus, this partially unconnected cross-frame explains the unexpected behavior in the cross-frame and the adjacent girder. The field observations are further corroborated by a numerical model where CF12-3&4 is removed. The associated numerical simulation results are then in much closer agreement with the field data. The bolts on cross-frame CF12-3&4 were tightened shortly after the full bridge was completed, so the cross-frame was in effect for the later field tests on the full Mattis-74 bridge.

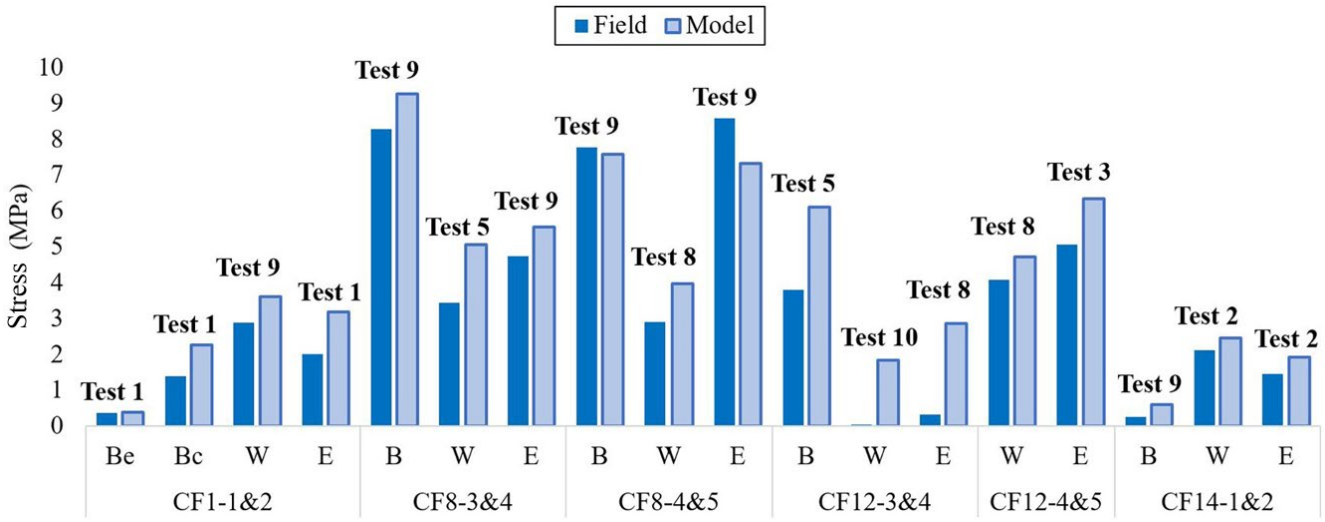

Figure 35. Graph. Maximum normal stress within cross-frame members during truck testing from field measurement and numerical simulation.

FIELD MEASUREMENTS AND MODEL VALIDATION: FULL BRIDGES

Analysis and Model Validation of Girder Response

To introduce bridge strain response evaluated through field measurements and numerical simulations, response history data of typical instrumented girder locations are shown in Figures 36 and 37 for Mattis-74 and in Figures 38, 39, and 40 for Mattis-57. These total strain measurements (before decomposition) are from field tests at three speeds and from numerical simulations under static load (using a DLOAD user subroutine in ABAQUS) with the test truck. Good agreement was achieved in general between the field strain measurements for the crawl test speed and analysis data under static truck loading. Slightly larger maximum strain was generally observed when the test truck was driven at higher speeds, which is evaluated in more detail in a later section. For the girders, strain readings were converted to stresses and then decomposed into strong-axis bending stress and lateral bending stress.

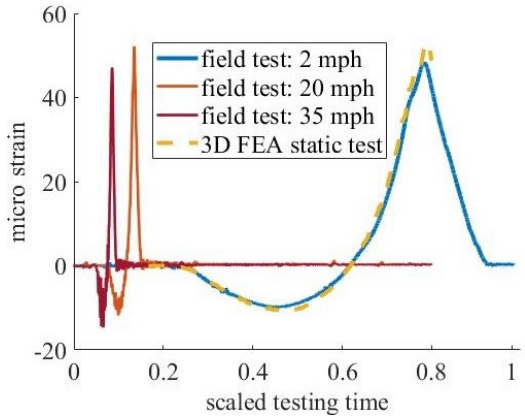

Figure 36. Graph. Typical field measurement for strain at instrumented girder cross-sections near midspan for critical load paths during the truck tests on Mattis-74: G4-S-BEt, Path 3-S.

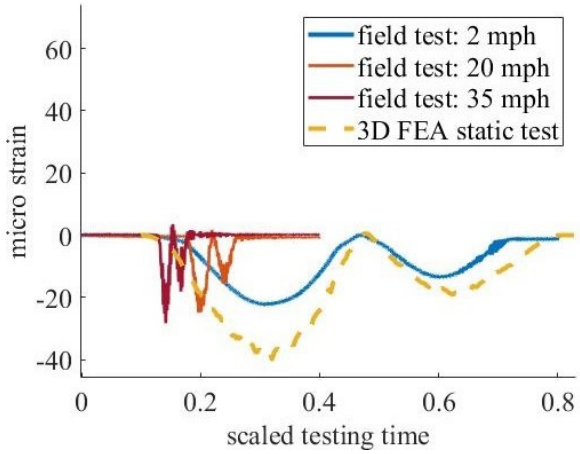

Figure 37. Graph. Typical field measurement for strain at instrumented girder cross-sections near the pier for critical load paths during the truck tests on Mattis-74: G3-Pier-TE, Path 2-S.

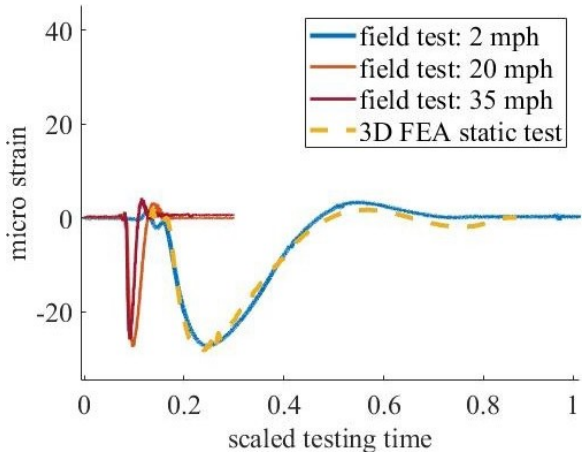

Figure 38. Graph. Typical field measurement for strain at instrumented girder cross-sections near the abutments for critical load paths during the truck tests on Mattis-57: G5-SAbut-BEb, Path 1-N.

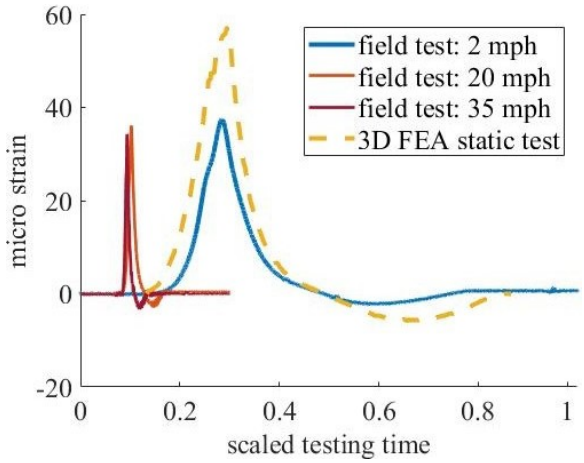

Figure 39. Graph. Typical field measurement for strain at instrumented girder cross-sections near midspan for critical load paths during the truck tests on Mattis-57: G5-S-BEb, Path 1-N.

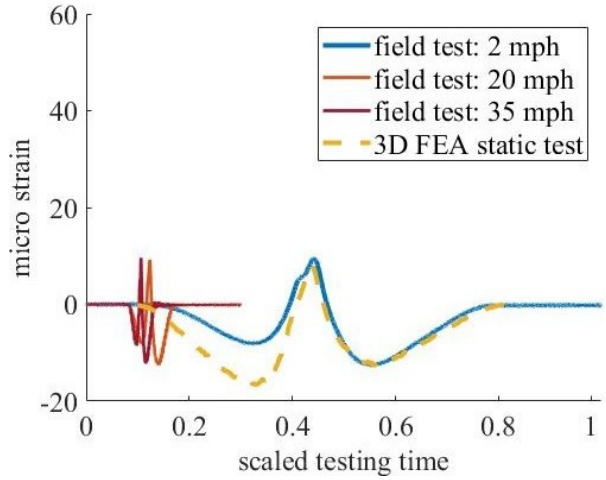

Figure 40. Graph. Typical field measurement for strain at instrumented girder cross-sections near the pier for critical load paths during the truck tests on Mattis-57: G5-Pier-S-BWb, Path 1-N.

To further illustrate the agreement between field measurements and numerical simulation results, stress envelopes (considering multiple isolated truck passes) are compared to maximum decomposed strong-axis bending stress and lateral bending stress at instrumented cross-sections (for the crawl tests). Figures 41 and 42 show the comparisons for Mattis-74 (G1 through G6) and Mattis-57 (G5 through G8), respectively. The numerical models capture the response trends observed in the field, so the numerical simulation results were used to assist in the evaluation of bridge behavior in addition to the field measurements.

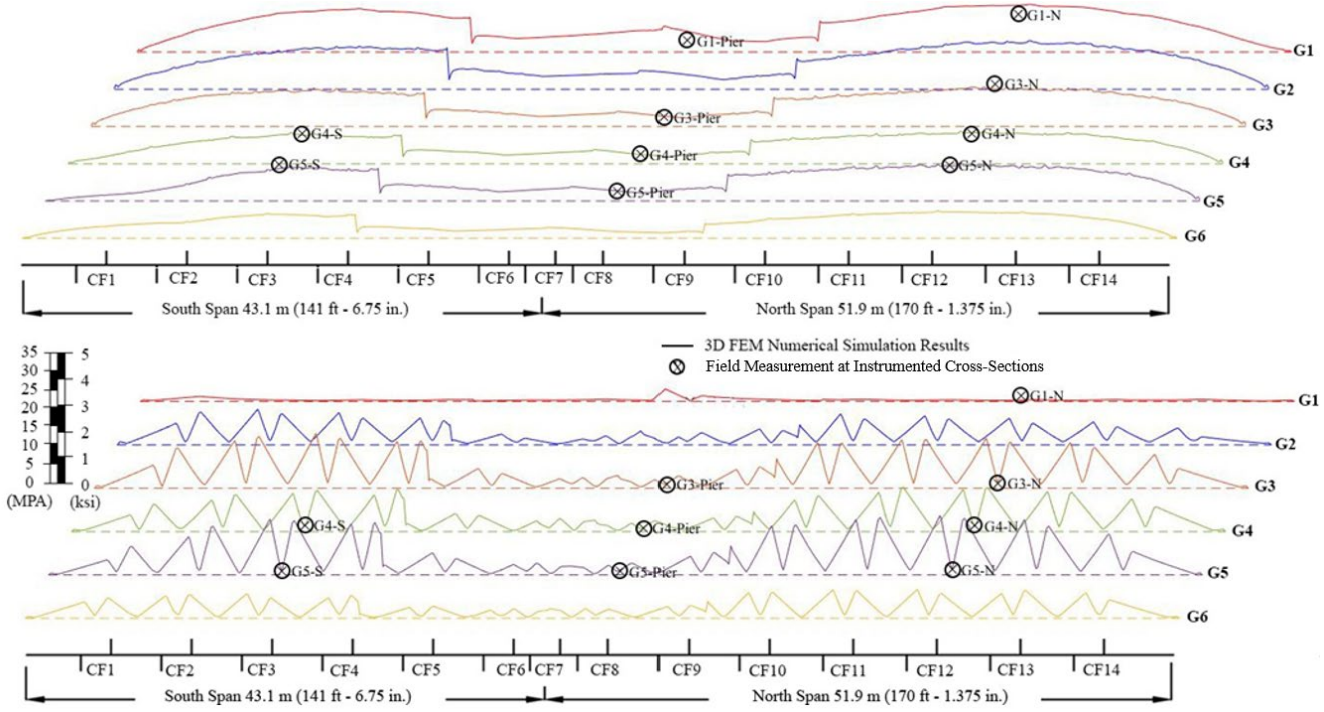

Figure 41. Graph. Mattis-74: Envelopes of girder strong-axis bending stress (top) and bottom flange lateral bending stress (bottom) for full-bridge live load tests.

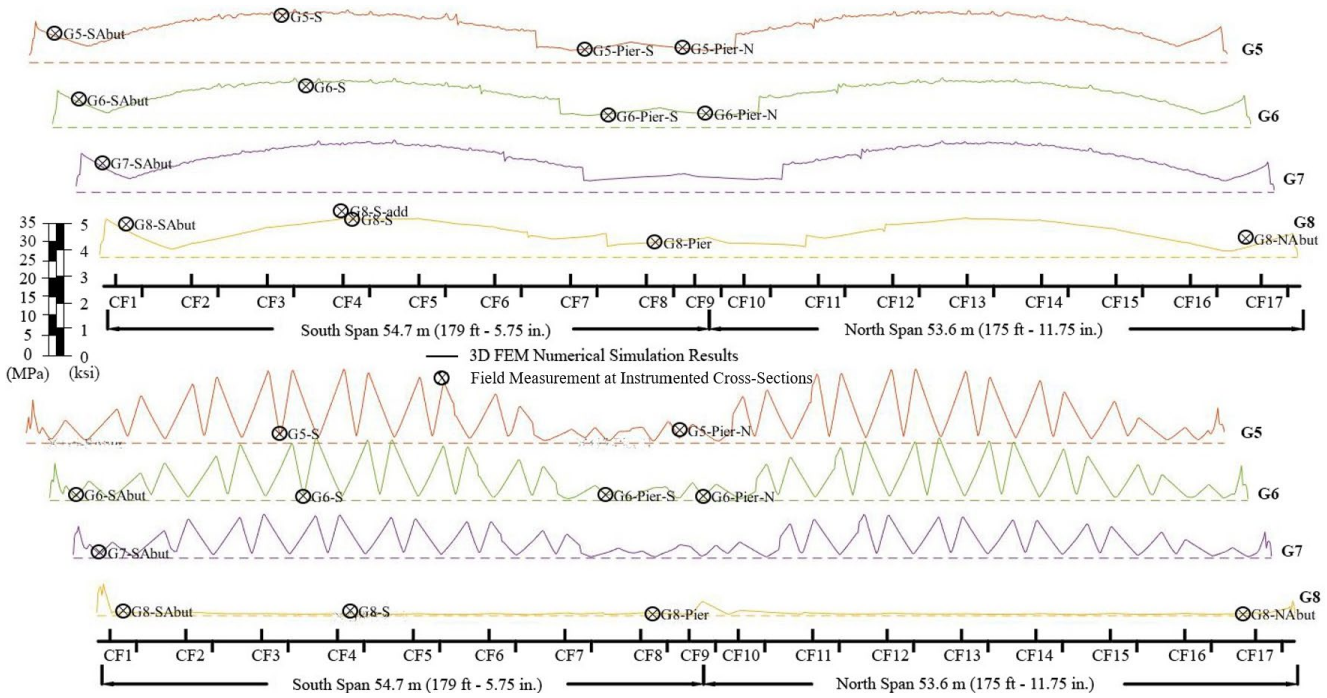

Figure 42. Graph. Mattis-57: Envelopes of girder strong-axis bending stress (top) and bottom flange lateral bending stress (bottom) for full-bridge live load tests.

Analysis and Model Validation of Cross-Frame Response

Figures 43 and 44 present the typical response history of strain measurements at three speeds and the numerical simulation results with static truck loading of a typical instrumented cross-frame for Mattis-74 and Mattis-57, respectively. Unlike girders, which were mostly observed with the largest strain measurements when the truck was closest, the most significant response of a cross-frame was sometimes not induced by a truck load closest to the bay. For cross-frame CF1-1&2 on Mattis-74, where the bottom chord was instrumented on both the connected (concentric) leg ("Bc") and the outstanding (eccentric) leg ("Be"), the strain measured on the outstanding leg was much smaller than that observed on the connected leg. The larger response on the connected leg than outstanding leg can be explained by a possible shear lag effect and bending behavior of the member. In general, good agreement was achieved between numerical simulation results and field measurements. Numerical simulation results of cross-frame response were therefore used to assist further analysis of their role in stress distribution among girders.

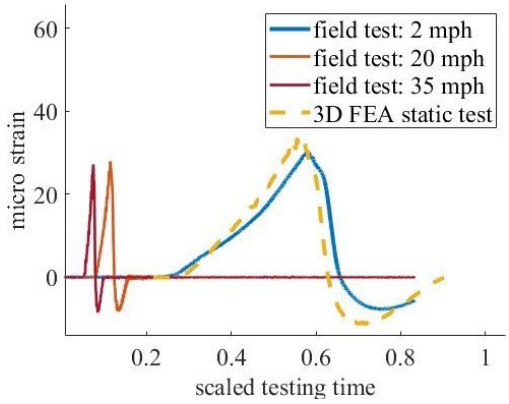

Figure 43. Graph. Typical field measurement for strain at instrumented cross-frames for critical load paths during the truck tests on Mattis-74: CF8-4&5-W, Path 3-S.

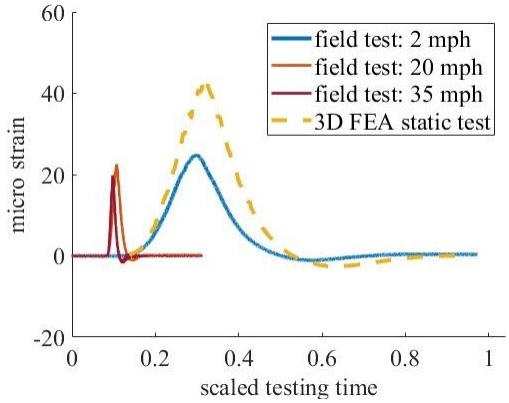

Figure 44. Graph. Typical field measurement for strain at instrumented cross-frames for critical load paths during the truck tests on Mattis-57: CF4-5&6-E, Path 1-N.

SUPERSTRUCTURE STATIC RESPONSE

Field measurements from the truck tests and corresponding 3D FEA results for the field tests have been used to evaluate the magnitude and distribution of girder and cross-frame responses, including girder strong-axis bending stress, flange lateral bending stress, and normal stress on cross-frame members. The field tests and expanded test results based on validated numerical models are then compared to calculations using line girder analysis (LGA), as a way to further investigate the efficiency of the standard design method used in bridge engineering practice.

Evaluation of Static Girder Response

Maximum strong-axis and lateral bending stress at girder bottom flanges from the validated numerical models of the isolated truck tests are shown in Figure 45 for Mattis-74 and in Figure 46 for Mattis-57. Similar results for half-Mattis-74 tests are shown in Figure 47.

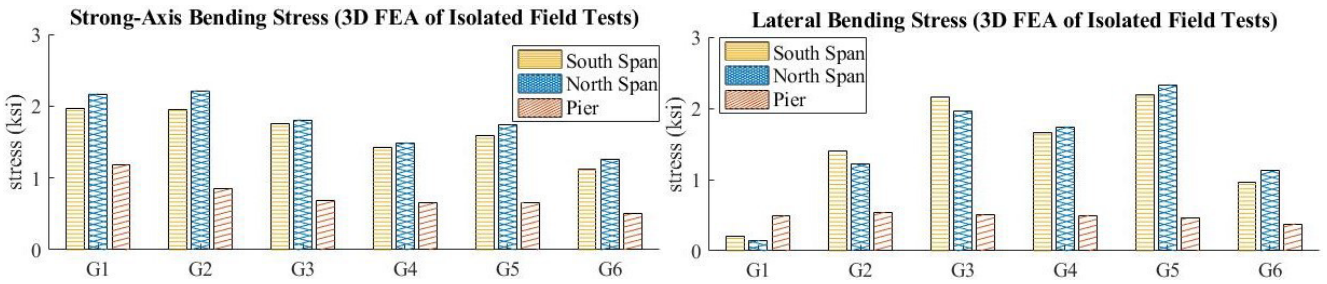

Figure 45. Graph. Maximum bottom flange strong-axis bending stress and lateral bending stress on Mattis-74 based on numerical simulations of the isolated truck live load testing.

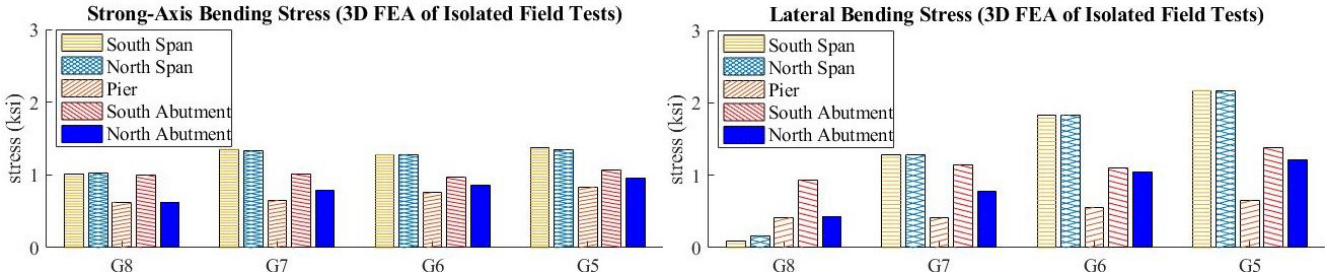

Figure 46. Graph. Maximum bottom flange strong-axis bending stress and lateral bending stress on Mattis-57 based on numerical simulations of the isolated truck live load testing.

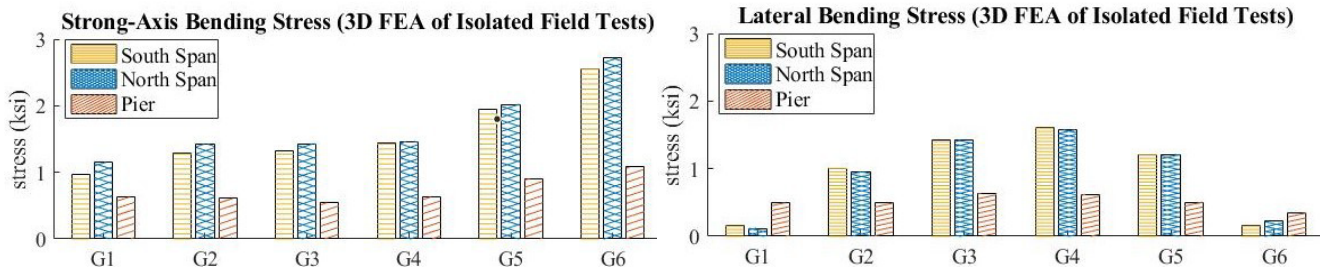

Figure 47. Graph. Maximum bottom flange strong-axis bending stress and lateral bending stress on half-Mattis-74 based on numerical simulations of the isolated truck live load testing.

The maximum girder bottom flange strong-axis bending stress under single (isolated) truck loads, based on field measurements and numerical simulation results, is compared to that calculated using LGA, considering a single girder loaded by an isolated test truck with the measured truck weight (Table 4) and applying live load distribution factors (LLDF) defined in AASHTO (2024).

LLDFs were calculated according to AASHTO Article 4.6.2.2, using an empirical equation shown in Figure 48 (AASHTO 2024, Table 4.6.2.2.2b-1) for interior girders and the lever rule for exterior girders. In the equation, S (ft) is the girder spacing, L (ft) is the span length, and t_s (in.) is the depth of concrete slab. K_g (in^4) is the longitudinal stiffness parameter, which is simplified as 1.02 (AASHTO 2024, Table 4.6.2.2.1-3) or explicitly calculated using the equation in Figure 49 (AASHTO 2024, Equation 4.6.2.2.1-1), where E_S (ksi) and E_D (ksi) are the modulus of elasticity of a girder and deck, respectively, A (in^2) is the cross-sectional area of the girder, I (in^4) is the moment of inertia of the girder, and e_g (in.) is the distance between the centers of gravity of the girder and the deck.

$$LLDF_{int} = 0.06 + (\frac{S}{14.0})^{0.4}(\frac{S}{L})^{0.3}(\frac{K_g}{12.0Lt_s{}^2})^{0.1}$$

Figure 48. Equation. Calculation of live load distribution factor.

$$K_g = \frac{E_S}{E_D}(I + Ae_g{}^2)$$

Figure 49. Equation. Calculation of longitudinal stiffness parameter.

The lever rule is used to calculate LLDF for exterior girders when an isolated (single) truck load is considered, with the truck placed at least 0.6 m (2 ft) away from the barrier or curb. As shown in Figure 50, the lever rule assumes hinges at interior girders to find the reaction at the exterior girder, by summing moments about the assumed (notional) hinge at the first interior girder (AASHTO, 2024). Mattis-74 has a sidewalk (as shown in Figure 28), and Mattis-57 also has a sidewalk with an additional barrier between the sidewalk and the shoulder (as shown in Figure 29). Both bridges had temporary barriers during staged construction under Stage I traffic. During practical bridge design procedures, the design stress of a bridge using LGA is the controlling stress of exterior and interior girders. The same LLDF is usually considered for all girders, as mentioned in Volume I (Zhou et al., 2026). The LLDF calculated using the lever rule for exterior girders would be smaller than that calculated for interior girders using the equation in Figure 48 if the sidewalks and barriers are not loaded. However, the LLDF for exterior girders (calculated using the lever rule) can be the controlling case if sidewalk regions are considered loadable during bridge design, which is often common practice (i.e., during the design of the monitored Mattis Avenue bridges).

LLDF reduction is considered for moment in skewed bridges with the equation in Figure 51, following AASHTO (2024) Table 4.6.2.2.2e-1. The factor c_1 is taken as 0 when a bridge is skewed less than 30° and calculated with the equation in Figure 52 when a bridge is skewed between 30° and 60°. When a bridge skewed more than 60° is designed with LGA, the equation in Figure 51 is used with θ equaling 60°.

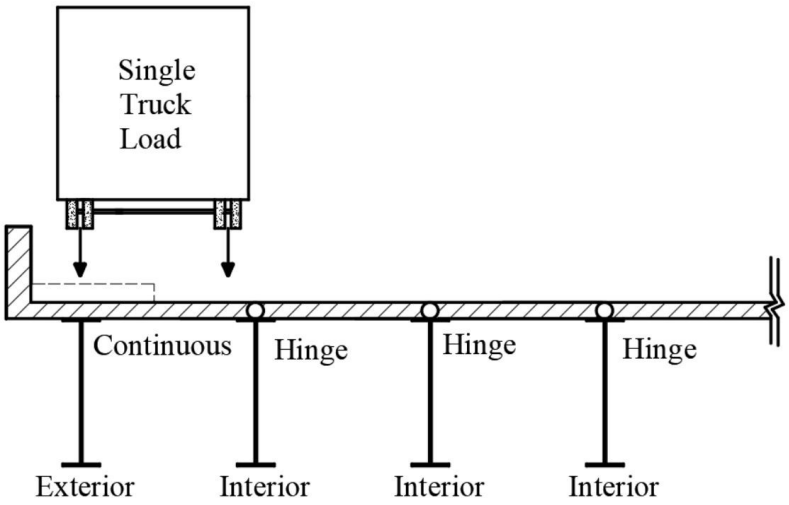

Figure 50. Illustration. Lever rule.

$$C_{skew} = 1 - c_1(tan\theta)^{1.3}$$

Figure 51. Equation. Calculation of skew reduction factor for live load distribution.

$$c_1 = 0.25(\frac{K_g}{12.0Lt_s{}^2})^{0.25}(\frac{S}{L})^{0.3}$$

Figure 52. Equation. Calculation of c_1 in skew reduction factor for live load distribution.

Table 6 presents the LLDFs of the Mattis Avenue bridges, which were specifically calculated to compare with the isolated truck tests in this research. The values might be smaller than those used for overall design of the Mattis Avenue bridges, which also consider the effect of having two or more lane loads. The calculated girder strong-axis bending stress using LGA and the calculated LLDFs are listed in the table, with loading of Truck 2 on Mattis-74 and Mattis-57 and Truck 1 on half-Mattis-74. During 1D analysis, the single girders of Mattis-74 and Mattis-57 were both represented as simply supported (roller at one bridge end and pin at the other) at their ends and continuous with a pinned support (fixed displacements) at the middle pier. IABs are generally conservatively considered as having the same boundary condition as stub abutment bridges using LGA.

Table 6. Live Load Distribution Factor for the Mattis Avenue Bridges and Strong-Axis Bending Stress Calculated Using Line Girder Analysis for the Field Tests

Location	Girder		Half-Mattis-74	Mattis-74	Mattis-57
South Span	Interior	LLDF	0.361	0.361	0.337
		Demand	15 MPa (2.2 ksi)	20 MPa (2.9 ksi)	31 MPa (3.0 ksi)
	Exterior	LLDF	0.543	0.543	0.540
		Demand	23 MPa (3.3 ksi)	30 MPa (4.4 ksi)	33 MPa (4.8 ksi)
Pier	Interior	LLDF	0.377	0.377	0.356
		Demand	10 MPa (1.5 ksi)	14 MPa (2.0 ksi)	10 MPa (1.5 ksi)
	Exterior	LLDF	0.542	0.542	0.534
		Demand	14 MPa (2.1 ksi)	20 MPa (2.9 ksi)	16 MPa (2.3 ksi)
North Span	Interior	LLDF	0.343	0.343	0.339
		Demand	15 MPa (2.2 ksi)	21 MPa (3.0 ksi)	21 MPa (3.0 ksi)
	Exterior	LLDF	0.546	0.546	0.540
		Demand	25 MPa (3.6 ksi)	33 MPa (4.8 ksi)	32 MPa (4.7 ksi)

Figure 41 shows that the maximum bottom flange strong-axis bending stress in bridge spans based on field testing with an isolated truck was 13 MPa (1.9 ksi) for Mattis-74, which is 63% and 40% of the 1D estimation using LLDF of interior and exterior girders, respectively. The maximum strong-axis bending stress in bridge spans of half-Mattis-74 was 12 MPa (1.7 ksi), as shown in Figure 33, which is 77% (using LLDF of interior girders) and 47% (using LLDF of exterior girders) of the 1D estimation. Estimating Mattis-57 with simply supported end boundary conditions introduced further conservativeness for the 1D analysis of the IAB. The maximum strong-axis bending stress of 8 MPa (1.2 ksi) for Mattis-57 under an isolated test truck (as shown in Figure 42) is less than 50% of the calculated stress using LGA, regardless of the requirement of which girder is used in the estimation. Even if the IAB is analyzed with fixed end boundary conditions using 1D analysis, the calculated stress would be 14 MPa (2.0 ksi) based on LLDF of interior girders and 22 MPa (3.2 ksi) based on LLDF of

exterior girders, which is still conservative. Field-measured maximum strong-axis bending stress is 60% (using LLDF of interior girders) and 38% (using LLDF of exterior girders) of the 1D analysis with fixed boundary conditions when analyzing Mattis-57. Near bridge supports, the measured bottom flange strong-axis bending stress was consistently smaller than that observed near bridge midspans, with the magnitude again smaller than that calculated using LGA.

The only girder that was observed with maximum strong-axis bending stress exceeding the 1D analysis using LLDF of interior girders under an isolated truck load was in the span of G6 during the live load tests on half-Mattis-74, based on numerical simulations. The maximum strong-axis bending stress in bridge spans of G6 on half-Mattis-74 was 19 MPa (2.7 ksi), as shown in Figure 47, which is 75% of the 1D analysis using LLDF of exterior girders, but exceeds by 22% the 1D analysis using LLDF of interior girders. The test truck and controlling path for G6 during the two series of tests on half-Mattis-74 and full bridge Mattis-74 were similar, so a comparison could be made regarding G6 for the two bridge geometries. G6 was an exterior girder during the half-bridge tests and an interior girder for the full-bridge tests, and it was observed with larger strong-axis bending response while functioning as an exterior girder.

Exterior girders were under sidewalks for the completed full bridges and therefore not significantly loaded during the truck tests nor directly loaded by traffic. However, G6 of half-Mattis-74 was more directly loaded due to the staged construction, as shown in Figure 28. Exterior girders are under larger strong-axis bending stress than interior girders when both are directly loaded by traffic, either during staged construction or possible bridge widening and retrofit. Calculating strong-axis bending stress under isolated truck loading with the same LLDF for all girders during LGA, which is the standard practice followed by most U.S. state agencies (as discussed in Volume I [Zhou et al., 2026]), ensures the safety of exterior girders when live load close to the exterior girders is considered, such as the special case tested in the field during the current study. However, the simplification induces conservativeness for interior girders. They are consistently observed with strong-axis bending stress less than 50% of the estimation using 1D analysis with the LLDF of exterior girders. When considering the isolated truck loading scenario, either designing exterior girders and interior girders with separate demands or considering a reduction in the LLDF calculated using the lever rule for exterior girders will help to make bridge design more efficient.

Interior girders were more critical than exterior girders regarding bottom flange lateral bending in the spans (near midspan) of both Mattis-74 (half and full in service) and Mattis-57. Based on validated numerical simulation results, maximum in-span flange lateral bending stress for the tested bridges is as large as 16 MPa (2.3 ksi) on the stub abutment bridge and 15 MPa (2.2 ksi) on the IAB for interior girders. The stress is less than 1.4 MPa (0.2 ksi) for exterior girders on both types of bridges. The AASHTO suggestion of additional lateral bending stress when lacking a refined analysis for designing skewed bridges over 20° is a lesser value for exterior girders than interior girders, which is supported by the field test findings. Near the bridge middle support, on the other hand, critical bottom flange lateral bending stress was observed to generally be evenly distributed among the girders, with a magnitude of around 3.4 MPa (0.5 ksi) for all tested bridges. Bottom flange lateral bending stress near integral abutments was also mostly the same among the girders, with a maximum magnitude (9.7 MPa [1.4 ksi]) larger than that near the pier.

Distribution of Superstructure Response

The standard LGA method evaluates a single girder, with the critical strong-axis bending response expected near bridge midspan while lateral bending stress is not considered. The distribution of strong-axis bending stress among girders is then estimated using a LLDF, as discussed above. Studying the distribution of strong-axis bending and lateral bending in the along-bridge (longitudinal) and lateral directions can help to better evaluate the effectiveness of the LGA estimation. Stress distribution of girders and cross-frames for each truck test has been studied by discretely evaluating numerically modeled strong-axis bending stress and lateral bending stress contours at cross-frame locations for girders as well as member (axial) stress of cross-frames. Contours of girder and cross-frame response for the six static (crawl speed) live load truck tests on Mattis-74 are presented in Figure 53, and the contours for Mattis-57 under the four crawl-speed live load tests are shown in Figure 54. Distribution of strong-axis bending stress at the girder bottom flange, contours for girder flange lateral bending stress at the tip of the bottom flange, and stress distribution of the larger cross-frame axial stress from the two diagonal members are presented in the figures at each cross-frame location.

The stress contours in Figures 53 and 54 further illustrate that lateral bending behavior near the bridge pier is small and mostly uniform among girders, while exterior girders are subject to less significant flange lateral bending stress compared to interior girders. The controlling girder strong-axis bending stress was observed at the girder closest to each particular truck test path, and exterior girders were observed with considerable strong-axis bending stress even under a load path that was close to the nearby interior girder. The peak stress location at the girder near a load path was also observed for cross-frame members and girder flange lateral bending stress. An exception was observed for girder bottom flange lateral bending response when the load path was close to an exterior girder.

For example, Figure 53-A shows the response distribution on Mattis-74 for load Path 1-S that is close to exterior girder G1 (and interior girder G2). Bottom flange lateral bending stress of about 9.7 MPa (1.4 ksi) is observed at both G2 and G5, but only a small lateral bending response was induced for G1. Instead of peak stress near midspan of the most directly loaded girder, such as that observed for strong-axis bending stress, the peak location regarding girder bottom flange lateral bending stress diverged from the obtuse corner in the spans. For the south span, the peak location moved closer to the middle pier, three girders away from the exterior girder, and in the north span, the peak location moved closer to the bridge end and some distance away from the load path. The other exterior load path (Path 3-N) that was near exterior girder G12 was also observed with similar behavior, as shown in Figure 53-F. The truck load along Path 3-N induced large lateral bending stress at G11 and G8, but small lateral response at G12. Peak stress locations of critical lateral response in both spans shifted away from the obtuse corners.

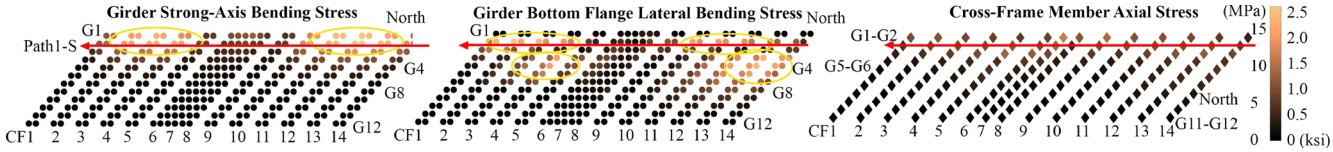

A. Path 1-S

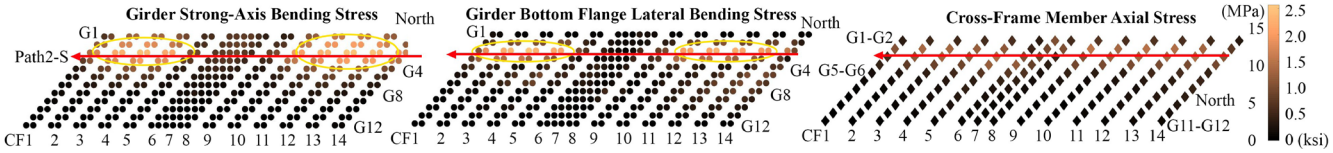

B. Path 2-S

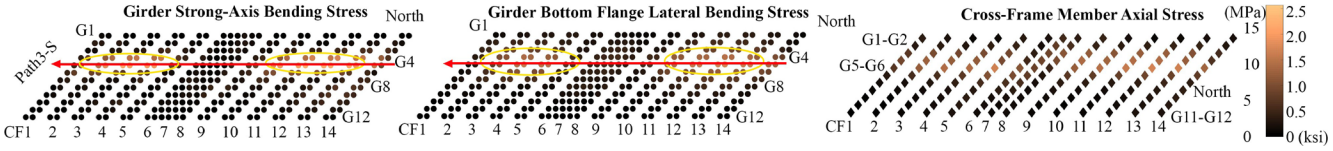

C. Path 3-S

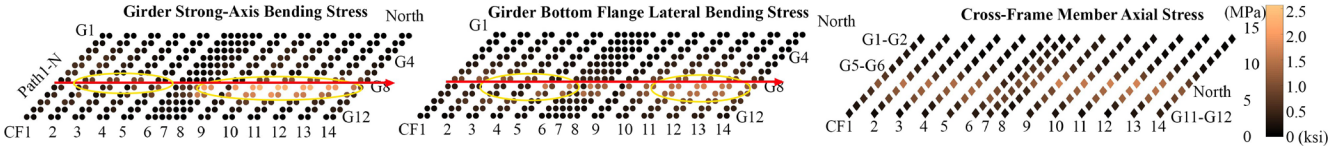

D. Path 1-N

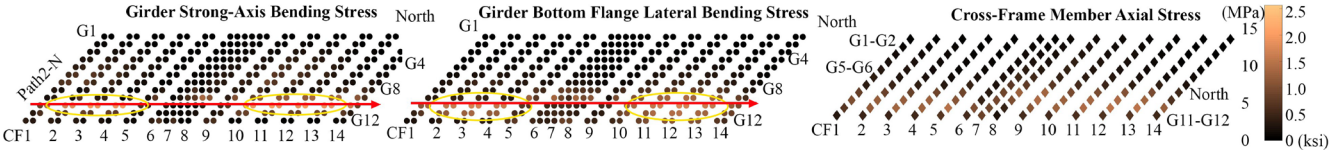

E. Path 2-N

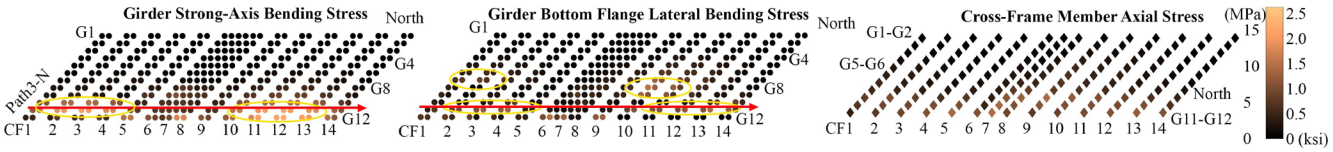

F. Path 3-N

Figure 53. Graph. Girder strong-axis bending stress, flange lateral bending stress, and cross-frame stress contours for Mattis-74.

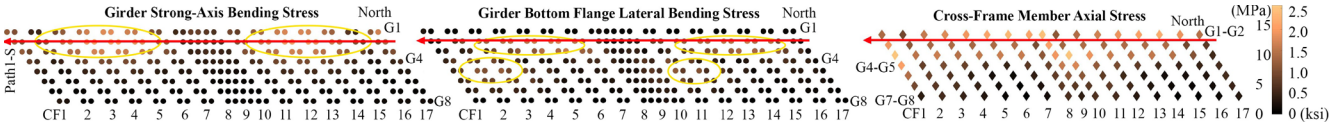

A. Path 1-S

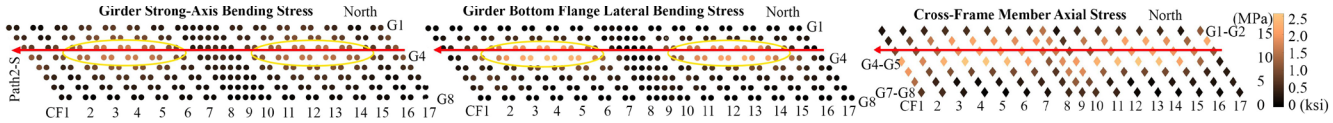

B. Path 2-S

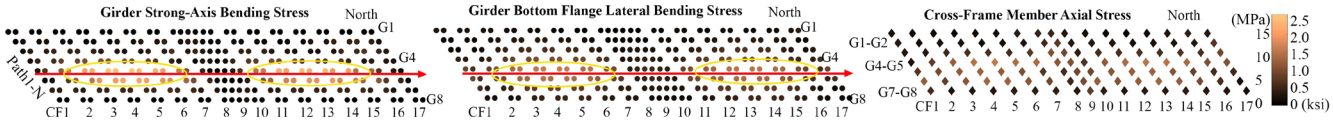

C. Path 1-N

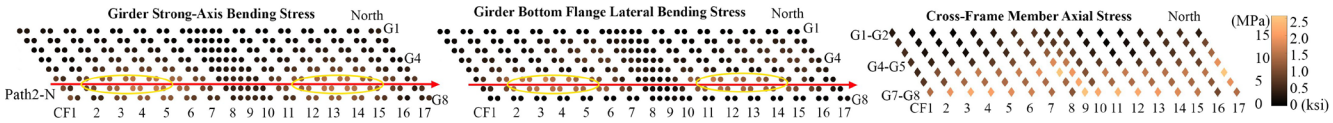

D. Path 2-N

Figure 54. Graph. Girder strong-axis bending stress, flange lateral bending stress, and cross-frame stress contours for Mattis-57.

A comparable trend of lateral load distribution can be found for Mattis-57. When the test truck was placed along Path 1-S (Figure 54-A) and Path 2-N (Figure 54-D), girder strong-axis bending response was concentrated on the girder closest to the load path, while girder lateral bending response was observed to be critical three girders away from the obtuse corner nearest to the load path. When the test truck was simulated along Path 2-S (Figure 54-B) and Path 1-N (Figure 54-C), both strong-axis bending stress and lateral bending stress were observed to be most critical at the girder closest to the load path. The distribution of lateral bending stress to an interior girder, even for a load path not adjacent to it, could induce additional lateral bending stress when a bridge is loaded with multiple trucks. Interior girders had larger lateral bending response than exterior girders for in-service bridges under live load, which further supports the AASHTO suggestion of larger additional lateral bending stress on interior girders than exterior girders for skewed bridges.

The change of peak lateral response location from close to midspan of the most loaded girder to the obtuse corner away from that girder has been illustrated by prior research. A load distribution between two obtuse corners of a skewed deck has been well explained, where a continuous load transfer could be established (Lu & Judd, 2022; Théoret et al., 2012). Cross-frames contribute to connecting steel girders together to perform as a system, especially at the bottom flange level for composite bridges. The observed bottom flange lateral load distribution following the diverged (away from obtuse corner) load path, in Figures 53 and 54, was caused by the existence of X-shaped cross-frames arranged in a staggered layout perpendicular to girders on the bridges. The cross-frames distributed the lateral load on the girder bottom flanges in a similar way to that in the deck. Girder

stress on in-service (composite) bridges with various cross-frame arrangements has been intensively evaluated in prior research. Benefits of cross-frames on bridge system-level capacity have been analyzed (McConnell et al., 2016; Radovic, 2017), and behavioral drawbacks for composite bridges under live load caused by cross-frames have been noticed. Girder stress with and without cross-frames has also been evaluated by previous studies (McConnell et al., 2020; Stallings et al., 1996, 1999; Tedesco et al., 1995).

Parametric cases were analyzed in the current research to evaluate the contribution of cross-frames for the critical load paths: Path 1-S and Path 3-N for Mattis-74 and Path 1-S and Path 2-N for Mattis-57. Total girder stress (prior to decomposition) decreased by around 20% under live load when cross-frames were excluded from the models (as theoretical case studies), which was mainly caused by the elimination of bottom flange lateral bending. Insignificant flange lateral bending stress was observed in bridge spans without the contribution of cross-frames, while slightly larger lateral bending behavior was observed near bridge supports. On the other hand, girder bottom flange stress was more concentrated on a single girder under live load, whereas the stress was more spread-out when cross-frames assisted in the load distribution. Similar to findings from previous studies (McConnell et al., 2020; Stallings et al., 1996, 1999; Tedesco et al., 1995), the deck response, reactions at supports, and girder lateral deflection increased by 10%–20% when cross-frames were not included in the analysis.

Lateral bending and strong-axis bending along a girder were compared to further study the load distribution on bridge superstructures, as shown in Figure 55. The figure presents the strong-axis bending and lateral bending stress along each girder during a test path that induced the maximum strong-axis bending stress on the girder. (The test path for each case is indicated in the figure.) The maximum lateral bending stress was much smaller than the maximum strong-axis bending stress for exterior girders and was generally larger than the maximum strong-axis bending stress for interior girders (especially for wider full bridges). Exterior girders are only observed with notable lateral bending stress near bridge supports. The distribution of critical lateral bending response (at cross-frames) mostly followed the same trend as strong-axis bending stress along a girder. Maximum lateral bending stress was observed close to where maximum strong-axis bending stress was observed.

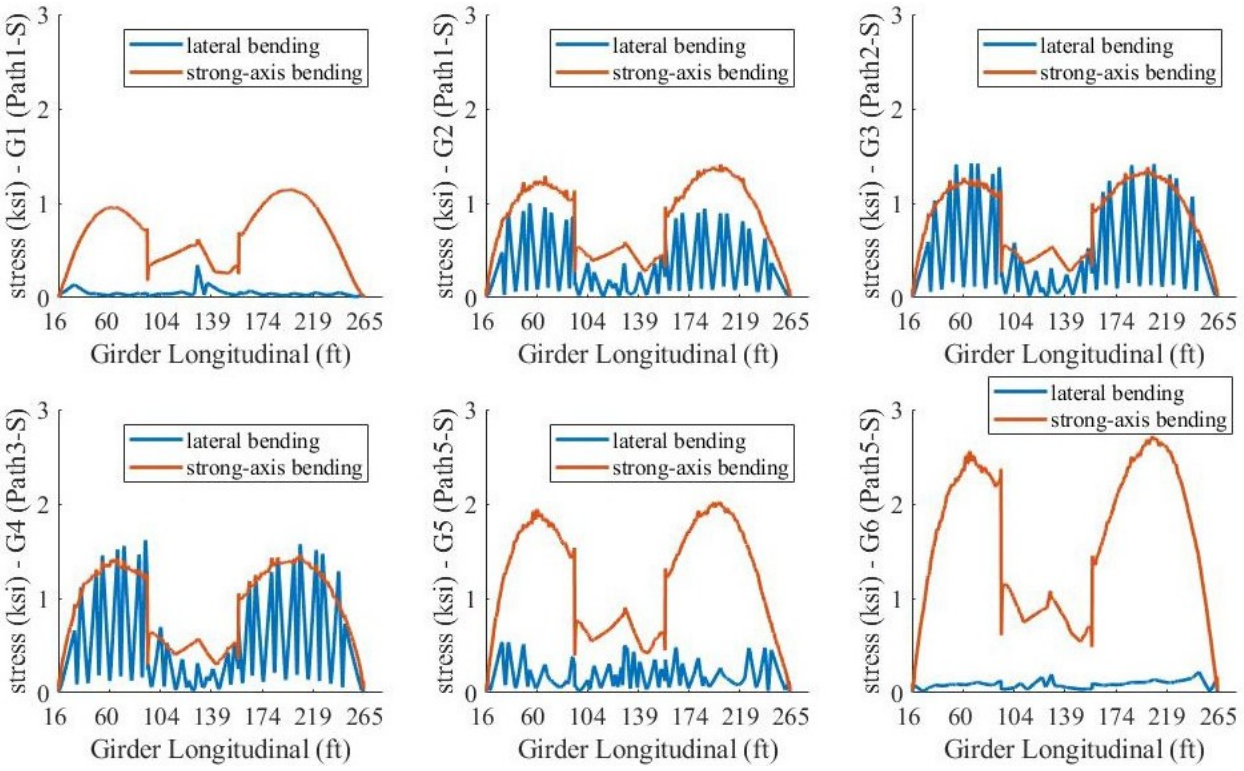

A. Half-Mattis-74

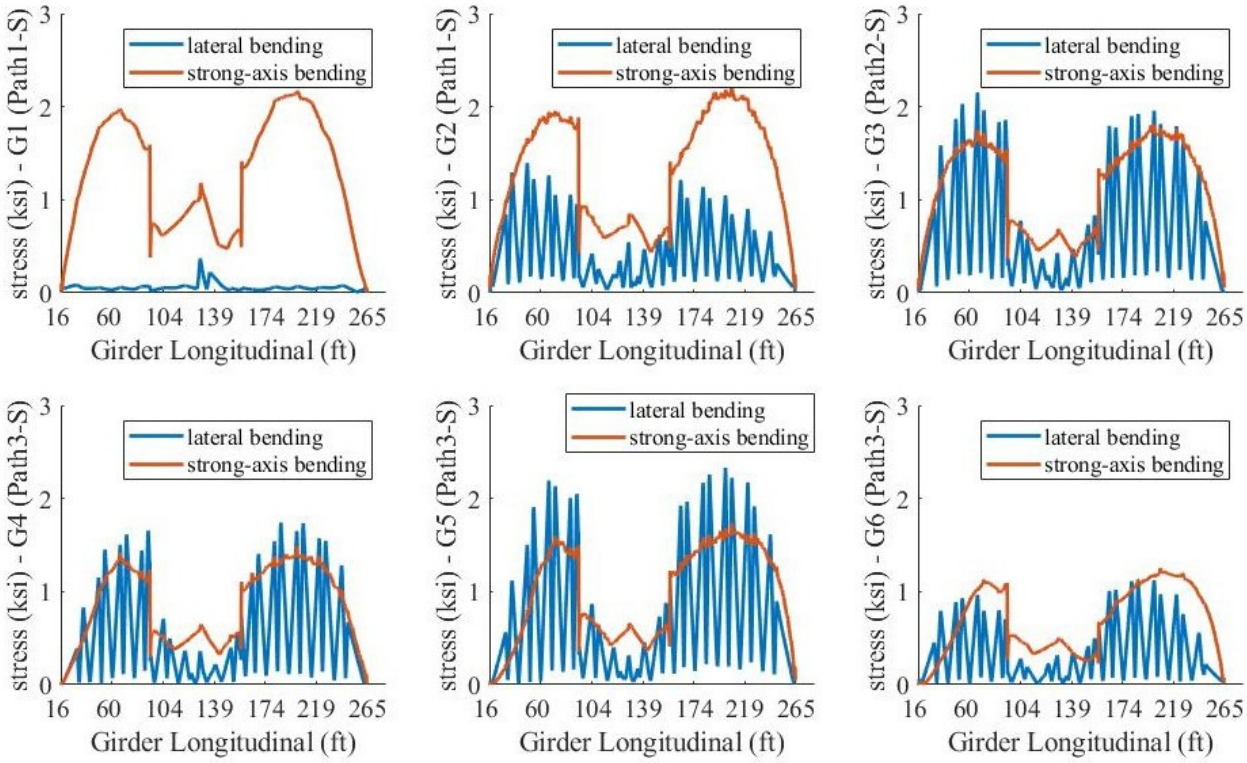

B. Mattis-74

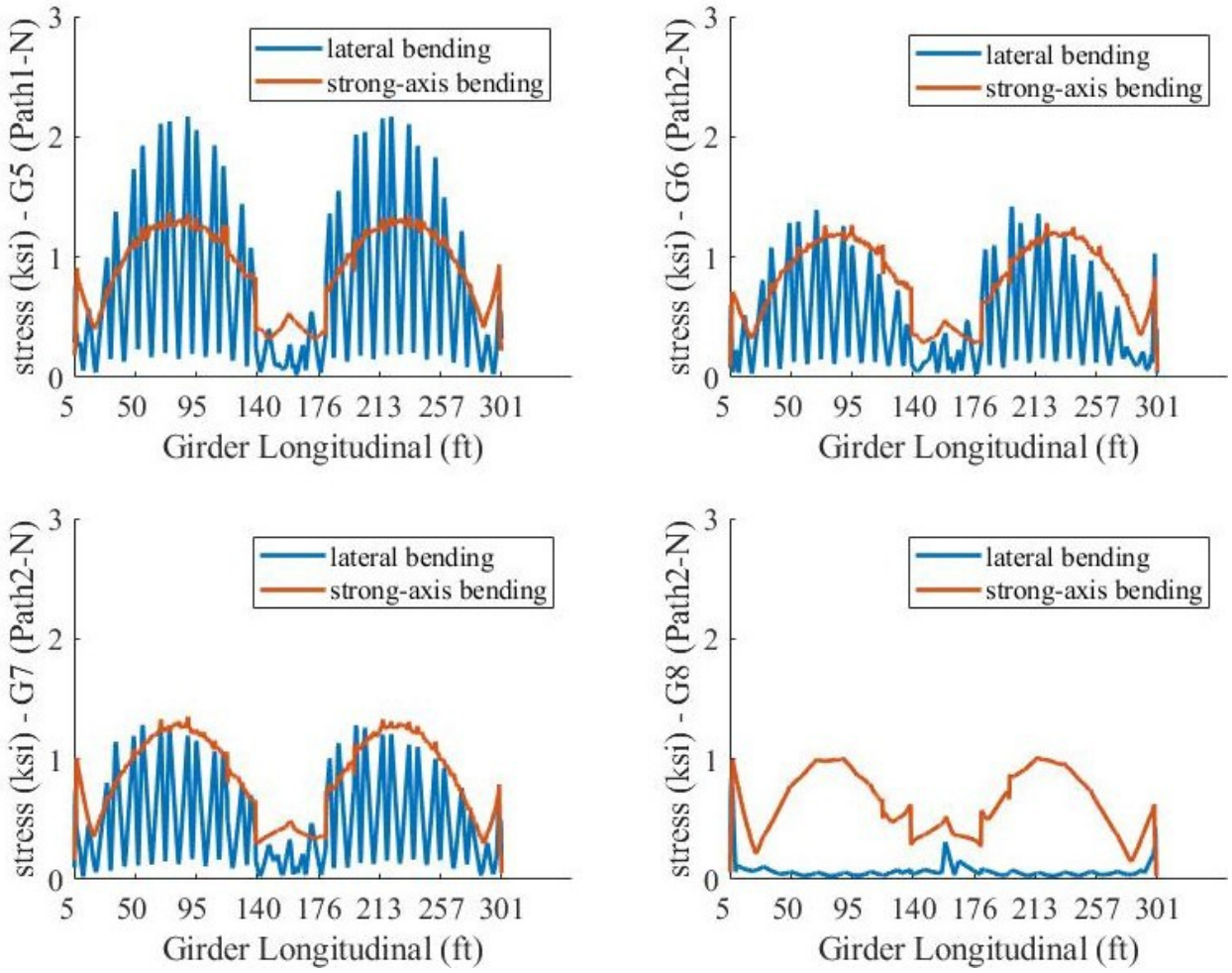

C. Mattis-57

Figure 55. Graph. Bottom flange lateral bending stress and strong-axis bending stress for girders under controlling truck test path.

BRIDGE GLOBAL MOVEMENT

Bridge superstructure displacement and end rotation of critical girders are categorized as global movements, which were small due to isolated truck loading, but they can still be useful to understand live load behavior and confirm satisfactory model performance. Global movement measurements are only available for the full bridges.

Bridge Superstructure Displacement

Relative bridge movement between the superstructure and substructure was measured at all four corners at the bearing level (exterior girder bottom flange) for Mattis-74, parallel and perpendicular to the girder lines. Bridge overall longitudinal movement at the deck level between the approach slab and transition slab was measured for Mattis-57. The largest movement was captured at the obtuse corners of Mattis-74 (per the bridge plan-view shown in Figure 1), the SW corner for the southbound live loads, and NE corner for the northbound loading cases. For Mattis-57, the maximum longitudinal

field displacement measurement was observed at the NW corner, which is also an obtuse corner (as shown in Figure 2), with a magnitude of 0.13 mm (0.005 in.). Overall, the superstructure movement relative to the bridge substructure is small under single-truck live load. Because of the flexibility allowed at the bearing for a stub abutment bridge, the relative movement between the superstructure and substructure is larger than at the deck level based on numerical modeling. For Mattis-74 with a stub abutment, movement along the bridge was larger than in the lateral direction perpendicular to the girder lines at the bearing level; movement at the bearing level is different from that at the deck level in most cases due to girder deformation.

Bridge corner movements were more obvious when the load was closer to exterior girders, especially at the bearing level for Mattis-74 (Path 3-N and Path 1-S). Response histories of movement at a representative corner (northeast) under the critical Path 3-N over Mattis-74 are shown in Figure 56. Slightly smaller superstructure-substructure relative movements were measured in the field than predicted by numerical models, which indicates less flexibility of elastomeric bearings than theoretically expected. Overall, the response history illustrated good comparisons between numerical models and the field test for the superstructure-substructure relative movement at the bearing level for Mattis-74. Because the bridge models did not include explicit representation of the approach slab, the deck-level superstructure movements for Mattis-57 from numerical simulation results at the deck corner were not directly comparable to the field measurements.

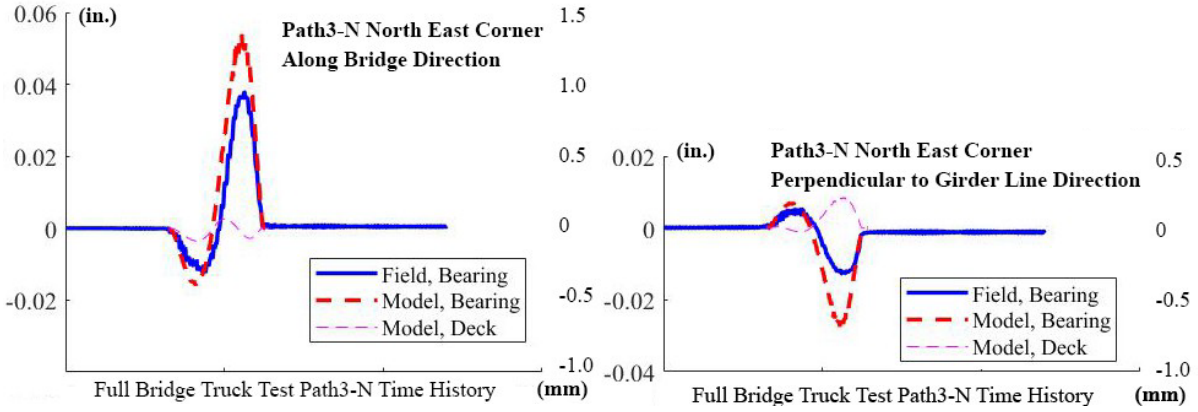

Figure 56. Graph. Northeast corner displacement transducer time history—Mattis-74 Path 3-N.

Girder End Rotation

End rotations about the girder major-axis (Z-axis rotation) were measured in the field by tiltmeters for the most heavily loaded girders, determined considering daily traffic, as indicated in Figures 1 and 2. Data collected from tiltmeters were noisier than measurements from strain gauges and displacement transducers, so low-pass filters (normalized bandwidth of 0.1) were applied to further process the data. Frequency content above 2 Hz was cut for tiltmeter measurements. Figure 57 presents typical response histories for the measured and simulated controlling tests—Path 2-S for Mattis-74 and Path 2-N for Mattis-57—and good comparison was achieved between the 3D FEA and field measurements. As expected, the stub abutment bridge was observed with larger end rotations than the integral abutment bridge. In general, girder end rotations for bridges under the live load truck tests were small.

Because of the noisy nature of the tiltmeter measurements and the small magnitude of both girder end rotations and bridge movements, they were not considered for quantification of bridge dynamic response under live load. The ability of the models to simulate such small bridge responses, however, did give further confidence in the accuracy of the numerical simulation approaches, especially regarding the representation of boundary conditions. Based on the verification with field data, the numerical simulation strategies used in this study can be adopted for research studying similar types of bridges and load conditions.

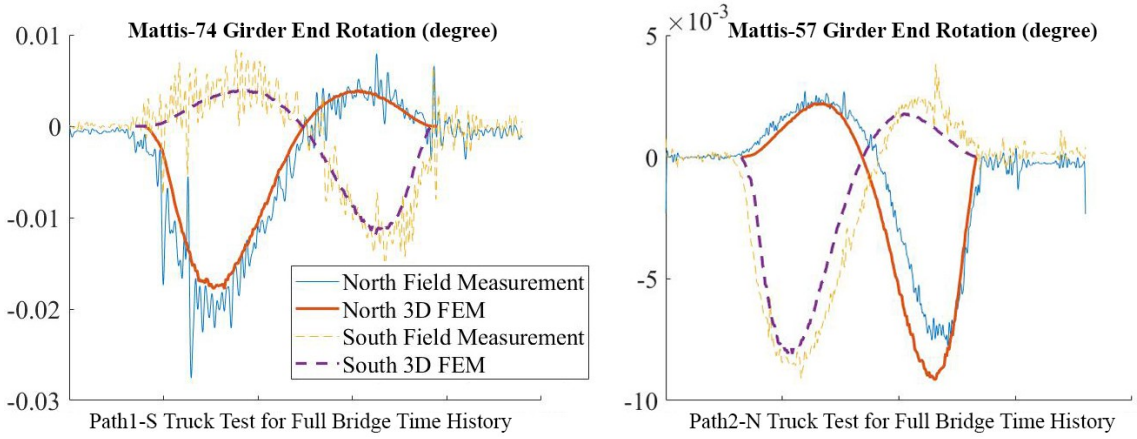

Figure 57. Graph. Girder end rotation of measured and simulated test Path 2-S on Mattis-74 (left) and Path 2-N on Mattis-57 (right).

Dynamic Impact on Superstructure Live Load Response

Measurements (at 20 Hz) from strain gauge readings collected during the full-bridge truck tests at various loading speeds were used to evaluate the dynamic impact on bridge response. The dynamic load allowance (DLA) is otherwise called the dynamic impact factor (IM). IM was evaluated based on field data according to the equation in Figure 58, where ε_{dyn} and ε_{sta} are maximum dynamic and static strain measurements, respectively, at an instrumented strain gauge location under a certain truck test path. The IM under full speed tests at 56 kph (35 mph) and lower speed tests at 32 kph (20 mph) were calculated, considering the crawl speed tests (at 3.2 kph [2 mph]) as static live load. Most IMs calculated from field measurements are less than 0.2, and Table 7 records the gauge locations where an IM factor larger than 0.1 were observed.

$$IM = \frac{max(\mathcal{E}_{dyn}) - max(\mathcal{E}_{sta})}{max(\mathcal{E}_{sta})}$$

Figure 58. Equation. Calculation of dynamic impact factor.

All instrumented locations with measured IM larger than 0.2 were near bridge supports. For the stub abutment bridge (Mattis-74), the dynamic impact factor evaluated from tests under both speeds was within the AASHTO required 33% used in design for general load cases (excluding fatigue). On the other hand, for the integral abutment bridge (Mattis-57), strain measurements at a few locations along exterior girder G8 exceeded the IM limit, especially when the bridge was tested at a normal traffic speed of 56 kph (35 mph). These test results indicate that exterior girders of an integral

abutment bridge, especially near the obtuse corner (pier and northeast corner of Mattis-57) are subjected to more significant amplification of girder and cross-frame response from dynamic live load. Such an amplification is not considered in standard design procedures but could be significant, especially when exterior girders are heavily loaded, such as during staged construction or bridge widening and retrofit.

Table 7. Critical Dynamic Impact Factors Calculated from Field Measurements

Bridge Mattis-74 Dynamic Impact Factor			Bridge Mattis-57 Dynamic Impact Factor		
Gauge Location	**20 mph**	**35 mph**	**Gauge Location**	**20 mph**	**35 mph**
G1-Pier-TE	0.11	0.23	G6-Pier-S-WE	0.04	0.22
G1-Pier-BEb	0.11	0.26	G6-Pier-S-WW	0.04	0.23
G3-Pier-BWb	0.16	0.21	G8-Pier-TE	0.08	0.25
G4-Pier-TW	0.09	0.23	G8-Pier-TW	0.05	0.26
G5-Pier-TE	0.09	0.27	G8-Pier-BEb	0.14	0.59
G5-Pier-TW	0.09	0.26	G8-Pier-BWb	0.17	0.69
CF8-3&4-Bc	0.06	0.32	G7-SAbut-TE	0.00	0.25
CF14-1&2-Bc	0.13	0.21	G8-NAbut-TE	0.19	0.25
CF14-1&2-E	0.25	0.17	G8-NAbut-TW	0.10	0.23
–	–	–	G8-NAbut-BEb	0.19	0.36
–	–	–	G8-NAbut-BWb	0.20	0.36
–	–	–	CF17-7&8-Bc	0.37	0.75
–	–	–	CF17-7&8-E	0.29	0.54

CHAPTER 5: BRIDGE RESPONSE UNDER LIVE LOAD—NUMERICAL SIMULATION

To enhance understanding of the magnitude and distribution of I-girder response under live load and the effect of bridge geometric parameters on their behavior, numerical parametric studies were conducted. For compatibility with the field tests and for clarity in observing load distribution trends, an isolated truck loading scenario was considered for this parametric study. Standard procedures for designing skewed steel I-girder bridges were evaluated by analyzing the behavior of bridges with variations in skew and bridge width under isolated truck loads over multiple live load paths along the width of a bridge. This scenario does not represent the complete set of live loads typically accounted for in design (i.e., lane loads plus design trucks), as the findings are focused on understanding general bridge response and making comparisons for a particular loading condition.

This chapter first describes the background of the parametric studies, including design considerations for a skewed steel I-girder bridge under an isolated truck load using standard 1D line girder analysis (LGA), as well as the bridges and live load paths simulated for the parametric study. Then, girder response in bridge spans is evaluated for both stub abutment and integral abutment bridges, regarding strong-axis bending and lateral bending. Variation of girder response with respect to variations in skew and bridge width are presented, and comparisons between findings from the numerical parametric studies and the standard LGA are discussed. Girder response near the bridge pier was generally less significant than that along bridge spans under isolated truck live loads, so the pier region responses are only discussed briefly at the end of this chapter.

NUMERICAL STUDY BACKGROUND

Loading Conditions

Vehicular live loading can include a design truck (such as design truck considered in this research, named HS20 in previous versions of AASHTO specifications, now part of the HL-93 live load model per AASHTO [2024] Article 3.6.1.2.2), or a design tandem, as well as design lane loads, with multiple design trucks over a design lane being accounted for when determining critical negative bending for continuous bridges. To focus this study on the load distribution of skewed steel I-girder bridges—without considering multiple lanes, lane loading, or a design tandem—design trucks were considered in one lane at a time. Other design factors (such as the multiple presence factor) were therefore not considered. Single trucks, as well as two trucks in a lane spaced 15 m (50 ft) apart, were modeled. The AASHTO design truck has a front axle of 35 kN (8 kips) and middle and rear axles of 142 kN (32 kips). Spacing between the front and middle axles is 4.3 m (14 ft), while spacing between the two 142 kN (32 kips) axles can vary from 4.3–9.1 m (14–30 ft). A sensitivity study showed that smaller rear-axle spacing induces more critical girder response in the positive moment regions, so the minimum rear-axle spacing of 4.3 m (14 ft) was used for the single-truck case as well as the two-truck case (truck train) per AASHTO (2024) Article 3.6.1.3.1.

The set of parametric study bridges included variations of the Mattis bridges for 4, 6, 8, and 12 girders, as presented in Figure 59, for a total of 8 sets of bridges. Each set was modeled with skew

variations of 0° to 70°, as shown in Figures 4 and 5. Figure 59 shows simulated load paths for the parametric study bridges of different widths, where the arrows represent the truck centerline. The slightly different girder spacing and overhang width for bridges with stub and integral abutments, based on Mattis-74 and Mattis-57, are listed in the figure. Edge load paths close to exterior girders were simulated as theoretical cases, which could potentially occur during staged construction (such as in the Mattis Avenue bridges), bridge widening, or retrofit. Inner load paths further away from exterior girders were arranged based on design traffic lanes on the full and half (i.e., during staged construction) Mattis Avenue bridges.

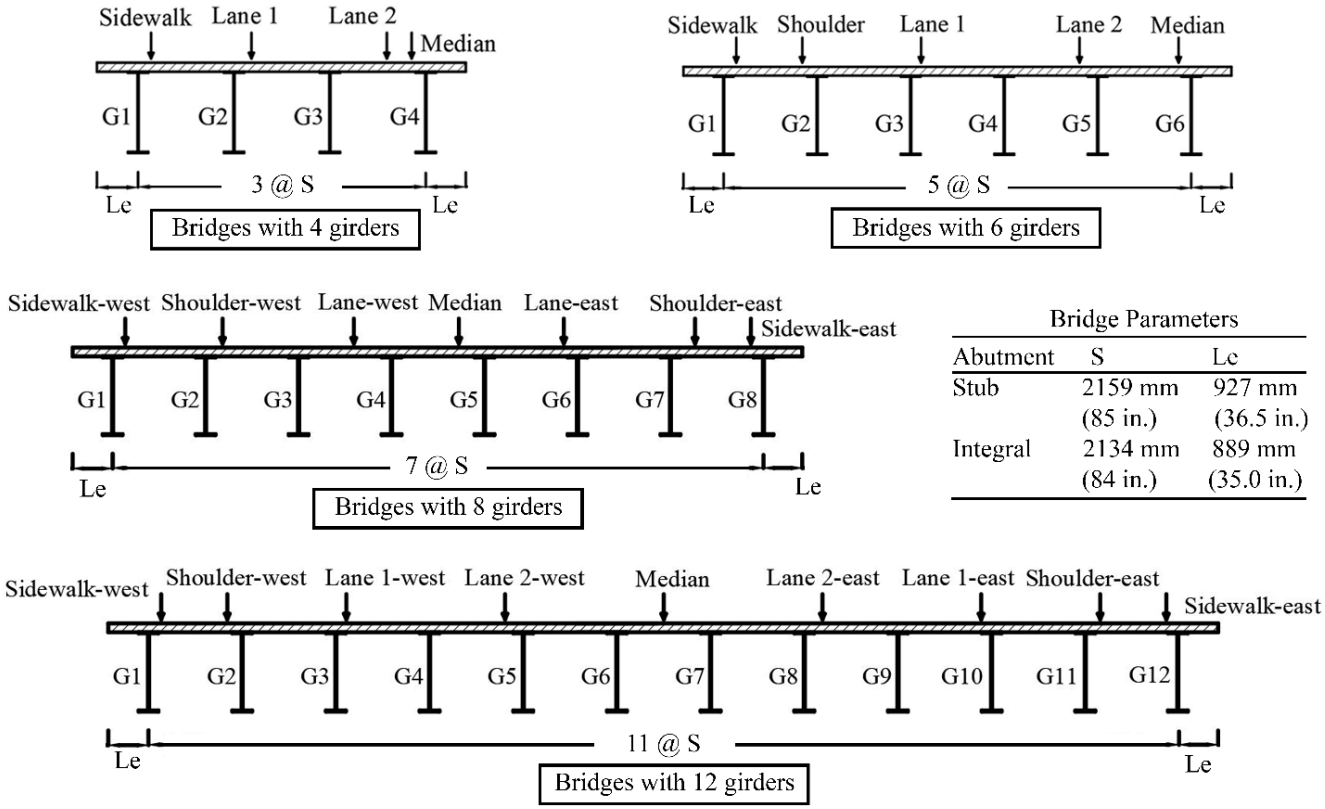

Figure 59. Section view. Load paths for numerical parametric studies of stub abutment and integral abutment bridges.

Baseline Line Girder Analysis

1D LGA, which is a common simplified analysis method used in bridge proportioning, can provide a baseline comparison for the 3D finite element analysis. LGA calculations for the Mattis Avenue bridges and their parametric variations were conducted considering the design truck load in a single lane for two scenarios: (i) an isolated design truck, and (ii) 90% of the two design truck train (for negative bending moment). Stub and integral abutment bridge boundary conditions were both modeled as roller supports at the bridge ends and with a pin support for the continuous girder at the middle pier, which is considered conservative for IABs. Wheel loads of the design truck(s) were applied to a single girder as moving point loads. Flexural response envelope values (magnitude of peak moment and stress) obtained considering both truck scenarios are shown in Table 8, prior to considering distribution effects.

Table 8. Girder Strong-Axis Bending Demands for Mattis Avenue Bridges Using Line Girder Analysis

Bridge Name	Demands	South Midspan	North Midspan	Pier
Mattis-74	Moment	2409 kN-m (1777 k-ft)	2763 kN-m (2038 k-ft)	3449 kN-m (2544 k-ft)
	Stress	69 MPa (10.0 ksi)	74 MPa (10.7 ksi)	67 MPa (9.6 ksi)
Mattis-57	Moment	2992 kN-m (2207 k-ft)	2956 kN-m (2180 k-ft)	3430 kN-m (2530 k-ft)
	Stress	74 MPa (10.8 ksi)	74 MPa (10.7 ksi)	54 MPa (7.8 ksi)

The peak strong-axis bending stresses shown in Table 8 were then adjusted according to live load distribution factors (LLDFs), based on standard design requirements (AASHTO 2024). When considering truck loads in a single lane, empirical equations associated with bridge span length, girder spacing, and skew angle are used to calculate the LLDF for interior girders (which considers the multiple presence factor), and a lever rule is used for exterior girders. Bridge width is not considered in either estimation approach. On the other hand, bridge width is a critical factor of more conservative estimation for exterior girder LLDF, which analyzes a bridge as a rigid cross-section considering cross-frame load transfer, per AASHTO (2024) C4.6.2.2.2d-1. Figure 60 presents the LLDFs (for single-lane design truck loads) of the parametric study stub abutment bridges (based on Mattis-74) and IABs (based on Mattis-57) with respect to variation of skew, which are different from what would have been used when designing the bridges if two or more lane-loaded scenarios govern. The multiple presence factor of 1.2 is considered for the lever rule and the rigid cross-section analysis. Skew effect is considered for bridges skewed more than 30° in the LLDF calculation, and the LLDF equations take all skews larger than 60° as being equal to 60°. Bridges skewed more than 60° are suggested by AASHTO to be designed with a refined method of analysis.

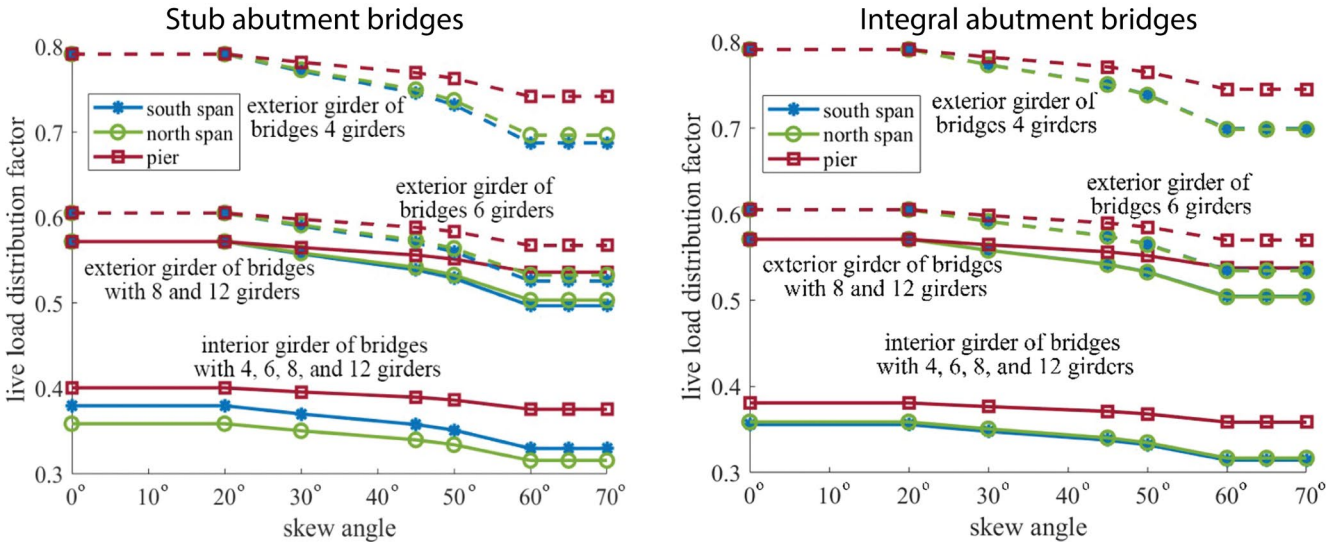

Figure 60. Graph. Live load distribution factors for isolated truck loading of the parametric study bridges.

Based on a prior agency survey presented in Volume I (Zhou et al., 2026), it is standard practice for most state transportation agencies to use the governing LLDF from exterior or interior girders for design, and many states mentioned that the lever rule often governs exterior girder design. LLDF for the parametric study bridges, as presented in Figure 5, indicates that the lever rule governs for

exterior girders of wider bridges (with 8 or 12 girders), while the rigid cross-section analysis governs for exterior girders of narrower bridges (with 4 or 6 girders). In LGA, girder lateral bending response is considered based on the AASHTO (2024) recommended total additional (unfactored) flange lateral bending stress of 69 MPa (10 ksi) for interior girders and 14 MPa (2 ksi) away from the end supports for exterior girders when bridges have skew exceeding 20° and cross-frames are in a staggered layout (AASHTO 2024). In addition, although AASHTO (2024) C6.10.1 is somewhat ambiguous, the proper interpretation seems to be that the recommended flange lateral bending stress estimate in exterior girders with staggered cross-frames near skewed bridge supports is 7.5 ksi.

GIRDER STRONG-AXIS BENDING STRESS IN BRIDGE SPAN

Strong-axis bending stress was numerically evaluated for each set of stub abutment bridges and IABs under the two different design truck live-load scenarios. Effects of bridge skew, width, and type of abutments on the distribution and magnitude of girder strong-axis bending stress were studied. Strong-axis bending stress in the bottom flange is more critical than that in the top flange for the in-service bridges with composite deck-girder behavior, and strong-axis bending response trends are similar for top and bottom flanges due to the linear assumption of strong-axis bending curvature along the girder height (even for composite sections). Bottom flange strong-axis bending stress (calculated at the bottom surface of the bottom flange) is therefore discussed.

Strong-Axis Bending Stress Distribution

Stub abutment bridges (based on Mattis-74) that have six girders, with skew variation from 0° to 70°, are selected to illustrate the distribution of girder strong-axis bending stress. Figures 61 and 62 present strong-axis bending stress envelopes of each girder for the six-girder stub abutment bridges skewed at 0° and 60°, considering the truck load(s) over Lane 1 and the Sidewalk (as shown in Figure 60), respectively. Peak strong-axis bending stress out along the bridge spans was extracted for all girders, at locations indicated with the dashed lines and the solid symbols (indicating south span or north span and 0° or 60° skew). (Girder response in the negative bending region near the interior support is discussed later.) The maximum in-span stress of each girder for the eight bridges is then summarized in the left-side figures, where the dashed boxes and solid symbols represent stresses corresponding to those from the right-side figures.

Greater strong-axis bending stress was observed at girders closest to the live load path—G3 for Lane 1 and G1 for the Sidewalk. For Lane 1, with live load near mid-width of the bridge and not close to any exterior girder, strong-axis bending response was mainly evenly distributed among the three girders near the load path. For the Sidewalk, with live load near exterior girder G1, strong-axis bending response was mostly distributed to the exterior girder. Overall peak strong-axis bending stress was larger when live load was closer to exterior girders, from comparing results for the Sidewalk (Figure 62) versus Lane 1 (Figure 61) truck loading. When directly loaded, exterior girders were subjected to larger strong-axis bending stress than interior girders, due to fewer adjacent girders for load distribution.

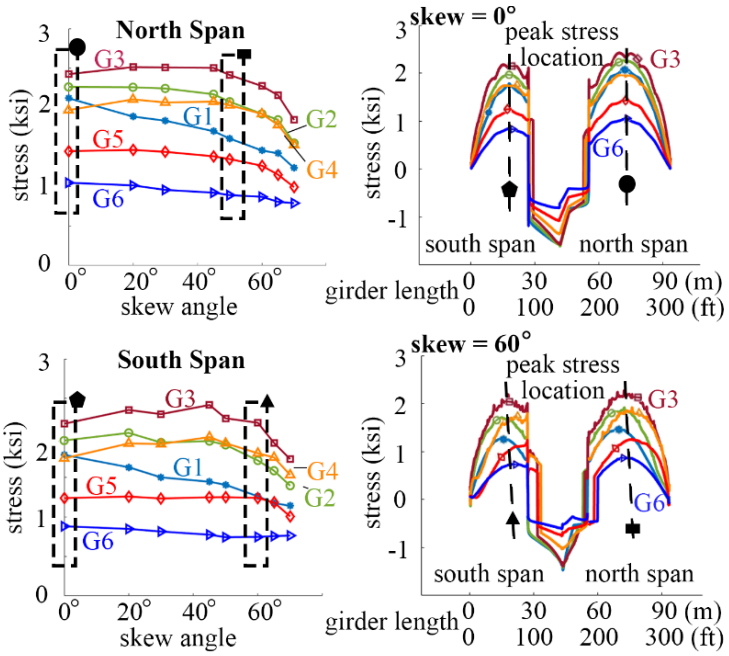

Figure 61. Graph. Typical stress envelopes and peak strong-axis bending stress for stub abutment bridges with six girders for Lane 1 load path (1 ksi = 6.9 MPa).

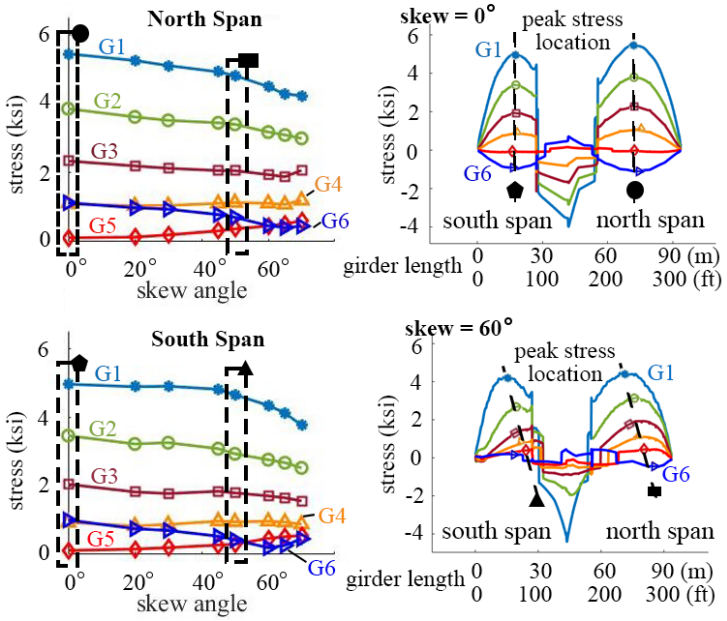

Figure 62. Graph. Typical stress envelopes and peak strong-axis bending stress for stub abutment bridges with six girders for Sidewalk load path (1 ksi = 6.9 MPa).

At 0° skew, the peak strong-axis bending stress was near midspan of the girders, as shown in Figures 61 and 62. As skew increased, the critical strong-axis bending response locations along the bridge spans shifted from the general trend of being near midspan (based on LGA) to an obtuse corner-to-corner distribution. For exterior girders, the critical location of in-span strong-axis bending stress got closer to the bridge obtuse corners when skew increased, whereas the critical location got closer to

the unloaded obtuse corner with increasing skew for interior girders. In the south span, the peak stress formed a distribution from near the bridge's southwest corner to near the southeast side of the pier. In the north span, the peak stress was distributed from near the northwest side of the pier to close to the northeast corner of the bridge. In addition, such an obtuse corner-to-corner stress distribution was more obvious for the Sidewalk load path (an edge load path near exterior girders, as shown in Figure 62) than the Lane 1 load path (an inner load path further away from exterior girders, as shown in Figure 61).

Observations for the IABs (not explicitly shown) are similar to those for the stub abutment bridges based on the numerical parametric studies, with only the following notable differences. Almost no girder strong-axis bending stress was observed at bridge ends for stub abutment bridges, because of the flexible end restraints, whereas considerable girder strong-axis bending stress was observed at the ends of IABs. For a few cases when IABs were skewed over 60° (even though not commonly used), the strong-axis bending stress at bridge ends from negative bending (observed at obtuse corners) was larger than that along the spans due to positive bending, which is not considered in the standard LGA approach that uses simplified pin-roller boundary conditions for IABs.

Peak Strong-Axis Bending Stress

The maximum strong-axis bending stresses in Figure 61 (for one of the inner load paths) and Figure 62 (for one of the edge load paths) are recorded in Figure 63 with the other load paths. The peak in-span strong-axis bending stress considering all inner and edge load paths for all stub abutment bridges in the parametric study is also presented in Figure 63. The figure shows peak stress in the longer (north) span versus variation in bridge width and skew; comparison of the peak stress versus LGA calculations is also illustrated. For exterior girders, only LGA results based on LLDF using the lever rule are presented in the figure, while the more conservative rigid cross-section analysis results are simply discussed (without illustration) for clarity. Girder response under practical/inner load paths and hypothetical/edge load paths adjacent to exterior girders are presented separately.

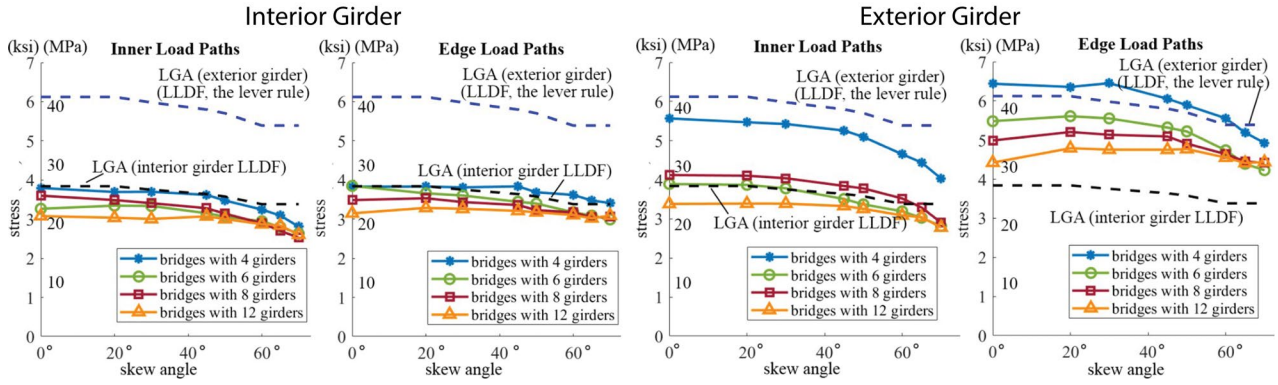

Figure 63. Graph. Peak strong-axis bending stress in all parametric study stub abutment bridges.

When using LLDFs from interior and exterior girders to estimate their respective strong-axis bending stress values, the LGA estimation was generally conservative. For interior girders, as shown in Figure 63 (left), numerical simulation results were slightly larger than the LGA calculations only when bridges with four girders were loaded over the sidewalk region (edge load paths). This is also the only case

where rigid cross-section analysis is needed, while the lever rule is conservative for the exterior girders in all other cases, as shown in Figure 63 (right). Exterior girders were observed with peak strong-axis bending stress larger than from an LGA calculation using the interior girder LLDF. It is therefore necessary to use the lever rule (and even rigid cross-section analysis for very narrow bridges having less than four girders) when estimating the exterior girder LLDF in cases where live load close to exterior girders is possible.

On the other hand, when using a governing LLDF from interior and exterior girders to estimate strong-axis bending stress demands for all girders, interior girders would be more conservatively designed using LGA than exterior girders. As shown in Figure 63, if the governing LLDF (usually for exterior girders, using the lever rule) was used for all girders on the stub abutment bridges, then the interior girder strong-axis bending stress would typically be conservatively overestimated by almost 50% (for isolated truck loads). Consideration of rigid cross-section analysis would yield even more conservative results.

For inner load paths, greater strong-axis bending stress was observed on exterior girders of stub abutment bridges with four girders compared to wider bridges, because one of the inner load paths—Lane 2 (as shown in Figure 59)—was close to exterior girder G4. Except for that bridge, width only had a small effect on girder strong-axis bending stress for inner load paths. The edge load paths were at the same relative locations on all the bridges—1.2 m (48 in.) away from bridge outer edges, as shown in Figure 59. Girder response under edge load paths was therefore suitable to evaluate the effect of bridge width on strong-axis bending response. For the edge load paths, exterior girders on narrower stub abutment bridges had larger strong-axis bending stress, especially when skew was less than 45°. On the other hand, interior girders had similar strong-axis bending stress regardless of bridge width. Overall peak girder strong-axis bending response decreased with increasing skew, with the rate of decrease larger for narrower stub abutment bridges and for exterior (versus interior) girders. LGA calculations considering the skew effect for girder strong-axis bending stress based on AASHTO (2024) do not take into account bridge width, which is conservative (especially for narrow stub abutment bridges and exterior girders).

Figure 64 shows the peak strong-axis bending stress considering all inner and edge load paths for all IABs in the parametric study, with both exterior and interior girders presented. The figure records the peak strong-axis bending stress for the longer span (the south span) of the IABs. The peak stress of the IABs was about 20% less than that of the stub abutment bridges, because of more bridge end restraint in the IABs. The commonly used LGA assumes the same boundary conditions when estimating the response of IABs and stub abutment bridges, which is more conservative for IABs than stub abutment bridges. As with the stub abutment bridges, LGA using an interior girder LLDF is sufficient for all IAB girders, except when live load is placed near exterior girders. Estimating girder strong-axis bending stress with a controlling LLDF from the lever rule is safe for exterior girders, and even more conservative for interior girders. Using rigid cross-section analysis would yield even more conservative results, which is not shown in Figure 64 for clarity. For all IAB load paths, the maximum strong-axis bending stress on interior girders is consistently less than 50% of the LGA calculation value based on an LLDF for exterior girders, even when only using the lever rule, as shown in Figure 64 (left).

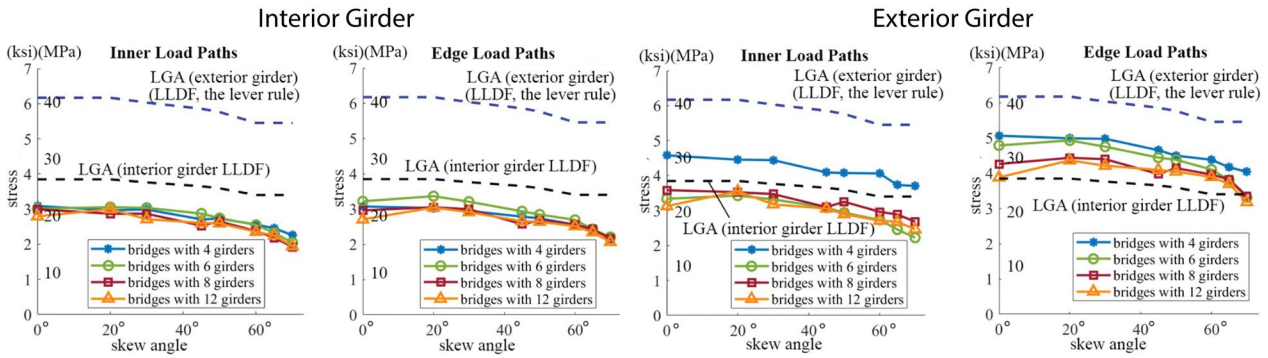

Figure 64. Graph. Peak strong-axis bending stress in all parametric study integral abutment bridges.

Like in the stub abutment bridges, the peak strong-axis bending stress in IABs for inner load paths is mostly not affected by bridge width, except for IABs with four girders that have an exterior girder close to an inner load path during staged construction (based on Mattis-57). For edge load paths, slightly larger strong-axis bending stress was observed on exterior than interior girders, and on narrower versus wider IABs. However, the effect of bridge width is much smaller than that observed for stub abutment bridges. As was the case for stub abutment bridges, the peak strong-axis bending stress for IABs decreased with an increase in skew, with a rate of decrease mostly consistent among the bridges of various numbers of girders. Unlike in the stub abutment bridges, the rate of stress change with change in skew was not noted to be different for exterior versus interior IAB girders.

GIRDER LATERAL BENDING STRESS IN BRIDGE SPAN

Girder top flanges are restrained by the concrete deck for in-service composite bridges, with less lateral bending response than at the bottom flanges. Lateral bending stress at the bottom flange of the I-girders was therefore evaluated on the stub abutment bridges and IABs for the simulated isolated design truck live load to study the effect of skew, bridge width, and type of bridge abutment on the magnitude and distribution of flange lateral bending stress out along the bridge spans in parametric variations of the monitored bridges.

Flange Lateral Bending Stress Distribution

Critical girder lateral bending response was consistently observed at cross-frame locations. Non-skew stub abutment bridges were not observed with any notable lateral bending response; on the other hand, non-skewed IABs exhibited notable bottom flange lateral bending stress of up to 14 MPa (2 ksi) at bridge ends.

Flange lateral bending stress was generally more significant for interior girders than exterior girders. Peak lateral bending stress was only slightly affected by the location of the load path, which is different from strong-axis bending stress, where a much larger peak response was induced by live load closer to exterior girders. However, the distribution of girder lateral bending response for skewed bridges was affected by the location of the load path. Near critical girder ends, the peak stress increased with increasing skew. For load paths closer to edges than mid-width of a bridge, the distribution of lateral response to interior girders was more obviously governed by increasing stress near bridge obtuse corners with an increase in skew, and the response was more like that for a

Sidewalk load path than for the Median load path. For many skewed bridges subjected to either load path, the peak lateral bending stress was observed at different locations compared to the peak strong-axis bending stress.

Peak Bottom Flange Lateral Bending Stress

Maximum in-span bottom flange lateral bending stresses are recorded for all load paths analyzed for stub abutment bridges with eight girders to form one of the datasets in Figure 65. The figure shows the peak in-span bottom flange lateral bending stress considering all inner and edge load paths for all stub abutment bridges in the parametric study (with peak stress for exterior versus interior girders and in north versus south spans reported separately). Interior girders (presented in Figure 65-A) generally experienced larger flange lateral bending stress than exterior girders (presented in Figure 65-B). Exterior girders were only observed with considerable lateral bending response for narrow stub abutment bridges with four girders. Notable in-span lateral bending stress was seen on one exterior girder at the first cross-frame near bridge obtuse corners when the live load was placed close to the other exterior girder, especially at the north bridge end where the distance between the first intermediate cross-frame and the bridge end was not controlled. Stress on these exterior girders increased with an increase in skew, especially for skews greater than 45°. Peak stress exceeded 21 MPa (3 ksi) for bridges with skew over 65° but was still smaller than that on interior girders.

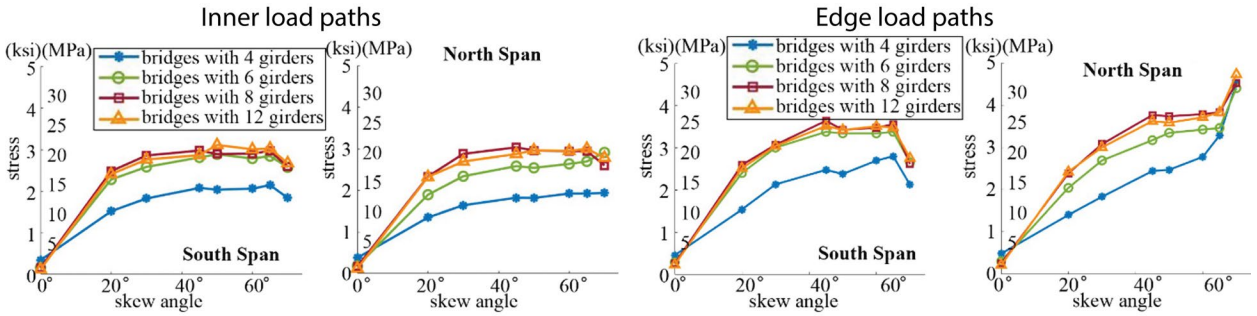

A. Interior girders

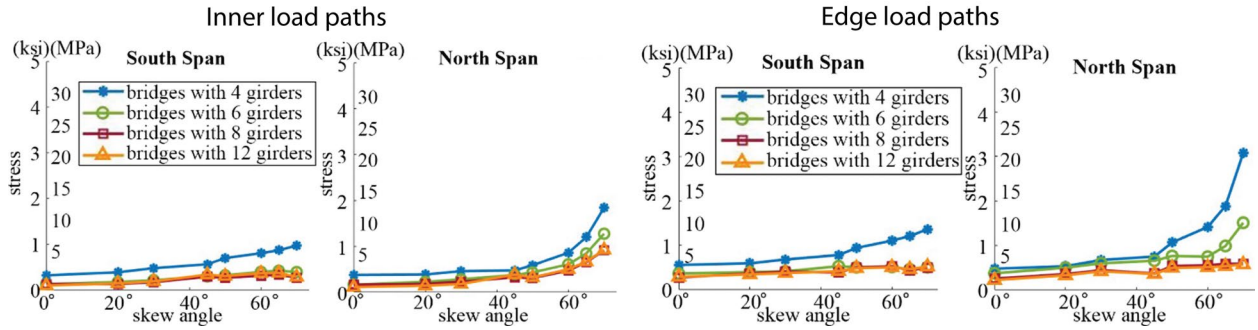

B. Exterior girders

Figure 65. Graph. Peak bottom flange lateral bending stress in all parametric study stub abutment bridges.

For inner load paths, the interior-girder peak bottom flange lateral bending stress (in-span) for skewed stub abutment bridges was mostly not affected by skew, with a peak stress of about 21 Mpa

(3 ksi) for all skewed bridges when considering the design truck in a single lane and without considering design load and multiple presence factors. For edge load paths, the peak lateral stress on interior girders increased from about 21 MPa (3 ksi) at 20° skew to about 28 MPa (4 ksi) at 60° skew, and a peak stress of around 34 MPa (5 ksi) was observed at 70° skew. This increase in peak stress with increasing skew, especially for skew over 60°, indicates the effect of distance from the first intermediate cross-frame to the bridge end on bottom flange lateral bending stress. Respecting the AASHTO (2024) C6.7.4.2 restriction is crucial to avoiding a large lateral bending response at bridge ends.

Figure 66 presents the peak exterior and interior girder bottom flange lateral bending stress in the north and south spans (and near end supports) for IABs in the parametric study. Narrow IABs with four girders were subjected to more lateral bending response at bridge ends than stub abutment bridges with four girders, because of the continuity between girders and abutments in IABs that likely induced global rotation. Lateral bending stress on exterior girders in IABs with four girders was even slightly larger than that on interior girders for skews of 20°–60°, with a peak lateral bending stress of about 21 MPa (3 ksi) observed at bridge obtuse corners. Apart from this case, no considerable flange lateral bending stress was observed on exterior girders; lateral bending response is generally more significant on interior girders.

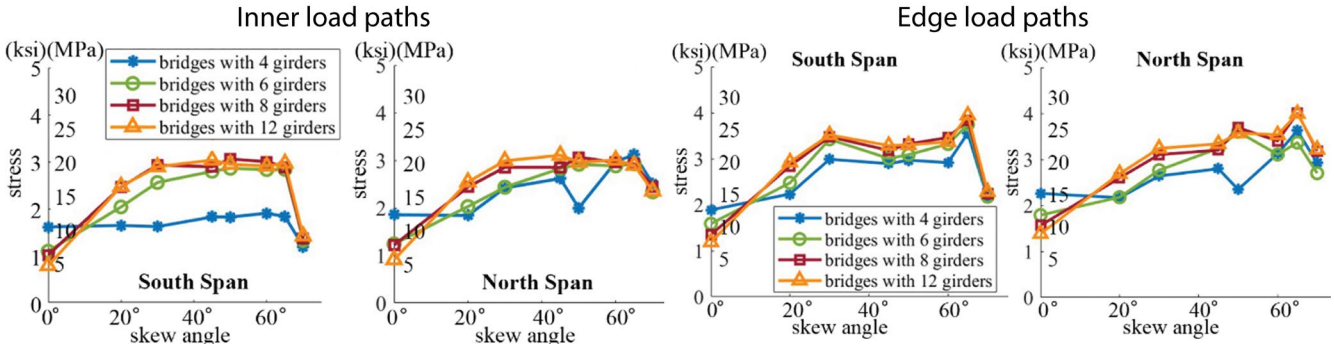

A. Interior girders

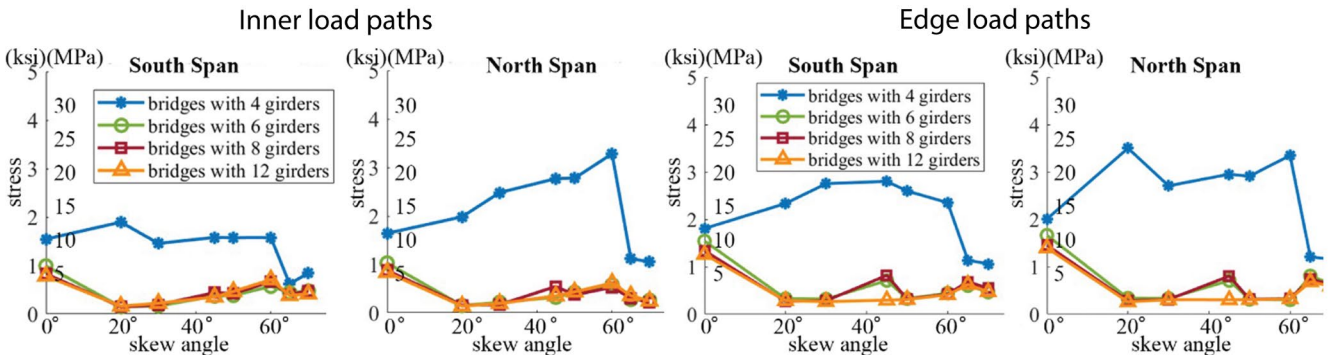

B. Exterior girders

Figure 66. Graph. Peak bottom flange lateral bending stress in all parametric study integral abutment bridges.

A notable decrease of interior girder bottom flange lateral bending stress for the south span of the IABs was observed for skews of 65° and 70°, demonstrating the effect of a decrease in cross-frame spacing (as presented in Figure 5). On the other hand, stub and integral abutment bridges with constant cross-frame spacing were observed to have their peak lateral bending stress mostly not affected by skew for inner load paths. It is therefore concluded that flange lateral bending response is controlled by cross-frame spacing when live load is not directly over exterior girders and bridge corners. In such cases, bottom flange lateral bending stress is induced by differential displacement between girders on skewed bridges that causes cross-frame forces, resulting in peak stress largely affected by cross-frame spacing (in any bay between two adjacent girders) but only slightly affected by skew. Girder lateral bending response on bridges wider than six girders was mostly not affected by bridge width, and bridges with stub and integral abutments that are wider than six girders were observed with similar peak bottom flange lateral bending stress. For the single-lane design truck cases analyzed, as shown in Figure 66, interior girder flange lateral bending stress was less than 28 MPa (4 ksi) for the IABs. This stress level is smaller than the additional stress of 69 MPa (10 ksi) suggested by AASHTO (2024) to account for lateral bending in interior girders of skewed bridges, but the AASHTO limit is intended to be compared to all unfactored loads combined, whereas this analysis only considers live load.

GIRDER RESPONSE NEAR BRIDGE INTERIOR SUPPORT

Considerable live load response near the bridge interior support in the current numerical parametric study (evaluating a single lane loaded by design truck(s) for in-service bridges) was observed by applying two design trucks spaced 15 m (50 ft) apart, with 10% response reduction considered, per AASHTO (2024). Maximum strong-axis and flange lateral bending stress values for the stub abutment bridges near the pier for interior and exterior girders (considering inner and edge load paths) are presented in Figure 67 with respect to skew and bridge width. Strong-axis bending stress on the girder bottom flange near the pier, induced by negative bending, was only slightly smaller than that along the spans caused by positive bending (comparing Figure 67 to Figure 63). Peak stress on interior girders near the pier decreased slightly with increasing skew for both inner and edge load paths, while peak stress on exterior girders near the pier (induced by the edge load paths) increased slightly with increasing skew. Skew generally has little effect on strong-axis bending stress of stub abutment bridges near the pier. Flange lateral bending response for interior girders of stub abutment bridges was less significant near the pier than along the spans for bridges with skew less than 60°, comparing Figure 67 to Figure 65. Exterior girder flange lateral bending stress was more significant near bridge interior supports than along the span for stub abutment bridges.

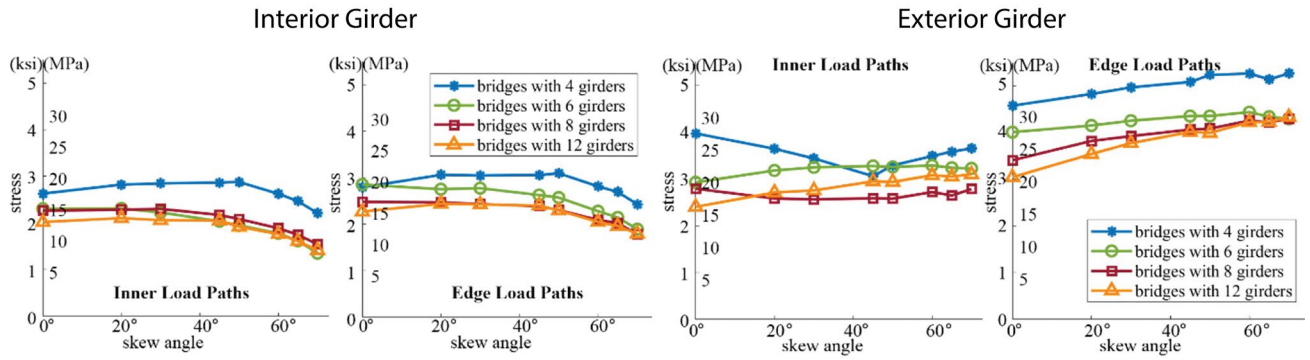

A. Strong-axis bending stress

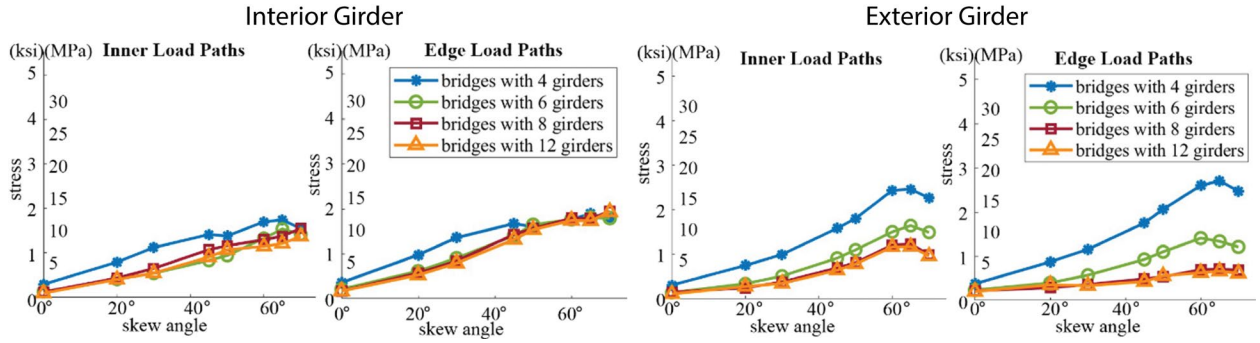

B. Bottom flange lateral bending stress

Figure 67. Graph. Peak girder response near the bridge pier in all parametric study stub abutment bridges.

The maximum bottom flange strong-axis and lateral bending stresses of IABs near the pier are presented in Figure 68. Like in stub abutment bridges, the strong-axis bending response near the pier (induced by negative bending) is smaller than that along the spans (from positive bending) for IABs. As skew increases, the peak stress for interior girders slightly decreases, while the peak stress for exterior girders slightly increases. Peak stress for IABs was smaller compared to stub abutment bridges, which is like the findings regarding stress along the spans. Strong-axis bending stress was in general not affected by bridge width near the pier for stub abutment bridges (as shown in Figure 67) and for IABs (as presented in Figure 68), except for narrow bridges with just four girders, which had slightly larger peak stress than in wider bridges.

For IABs (as for stub abutment bridges), interior girder flange lateral bending stress was more significant along the spans and near the abutments (as shown in Figure 66) than near the pier (as presented in Figure 68), while exterior girders had larger flange lateral bending stress near the pier than in-span. Similar to the discussion for girder response along the spans, exterior girders for narrow bridges (with either stub or integral abutments) were subject to larger lateral bending response than wider bridges. For all wider bridges, exterior and interior girders were observed with similar peak lateral bending response near the pier, with no considerable effect due to bridge width. Near the pier (which has fixed bearings), the lateral bending response was induced by global movement—rotation about the skewed support line. Peak lateral bending stress therefore almost monotonically increased with increasing skew.

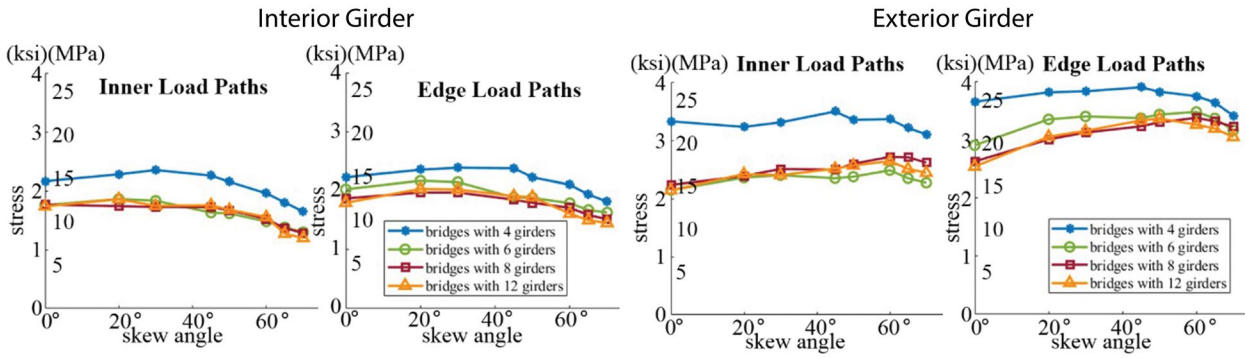

A. Strong-axis bending stress

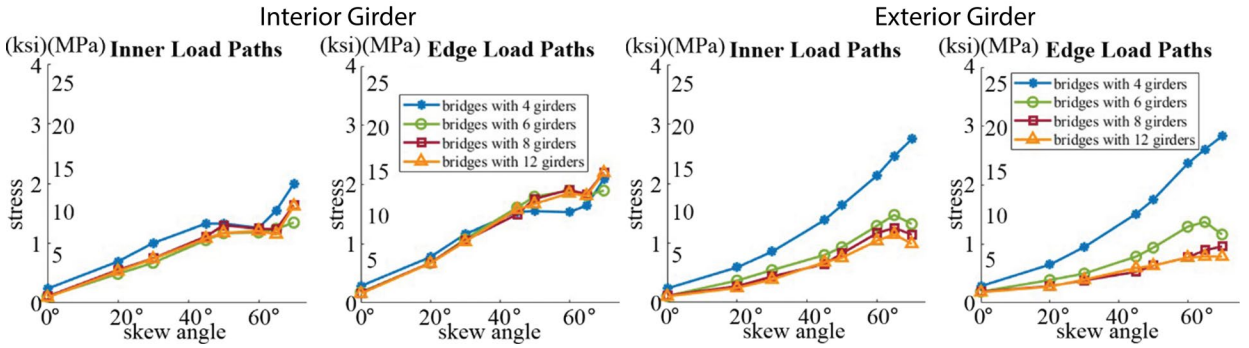

B. Bottom flange lateral bending stress

Figure 68. Graph. Peak girder response near the bridge pier in all parametric study integral abutment bridges.

CHAPTER 6: SUMMARY, CONCLUSIONS, AND RECOMMENDATIONS

This volume documents research aiming to enhance knowledge about the structural demand and load distribution of skewed steel I-girder bridges with stub abutments or integral abutments when subjected to construction loading and in-service live load. These objectives have been addressed in this research through combined analysis of measurements from field monitoring and data from numerical simulation results. Two new two-span continuous steel I-girder bridges in Champaign, Illinois, were selected for field monitoring, following experiences from previous research and findings from an agency survey. Mattis-74 has stub abutments and a 41° skew, while Mattis-57 has integral abutments and a 45° skew. This chapter summarizes the key findings and provides the primary practical applications of this research regarding evaluation of standard design practice regarding pre-composite and in-service skewed steel I-girder bridges.

SUMMARY AND CONCLUSIONS

Skewed I-Girder Bridge Behavior during Deck Placement

Two skewed steel I-girder bridges were monitored in the field during concrete deck placement of Stage I construction (approximately half of the bridge), with data analysis focused on I-girder response. 3D finite element analysis (FEA) was also conducted for the monitored deck placement process, where boundary conditions (at bearings and the pre-composite integral abutment), wooden formwork (to transfer wet concrete dead load), and deck overhang support brackets were accurately and efficiently represented. Cross-frames were considered critical members for transferring lateral response between girders and were therefore modeled using the same level of detail as for the I-girders. Field measurements and numerical simulation results were post-processed into strong-axis bending stress and lateral bending stress (from weak-axis bending and warping torsion), also considering axial response. Numerical simulation approaches were validated with good comparison between 3D FEA results and measured girder strong-axis bending and lateral bending response for deck placement.

Parametric studies were then conducted to investigate the effects of bridge skew on steel I-girder response under construction, with a focus on evaluating girder flange lateral bending stress. The two instrumented bridges were analyzed with skew variation from 0° to 70° (keeping other parameters from the overall design unchanged), and seven additional real bridges were selected from a database provided by the Illinois Department of Transportation to enhance the analysis findings. Key general findings are summarized below.

- Larger skew leads to a slightly smaller magnitude of strong-axis bending stress, which is clearer near girder midspan locations.

- The skew effect on girder flange lateral bending stress can be characterized as an overhang (local) effect or a global effect, or both. The two types of effect are defined in this report as follows:

- Overhang (local) skew effect—lateral bending response that is transferred from exterior girders to interior girders at cross-frames in a skewed bridge with a staggered intermediate cross-frame layout.

- Global skew effect—lateral bending response that is caused by global rotation of a skewed bridge about the skewed support line.

- Near bridge midspan, flange lateral bending stress is significantly affected by skew locally, caused by the transfer of lateral load from exterior girders to interior girders through staggered cross-frames (especially for girder bottom flanges when the skew is less than 60°).

- Near bridge supports, girder lateral bending is primarily affected by skew globally, caused by rotation of the steel system about the skewed support line.

Skewed I-Girder Bridge Behavior under Truck Live Load

The instrumented bridges were loaded in the field with two series of isolated truck tests—one on the in-service half-Mattis-74 bridge (during staged construction) at crawl speed and the other on the fully constructed Mattis-74 and Mattis-57 bridges at multiple speeds. Satisfactory comparisons between numerical simulation results and field measurements for girder and cross-frame response under the isolated truck testing were achieved, which validates the modeling approaches for in-service bridges under live load. An illustration of I-girder cross-section behavior based on the crawl speed live load tests on half-Mattis-74 was presented to assist with interpretation of the stress decomposition method used throughout this research. Key observations of bridge superstructure response under live load, based on field testing and companion numerical simulation, are summarized below (focusing on girder strong-axis bending and lateral bending). Some evaluation of standard design practice is also mentioned to emphasize the observations.

- For girder strong-axis bending stress:

  - The controlling response was observed at the girder closest to the test path.

  - Maximum strong-axis bending stress calculated using line girder analysis (LGA), with a live load distribution factor (LLDF) defined in AASHTO, conservatively estimated girder strong-axis bending stress under the isolated truck tests by around 50%.

  - Exterior girders are more conservatively designed than interior girders with respect to strong-axis bending stress when directly loaded.

  - Calculating strong-axis bending stress with the same LLDF for all girders ensures safety for exterior girders under even special live load cases (e.g., during staged construction). However, it could be over-conservative for interior girders with isolated truck loading.

- For girder bottom flange lateral bending stress:

  - Critical response was consistently observed at cross-frame locations.

- Governing girder lateral bending response was observed at the girder near a load path, except when the live load was close to exterior girders.

- When truck loading was placed near an exterior girder, maximum lateral bending response was observed at the second adjacent interior girder, and critical stress in the girder was close to the corner far away from the loaded obtuse corner.

- Interior girders were more critical than exterior girders with respect to bottom flange lateral bending along bridge spans, which supports the AASHTO suggestion (in the absence of a refined analysis) of lowering the additional lateral bending stress for exterior girders when designing skewed bridges over 20° with a staggered cross-frame layout throughout the bridge.

- The maximum bottom flange lateral bending stress near bridge supports was almost evenly distributed for all girders, with a magnitude smaller than that along the spans.

Numerical parametric studies were conducted to further evaluate standard design practices of skewed steel I-girder bridges under live load and to improve knowledge of load distribution in these bridges. Effects of bridge skew, type of abutment, bridge width, and position of live load on girder response were considered during the parametric study. Key observations (based on simulation of isolated truck loads) are summarized below. The isolated truck loading scenario was chosen for compatibility with the field tests and clarity in observing load distribution trends. However, this scenario does not represent the complete set of loads for design (i.e., lane loads plus design trucks), so the findings are focused on global behavior and making relative comparisons for a simple loading case. Major findings regarding girder strong-axis bending stress of skewed steel I-girder bridges subjected to truck live load are as follows:

- The magnitude of maximum strong-axis bending stress under any load path slightly decreases with an increase in skew.

  - For stub abutment bridges: the rate of stress decrease with increase in skew was larger for narrower bridges and larger for exterior girders (compared to interior girders).

  - For integral abutment bridges: the rate of stress decrease with increase in skew was consistent for various bridge widths and for exterior girders versus interior girders.

- Critical strong-axis bending stress was observed at the girder closest to the load path.

- When directly loaded in a similar way, exterior girders were observed with larger strong-axis bending stress than interior girders. However, exterior girders are not likely to be directly loaded except when incomplete bridges are temporarily in service during construction or bridge widening.

- Live load placed closer to mid-width of a bridge is better distributed among adjacent girders, whereas live load placed closer to an exterior edge of a bridge is less well distributed and more concentrated at the closest girder.

The distribution of lateral bending response for skewed steel I-girder bridges is dependent on the location of the live load. The following points summarize the distribution of lateral bending response in interior girders (based on numerical parametric studies of isolated truck loads), which is generally more critical than exterior girders:

- Distribution of lateral bending response over the width of a bridge—Live load placed close to (or directly over) an exterior girder induces peak lateral bending response at the second adjacent interior girder inward (for bridges more than four girders wide), and notable lateral bending stress was distributed all the way to the third interior girder (inward) for the scenarios presented in this report. Live load placed near mid-width of a bridge (away from exterior girders) is concentrated on the nearby interior girders, instead of being distributed further outward.

- Distribution of lateral bending response over the length of a bridge—Live load placed near mid-width of a bridge (away from exterior girders) induces peak lateral bending stress near midspan of the critical girder, regardless of skew. Live load placed close to (or directly over) an exterior girder induces peak lateral bending stress further away from midspan of the critical girder as skew increases; peak stress is located on the second interior (inward) girder, close to the obtuse corner that is not directly loaded.

PRACTICAL APPLICATIONS

AASHTO LRFD considers flange lateral bending of I-girders on a skewed bridge during deck placement by separately estimating an overhang effect (C6.10.3.4) and a skew effect (C6.10.1): (1) lateral bending behavior induced by overhang load is evaluated on exterior girders in standard practice, which might be done without considering additional flange lateral bending that may result from skew; (2) in the absence of a more refined analysis, girder flange lateral bending stress due to the skew effect is recommended as 69 MPa (10 ksi) for interior girders and 14 MPa (2 ksi) for exterior girders away from the end supports when a bridge is skewed more than 20° and uses discontinuous cross-frames or diaphragms along the entire bridge. Although AASHTO C6.10.1 is somewhat ambiguous, the proper interpretation seems to be that the recommended flange lateral bending stress estimate in exterior girders near skewed bridge supports is 7.5 ksi when there are discontinuous cross-frames near the supports. The AASHTO lateral bending recommendation is intended to encompass all sources of unfactored load. Key findings from evaluating the abovementioned standard design practice with respect to girder flange lateral bending stress of skewed steel I-girder bridges under concrete dead load, through field monitoring and numerical parametric studies, are summarized as follows:

- Evaluation of AASHTO C6.10.3.4—Near bridge midspan, larger flange lateral bending stresses were observed on interior girders than exterior girders, which is induced by skew transferring the local overhang load inward.

- Lateral bending response observed near supports was generally larger than that near bridge midspan during deck placement.

- Considerable girder bottom flange lateral bending stress was developed during deck placement at the bridge end for the pre-composite stub abutment bridge when the skew is larger than 60°.

- Consistent with AASHTO, it is suggested that a refined method of analysis capable of considering superstructure lateral load transfer should be carried out to estimate flange lateral bending stress during deck placement, particularly when a bridge is skewed more than 60°.

Girder strong-axis bending under (traffic) live load is evaluated by standard LGA through using LLDF, defined in AASHTO Article 4.6.2.2. The skew effect is considered when calculating LLDF, and exterior and interior girders are usually designed with the same demand in standard design practice utilized by state transportation agencies in the U.S. (as reported in Volume I [Zhou et al., 2026]). In addition to bridge static behavior, AASHTO requires a dynamic load allowance (DLA) of 33% when fatigue is not considered (Table 3.6.2.1-1). The key findings from evaluating the abovementioned standard design practice for skewed steel I-girder bridges, through field monitoring and numerical parametric studies with isolated truck live loads, are summarized as follows:

- For girder strong-axis bending stress—evaluation of LGA using AASHTO Article 4.6.2.2:

    - Exterior girders are prone to larger strong-axis bending stress than interior girders when directly loaded.

    - Estimating girder strong-axis bending stress using LGA is overall conservative for the case of isolated truck loads, but the common practice to use the controlling LLDF for all girders can be overly conservative for interior girders. Either using distinct calculations for exterior and interior girders or introducing a reduction for the lever rule when applying exterior girder LLDF to interior girders will help make bridge design requirements more efficient for the case of isolated truck live loading.

    - Standard LGA assumes the same boundary conditions when designing IABs and stub abutment bridges, which makes strong-axis bending stress estimation for IABs even more conservative.

    - The skew effect considered in the calculation of LLDF is conservative for stub abutment bridges, especially for narrow bridges and exterior girders.

- For girder bottom flange lateral bending stress—evaluation of AASHTO C6.10.1:

- Narrow bridges with four girders have less lateral bending response than wider bridges. Girder lateral bending response on bridges more than six girders wide was not affected by bridge width when considering the same level of truck loading (i.e., an isolated truck load).

- Interior girders are in general more critical than exterior girders regarding flange lateral bending stress, which is consistent with the decrease in suggested additional lateral bending stress for exterior girders per AASHTO when a refined analysis is not used.

- When a truck live load is placed near an exterior girder, bottom flange lateral bending stress is affected by the distance from the first intermediate cross-frame to the bridge end. Controlling that distance according to AASHTO C6.7.4.2 is critical to avoid a large concentration of lateral bending response at bridge ends.

- Evaluation of AASHTO Table 3.6.2.1-1—most DLAs calculated from field measurements for the isolated truck test were less than 20%. DLA for Mattis-74 was consistently within the AASHTO required 33%. DLA for Mattis-57 exceeded the AASHTO requirement at (exterior) girders and cross-frames near obtuse corners.

REFERENCES

ABAQUS. (2023). ABAQUS/CAE. www.3ds.com. Dassault Systems.

Almoosi, Y., McConnell, J., & Oukaili, N. (2021). Evaluation of the variation in dynamic load factor throughout a highly skewed steel I-girder bridge. *Engineering, Technology & Applied Science Research*, *11*(3), 7079–7087. https://doi.org/10.48084/etasr.4106

American Association of State Highway and Transportation Officials. (2024). *Load and resistance factor design bridge design specifications, 10th Edition*. AASHTO.

Deng, Y., Phares, B. M., Greimann, L., Shryack, G. L., & Hoffman. J. J. (2015). Behavior of curved and skewed bridges with integral abutments. *Journal of Constructional Steel Research*, *109*, 115–136. https://doi.org/10.1016/j.jcsr.2015.03.003

Deng, L., Yu, Y., Zou, Q., & Cai, C. S. (2014). State-of-the-art review of dynamic impact factors of highway bridges. *Journal of Bridge Engineering*, *20*(5). https://doi.org/10.1061/(ASCE)BE.1943-5592.0000672

Greimann, L., Phares, B. M., Deng, Y., Shryack, G., & Hoffman, J. (2014). *Field monitoring of curved girder bridges with integral abutments*. Bridge Engineering Center, Iowa State University.

Illinois Department of Transportation. (2020). Understanding the Illinois Size and Weight Laws.

Illinois Department of Transportation. (2023). *Bridge manual*. Bureau of Bridges and Structures.

Illinois Department of Transportation. (2024). *Illinois Bridges E-Plan*. Accessed January 15, 2024. http://apps.dot.illinois.gov/eplan/DESENV/

LaFave, J. M., Brambila, G., Kode, U., Liu, G., & Fahnestock, L. A. (2021). Field behavior of integral abutment bridges under thermal loading. *Journal of Bridge Engineering*, *26*(4), 04021013. https://doi.org/10.1061/(ASCE)BE.1943-5592.0001677

Lu, R., & Judd, J. (2022). Effect of bridge skew on the analytical and experimental responses of a steel girder highway bridge. *Lect. Notes Civ. Eng. Vol 213*. Springer, Singapore.

Luo, J., Fahnestock, L. A., & LaFave, J. M. (2021). Seismic performance assessment of quasi-isolated highway bridges with seat-type abutments. *Journal of Earthquake Engineering*, *25*(11), 2285–2324. Taylor & Francis.

McConnell, J. R., Radovic, M., & Ambrose, K. (2016). Field evaluation of cross-frame and girder live-load response in skewed steel I-girder bridges. *Journal of Bridge Engineering*, *21*(3), 04015062. https://doi.org/10.1061/(ASCE)BE.1943-5592.0000846

McConnell, J., Radovic, M., & Keller, P. (2020). Holistic finite element analysis to evaluate influence of cross-frames in skewed steel I-girder bridges. *Engineering Structures*, 213, 110556. https://doi.org/10.1016/j.engstruct.2020.110556

Okumus, P., Oliva, M. G., & Arancibia, M. D. (2018). *Design and performance of highly skewed deck girder bridges* (Report No. 0092-16-05). Wisconsin Department of Transportation Research & Library Unit.

Radovic, M. (2017). “Evaluating the role of cross-frames in stress distribution of steel I-girder bridges by ‘holistic’ assessment of finite element analysis data.” Thesis, University of Delaware. https://udspace.udel.edu/handle/19716/24513

Sanchez, T. A. (2011). “Influence of bracing systems on the behavior of curved and skewed steel I-girder bridges during construction.” Ph.D., Georgia Institute of Technology. https://smartech.gatech.edu/handle/1853/42731

Stallings, J. M., Cousins, T. E., & Stafford, T. E. (1996). Effects of removing diaphragms from steel girder bridge. *Transportation Research Record*, *1541*(1), 183–188. https://doi.org/10.1177/0361198196154100124

Stallings, J. M., Cousins, T. E., & Stafford, T. E. (1999). Removal of diaphragms from three-span steel girder bridge. *Journal of Bridge Engineering*, *4*(1), 63–70. https://doi.org/10.1061/(ASCE)1084-0702(1999)4:1(63)

Tedesco, J. W., Stallings, J. M., & Tow, D. R. (1995). Finite element method analysis of bridge girder-diaphragm interaction. *Computers & Structures*, *56*(2), 461–473. https://doi.org/10.1016/0045-7949(95)00037-H

Théoret, P., Massicotte, B., & Conciatori, D. (2012). Analysis and design of straight and skewed slab bridges. *Journal of Bridge Engineering*, *17*(2), 289–301. https://doi.org/10.1061/(ASCE)BE.1943-5592.0000249

Vermont Agency of Transportation. (2008). *Integral abutment bridge design*. VTrans Integral Abutment Committee.

Zhou, S., Dorado, R., LaFave, J. M., & Fahnestock, L. A. (2026). *Spatial and temporal load distribution in steel bridge superstructures (Vol. I): Agency survey and preliminary numerical modeling of skewed steel I-girder bridges for field instrumentation* (Report No. FHWA-ICT-26-002). Illinois Center for Transportation/Illinois Department of Transportation. https://doi.org/10.36501/0197-9191/26-002

Zhou, S., Fahnestock, L. A., LaFave, J. M., & Dorado, R. (2024). Construction and live load behavior of a skewed steel I-girder bridge. *Transportation Research Record*, *2678*(1), 846–860. https://doi.org/10.1177/03611981221105276


Illinois Department
of Transportation


ILLINOIS